Synthesis and Characterization of $Fe_{70}Pd_{30}$ Nanohelices

Cheng Xu

A dissertation
submitted in partial fulfillment of the
requirements for the degree of

Doctor of Philosophy

University of Washington

2018

Reading Committee:

Minoru Taya, Chair

Dwayne D. Arola

Christine Luscombe

Program Authorized to Offer Degree:
Materials Science and Engineering

University of Washington

Abstract

Synthesis and Characterization of $Fe_{70}Pd_{30}$ Nanohelices

Cheng Xu

Chair of the Supervisory Committee:
Professor Minoru Taya
Mechanical Engineering Department

A device performing controlled actuation and motion at the nanoscale will be the essential component for future nanoelectromechanical systems. $Fe_{70}Pd_{30}$ ferromagnetic shape memory (FSMA) alloy shows multi-functional effects, including conventional shape memory effect, superelasticity, ferromagnetic shape memory effect, magnetostriction, and Invar effect. These unique properties make $Fe_{70}Pd_{30}$ alloy a promising nanoactuation material. This work aims to fabricate $Fe_{70}Pd_{30}$ nanosprings which serve as the key building block of linear spring actuator in nanoscale. I develop a synthesis route of potentiostatic-galvanostatic mix pulse electrodeposition using a porous anodic alumina (PAA)-mesoporous silica hybrid template for fabrication of $Fe_{70}Pd_{30}$ nanosprings with precise chemical composition. This synthesis route can be applied as a general method for nanospring synthesis and not limited to specific target materials. Then I explore the crystal structure and temperature induced martensite phase transformation of annealed $Fe_{70}Pd_{30}$ nanosprings which are essential for their potential use as shape memory smart materials. Finally, I investigate the various microphases of Fe-Pd nanowires that originate from the block copolymer-silica co-self-assembly under cylindrical confinement via experiment and simulation.

TABLE OF CONTENTS

LIST OF FIGURES

LIST OF TABLES

ACKNOWLEDGMENTS

I would like to express my gratitude for the guidance, support, and encouragement from my doctoral advisor, Prof. Minoru Taya, and the members of my committee, Prof. Dwayne Arola, Prof. Christine Luscombe and Prof. Tomikazu Sasaki.

I thank all the visiting scholar and labmates who helped in various respects in my research. Especially I appreciate Prof. Shinji Muraishi for his help of TEM analysis, Prof. Takehiro Matsuse for his help on molecular dynamic simulation of Fe-Pd nanospring, Prof. Takahiro Kunimine for his advice based on Fe-Pd nanoparticle system and his help on TEM sample preparation, Dr. Hiromi Yasuda for introducing me to Python, Dr. Satoshi Yamatomo for his help on polymerization, Dr. Satomi Takao, Nishita Ananda and Bryan Ferguson for inspiring discussions.

I am also very grateful for the help from all the research scientists in Molecular Analysis Facility (UW) and Washington Nanofabrication Facility (UW). Special thanks go to Liam Bradshaw for his help on XRD analysis, Ellen Lavoie for her help on TEM analysis, Scott Braswell for his help on SEM analysis and Darick Baker for his help on the sputtering.

I thank my friend Dr. Xiuwen Zheng for his patience in answering my questions related to programming (C++ and R) .

I thank my parents Lishen Xu, Hui Liu and my sister Ping Xu for their unconditional love.

DEDICATION

I dedicate this thesis to my family, my father Lishen Xu, my mother Hui Liu, and my sister Ping Xu

Chapter 1

INTRODUCTION

Nanoscale mechanical devices have been emerging rapidly in the field of science and engineering due to their wide range of applications such as signal processing, optical/acoustic metamaterials, and robotic surgery [1, 2, 3, 4, 5, 6]. The recent state-of-the-art fabrication techniques, together with electromagnetic system, has enabled one to develop nanoelectromechanical systems (NEMS) [7, 8, 9, 10]. The current NEMS devices employed electrostatic (capacitive) actuation, magnetomotive actuation, thermal actuation, piezoelectric actuation and magnetostriction actuation mechanisms to actuate the structure [11, 12, 13, 14, 15]. However, to develop efficient and robust NEMS devices with accurate manipulation, we need to improve actuation system. Recently, the spring actuator based shape memory alloys (SMAs), which can show efficient actuation arising from martensite phase transformation, has been proposed [16].

Fe-Pd binary alloy at the chemical composition near 70 at.% exhibits functional effects, including conventional thermal shape memory effect (SME), ferromagnetic shape memory effect (FSME), superelasticity (SE), magnetostriction and Invar effect. Such advantageous effect along with their high ductility (compared to NiMnGa ferromagnetic shape memory alloy) [17] and biocompatibility [18] make $Fe_{70}Pd_{30}$ a promising sensing and actuating material for biomedical applications. A helical shape memory actuator can attain 200% to 600 % deformation according to its geometry [19]. Therefore such spring actuator with large stroke and significant forces attracts enormous scientific interest.

The main work in this thesis is inspired by the macroscopic $Fe_{70}Pd_{30}$ shape memory robot [16] in which the $Fe_{70}Pd_{30}$ spring is the critical component. The current work aims to generate equivalent actuator in nanoscale to meet the need for applications in growing

nanotechnology, especially for potential robotic cancer therapy. Here, I study the fabrication technique for Fe-Pd nanohelices with precise control of chemical composition. Electrodeposition utilizing a porous anodic alumina (PAA)-mesoporous silica hybrid template is proved to be an efficient way to generate $Fe_{70}Pd_{30}$ nanohelices. The spring structure is formed as a result of block copolymer-inorganic silica precursor co-self-assembly under cylindrical nano-confinement. The combination of the intrinsic property of the block copolymer, the block copolymer-confining wall interaction and the degree of confinement lead to a series of novel microphases, including the target nanosprings, opposed to the bulk case. Since Fe-Pd system is highly sensitive to the chemical composition, all its beneficial effects depend on the development of a synthesis route for nanoscale spring with precise control of the stoichiometry. Then the next step is to explore whether $Fe_{70}Pd_{30}$ in nanoscale retain the reversible martensite phase transformation as its bulk phase. I investigate the crystal structure of as-deposited and annealed $Fe_{70}Pd_{30}$ nanowires, and explore their temperature induced martensite phase transformation. I also explore the various morphology of Fe-Pd nanowires originate from block copolymer-silica co-self-assembly under nanoconfinement.

This dissertation is structured as follows: Chapter 2 briefly reviews the background knowledge. Chapter 3 describes the experimental details to fabricate templates to generate continuous Fe-Pd nanosprings. Chapter 4 discusses the effect of the plating bath composition and plating technique on the chemical composition of the Fe-Pd thin film and Fe-Pd helices. This study ensures that the fabricated Fe-Pd nanowires reach to 70 at.% Fe and meet the pre-requirement of shape memory effect. Chapter 5 focuses on the crystal structure of Fe-Pd nanorods and Fe-Pd nanohelices and discusses the thermoelastic martensite phase transformation. Chapter 6 discusses the morphology evolution of electrodeposited Fe-Pd nanowires and the methods to enlarge the size of Fe-Pd helices by enlarging the equilibrium period of the structure guiding block copolymer.

Chapter 2

BACKGROUND

Within the following chapter, I first briefly review the fundamentals of shape memory alloys, including the conventional shape memory effect, superelasticity, and ferromagnetic shape memory effect. And I introduce a $Fe_{70}Pd_{30}$ spring based linear actuator as the potential nanorobot for biomedical application. Then the composition sensitivity of $Fe_{70}Pd_{30}$ binary alloy is presented to emphasize the significance of stoichiometry control of Fe-Pd system. The next session discusses the conventional fabrication techniques of metallic nanohelices, followed by an emphasis on nanoconfined mesoporous silica template method. The last part discusses the fundamentals of electrochemical deposition, the conventional plating baths, the resulting shape and the crystal structure of the Fe-Pd binary alloy system by electrodeposition.

2.1 Shape Memory Alloy

Shape memory alloy (SMA) is a class of materials which shows large reversible strain when subjected to thermal, stress or magnetic loading. SMAs showing shape memory effect (SME) and superelasticity (SE)/pseudoelaticity (PE) are of great current interest because of their unique properties, allowing the direct use of material itself as sensing or actuating device. The shape memory behavior is first discovered by Chang and Read in Au-47.5 at.%Cd alloy [20] in 1951. Then in 1963, $NiTi$ is found to have the same property by Buelher [21]. Until now, there are two main families of conventional SMAs: copper-based $CuAl - X$ SMAs [22, 23], and $NiTi-Y$ SMAs (X, Y stand for a third element) [24, 25]. Their shape memory actuation is driven by temperature change. Besides the well-known conventional SMAs, ferromagnetic shape memory alloys (FSMAs) shows the actuation to the magnetic field beside the thermal

fields. For conventional SMAs, the speed of actuation is usually limited by the speed of heat conduction. While the FSMAs can reach much higher actuation speed since the magnetic field can be switched in the range of KHz. Among FSMAs, *Ni-Mn-Ga* system is most widely studied and used. Other FSMAs, for example,*Fe-Pd*, *Fe-Pt*, *Co-Ni-Al* and so on also attracted lots of interest [26, 27, 28, 29].

The key element that lies behind the shape memory effect and superelasticity of SMA is the reversible martensite phase transformation. The martensite phase transformation is a displacive, first-order diffusionless transformation from a high symmetric high temperature austenite phase (Fig.2.1(a)) to a low symmetric low temperature martensite phase (Fig.2.1(b)). Martensite phase has been discovered in many alloys, for example, the martensite phase in steel. However, only the reversible thermoelastic martensite phase transformation shows the shape memory effect. During the martensite phase formation, twining (Fig.2.1(b)) is favored over gliding to reduce shearing stresses because the former retains all the atomic bonds and the degree of order.

The shape memory effect induced by temperature change can be explained by the cycle from (a) to (c) in Fig.2.1. When a SMA is cooled down passing the martensite starting temperature, a twinned martensite phase is formed. From (a) to (b), atom positions will slightly shift to generate a new phase and there is no volume change for this phase change. The structure in (b) is called 'twin structure'. The structures separated by the twin boundary (red line in (b)) are mirror image of each other. At the thermal induced martensite stage, stress can be applied to create deformation of SMA. This deformed shape is maintained until SMA is heated again. Heating causes deformed shape (c) to return to austenite phase. Macroscopically view shows that the alloy can 'remember' its original shape before deformation. This effect of SMA is known as the 'one-way shape memory effect'. It is noticeable that this one way shape memory effect is just one time effect. Meaning that after deformed martensite returns to austenite, cooling will not lead to shape change unless stress is applied. Except for one-way shape memory effect, SMA can be programmed to remember the deformed shape during a special 'training' treatment, to get the two-way shape memory

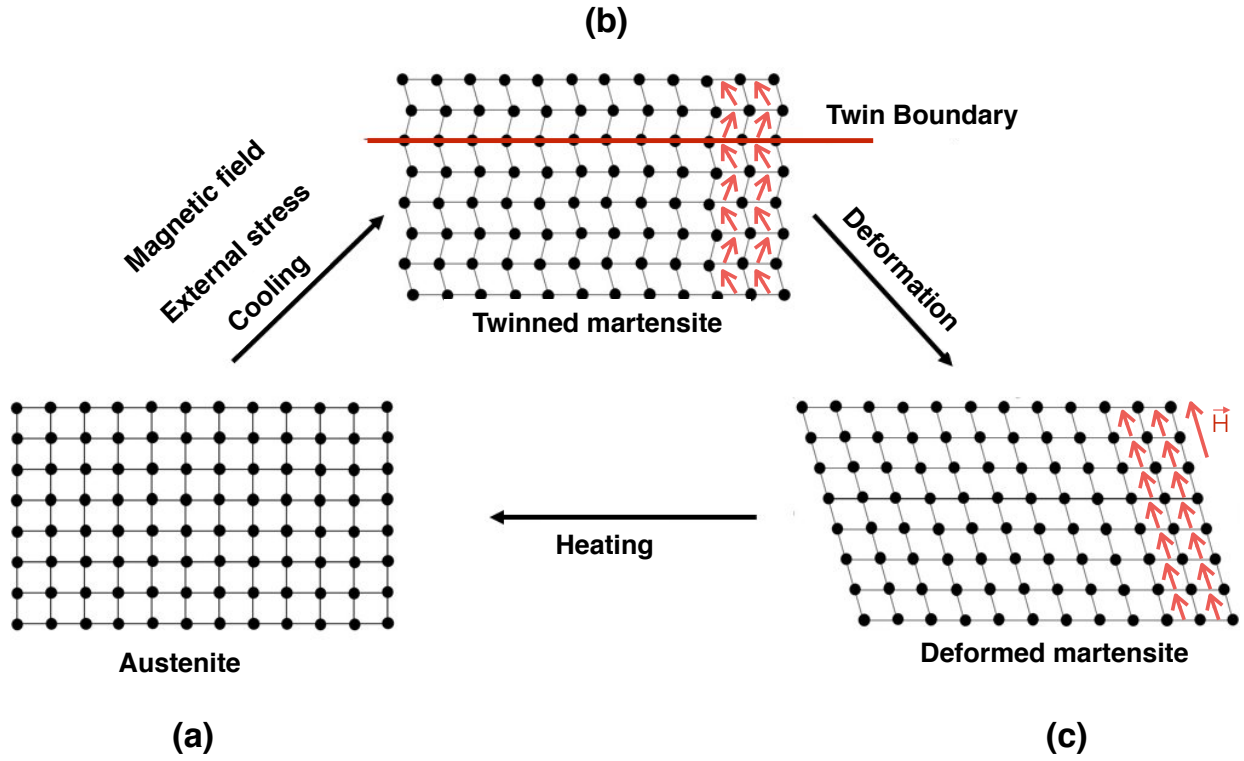

Figure 2.1: Illustration of reversible martensite phase transformation of SMA (a) the parent austenite phase (b) the twinned martensite phase (c) the deformed martensite phase. the red arrow in the crystal cells shows the direction of the magnetic moment.

effect. During the training process, stress is applied to trigger the rearrangement of martensite to form 'stress-induced martensite'. SMA learns to remember the deformed stage of its shape and can go over multiple times of the deform-recover cycle.

Besides the thermal induced phase transformation, stress can also initiate martensite transformation. At a temperature right above martensite transformation starts, the applied stress stabilizes martensite while unloading leads to the disappearance of the formed martensite. The stress needed to initiate martensite transformation increases with increasing temperature [30]. Thus there is a critical temperature Md that beyond this temperature, the stress will cause dislocation movement before it can inititate the martensite transformation.

Af is the temperature that austenite transformation completes. Between Af and Md, the strain can be fully recovered; this effect of SMA is named as superelasticity.

Large reversible strain can also be induced by the magnetic field for FSMAs. The shape change of FSMAs under magnetic stimuli is usually caused by three mechanisms: (1) magnetic field induced martensite phase transformation; (2) magnetic field induced martensite variants reorientation; and (3) magnetostriction. When the difference of saturation magnetization between austenite and martensite is large, the sample near phase transformation state might go through reversible martensite transformation under an applied magnetic field. However, the required magnetic field is huge to induce martensite phase. In Fe-Ni alloy system, a 10 T magnetic field cause a 20 °C shift in phase transformation temperature. In the less symmetric martensite phase with large magnetocrystalline anisotropy, the magnetic moment is usually aligned in a particular crystallographic easy magnetization direction. The red arrows in Fig.2.1(b) shows the alignment of magnetic moment direction in each twinned martensite unit cell under zero magnetic field. Under an external magnetic field, the domain wall of the twinned unit cells will move and the magnetic moment will align themselves in the direction of the external field. The overall effect of such martensite variants reorientation is the large strain of the materials. The magnetostriction describes the volume change of materials originates from electron spin orbit coupling under an external magnetic field. The resulted strain from magnetostriction is much smaller compared with the strain generated from the martensite phase transformation and martensite variants reorientation.

The phase change of the SMAs leads to its diverse applications. For example, in the medical field, NiTi alloy can be used as the stent to treat the narrowing of the blood vessel. The recovery strain of correctly machined NiTi shape memory alloy can reach up to 8%. In comparison, 304V stainless steel can only reach to 0.5% [31]. The NiTi stent in a closed state will fit into a small volume to be delivered into the blood vessel easily.After transport to the target location, NiTi stent in an open state will expand and support the wall of the blood vessel. Thus the blood will flow freely. Another successful application of SMA is for tube coupling. In 1971, Raychem developed the coupling system for titanium tubing in

hydraulic lines [32]. The coupling part is first machined in the austenite state with an inner diameter smaller than the outer diameter of the tube. Then the part is cooled down to the martensite state and mechanically expanded the inner diameter to be larger than the outer diameter of the tube. After connecting the part and the tube, the martensite will transform to austenite by increasing the temperature. The inner diameter of the part will shrink to the original scale thus realize the coupling. The other major application of SMAs is to be used as actuators, due to their simplicity of mechanism, clean, silent, spark-free and zero-gravity working conditions and high power/weight ratios [33]. The easiest and most classic SMA actuator is the SMA coil spring. By using SMA helical spring as a basic component, Wada and Taya designed and made a linear actuator with *Fe-Pd* ferromagnetic SMA [16]. *Fe-Pd* FSMA exhibits three different actuation modes, (i) phase change under the constant applied magnetic field, (ii) variant rearrangement in 100% martensite under constant applied magnetic field, resulting in large strain, and (iii) phase change under applied magnetic field gradient [34]. Taya group used the third actuation mechanism to design a set of actuators. An example of such actuators based on the third actuation mechanism is novel linear actuator composed of mainly two parts (see Fig.2.2). The first part is composed of permanent magnet, electromagnet, and yoke. This part provides the magnetic field gradient. The second part is a coil spring made of $Fe_{70}Pd_{30}$. Because of the martensite phase transformation, the stiffness of the spring is much less than that of the spring made of Fe. And the martensite phase transformation accommodates the stress concentration on the surface of the spring. These allow the spring to achieve full contraction, as compared with conventional Fe based spring that can only reach much smaller stroke than *Fe-Pd* based spring. Taya *et al.* [35] conducted molecular dynamic simulation on the actuation of nanorobots made of cylindrical head and helical tail. For a nanorobot with head diameter 60 nm, head length 200 nm and helical spring wire diameter 10 nm, outer loop diameter 60 nm and loop gap 3 nm, the complete contraction of spring was observed under an applied field of 0.448 T, giving a total stroke of 47 nm. This result suggests that *Fe-Pd* shape memory nanorobots under oscillating magnetic field can be used as nanolinear actuator.

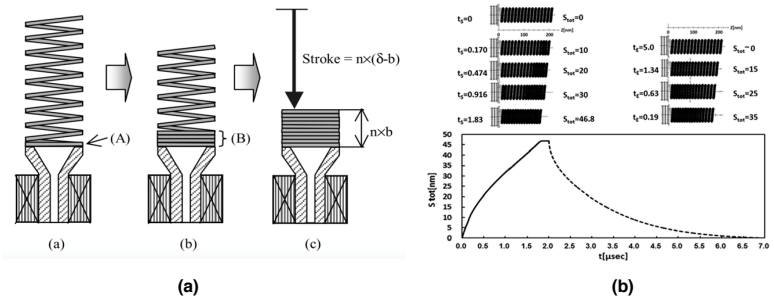

Figure 2.2: (a) MacroscopicFe-Pd spring based linear actuator (obtained from reference [16]) (b) The actuation of Fe-Pd nanorobots made of Fe-Pd cylindrical 'head' and Fe-Pd helical 'tail' under magnetic switch on and off mode (obtained from reference [35]).

2.2 Fe-Pd **Shape Memory Alloy**

There are two types of FSMAs that exhibit large (> 0.005) field-induced strain: Ni_2MnGa and $Fe_{70}Pd_{30}$ [36]. The field-induced strain of Ni_2MnGa (5.8% in tetragonal and 9.4% in orthorhombic [37]) is larger than that of $Fe_{70}Pd_{30}$ (0.6% [38]). However, Ni_2MGa is a brittle material, and Ni might cause health issues including skin allergies, lung fibrosis, variable degrees of kidney and cardiovascular system poisoning and stimulation of neoplastic transformation [39].On the other hand, Fe-Pd alloy in the proximate composition of $Fe_{70}Pd_{30}$ has several advantages including its high magnetocrystalline anisotropy, high ductility compared with Ni_2MnGa, fast response speed towards magnetic fields when compared with conventional SMAs and less known hazards to human health concerns [18, 40, 41],making it a promising material as an FSMA actuator.

Fig.2.3(a) shows the equilibrium phase diagram based on bulk Fe-Pd which indicates that the single (γ-Fe, Pd) face centered cubic (fcc) phase with disordered Fe and Pd atoms in lattice only stably exists at temperatures higher than 1043 K. Slow cooling to room temperature will lead to the decomposition of the single ($\gamma - Fe, Pd$) fcc phase into $Fe_{50}Pd_{50}$ and α-Fe,Pd solid solution phases. Thus rapid quenching is necessary to limit the diffusion speed of iron to avoid the phase decomposition and permit the existence of metastable

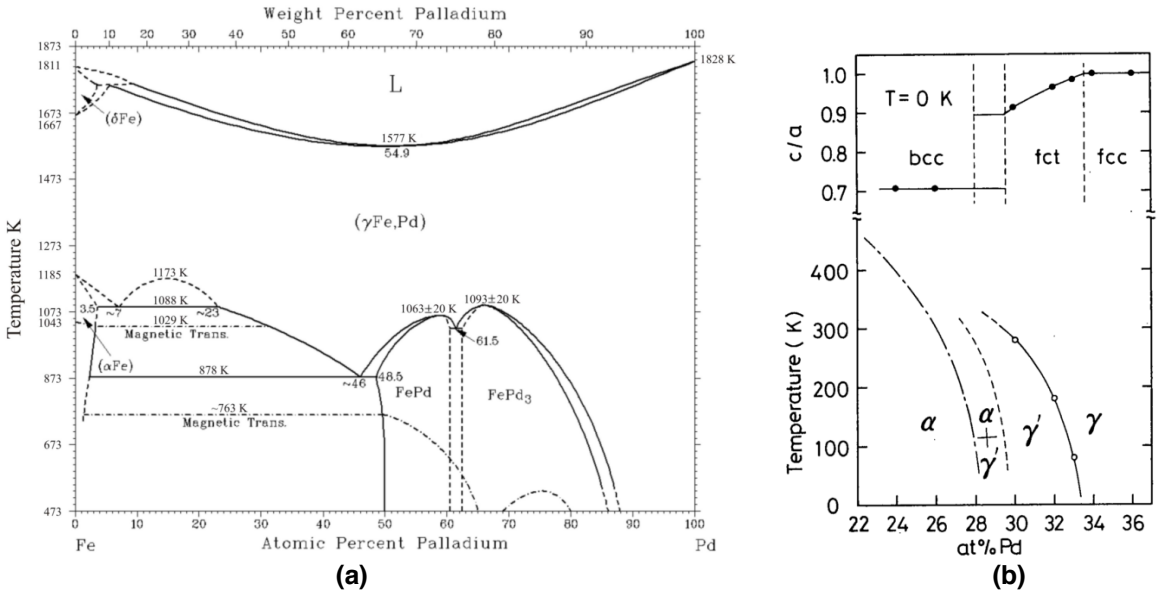

Figure 2.3: (a) *Fe-Pd* alloy equilibrium phase diagram [42] dependent on the chemical composition and temperature at constant ambient pressure (b) *Fe-Pd* metastable phase diagram at 22 at.% Pd to 37 at.% Pd [43].

$Fe_{70}Pd_{30}$ fcc phase at room temperature. Matsui *et al.* [43] reported the metastable phase diagram of the *Fe-Pd* system for bulk *Fe-Pd* melted in a plasma-jet furnace and annealed at 1150 °C for seven days in a vacuum silica tube. Their results showed that the face-centered tetragonal (fct) phase (γ' in Fig.2.3(b)) only exists in the stoichiometry range of 28 at.% Pd to 33.5 at.% Pd. The martensite starting temperature is highly sensitive to the composition. On an average increase of 0.1 % Pd, the martensite starting temperature drops around 10 K. At 30 at.% Pd, the reversible phase transformation starts at around 300 K. If the composition deviates to a lower Pd at.% region but is still greater than 28 at.% Pd, the alloy will easily enter the body-centered tetragonal (bct) phase ($\alpha+\gamma'$) region which is not reversible. While if the composition changes slightly to the higher Pd at.% region but still is lower than 33.5 at.% Pd the reversible transformation temperature will decrease drastically, which will limit the applications of FSMA. Since the nano-spring coil based actuator demands reversible fcc-fct phase transformation at room temperature, the *Fe-Pd* nanospring is highly compositionally

sensitive. Therefore, one of the main issues for Fe-Pd FSMA nanosprings fabrication is to precisely control the homogeneous chemical stoichiometry close to $Fe_{70}Pd_{30}$ with single fcc austenite phase.

2.3 Synthesis Methods for Nanohelices

In this section, I examine nano-scale fabrication process for designing the Fe-Pd based actuator, specifically helical structures. Altough Fe-Pd based spring in centimeter scale [16] has exhibited its effective actuation mechanisms, nanoscale FSMA-based springs have never been fabricated. One of the challenges is that the processing methods of nanohelices highly depend on the specific target material. There does not exist one general method for all kinds of nanohelices. Molecular self-assembly is usually used for synthesizing organic and polymeric nanohelices [44, 45]. While for inorganic nanohelices synthesis, the strategy can be concluded in two categories: template-free method and template-based method.

2.3.1 Template-free Method

In the template-free method, nanohelices can be synthesized by glancing angle deposition (GLAD), residual stress release of strips, self-coiling helices driven by spontaneous dipole moment, and electrospinning.

Glancing angle deposition is one of the most promising template-free method for synthesis of nano helix with limited turns. Compared with conventional vapor deposition, the incident physical vapor for GLAD has a large glancing angle ($\theta > 70°$) with the substrate. When the substrate is not specially treated, the vapor flux nucleates randomly. Because of the large incident angle, the nucleated grain will block the incident flux. The space behind the nucleated grain will not receive the incident flux. Such shadowing effect will cause the columnar growth of vapor source. When a step motor is applied to rotate the substrate with the axis normal to the surface, different shapes like zigzag, spiral nanowires can be obtained. In such untreated substrate, the nucleation sites are close to each other, thus the processed wires are densely packed. Need to notice that it is possible to pre-pattern the substrate to

create preferred nucleation site. In this way, the distance between each helix wire can be adjusted. Various materials, including Cr, Mg, Cu, MgF_2, SiO_2, CaF_2 [46, 47], Si, TiO_2, SnO_2 [48], Au, Ag, Ag-Cu alloy [49] have been successfully made using GLAD. With the GLAD method, a broad range of materials can be deposited and the co-deposition with controllable composition of alloys is possible. However, the drawbacks of the GLAD method are that the shape of the GLAD synthesized helices are not well formed, the shape of GLAD processed springs are close to screw shape with limited turns and not flexible. Therefore, the fully contraction and relaxation cycles of spring can not be satisfied.

Another template-free method to produce nano-helix is to roll up a pre-strained bilayer membrane. Bell *et al.* [50] fabricated $InGaAs/GaAs$ helices by utilizing the curl up method. The process consisted of epitaxial deposition in the sequence of AlAs, InGaAs and GaAs onto GaAs substrate. Then E-beam/photolithography was used to create the strip pattern. Such pattern could be further transferred to InGaAs/GaAs by dry etching. Then the sacrifice AlAs layer was etched away by HF aqueous solution. Because of lattice mismatch between InGaAs and $GaAs$, there is compression in GaAs and tensile stress in InGaAs layer before the removal of $AlAs$. After the removal of sacrificial AlAs layer, the interface force would cause the bilayer to curve up. The direction of rolling of bilayer is determined by the stiffness anisotropy [50]. So far InGaAs/GaAs [50], SiGe/Si [51, 52] Si/Gr [53] nano-helix have been synthesized with rolling up method. Using this method, a precise control of the geometry of the helix spring (including helix pitch and angle) can be realized. However, the material might be limited to satisfy the lattice mismatch condition of the bilayer.

Other template-free methods are also developed for processing of nano-helix. The polar surface induced self-coiling during vapor solid growth is well developed in researches of ZnO nanohelice [54, 55]. For the materials that are non-centrosymmetric, there will be a spontaneous dipole moment generated at the terminated surface. Thus during the vapor solid growth, the wire tend to coil up to decrease such electrostatic energy caused by polar surface. And Chang *et al.* [56] have reported electro-spinning method to obtain iron oxide nano-helix. The size of the nano-helices processed by the electrospinning method tends to

be close to micron scale.

2.3.2 Template-based Method

Besides the direct synthesis of nanohelices, an alternative processing strategy is to create a template with helical holes. Then the target material can infiltrate into the helix template and inherit the parent structure. Metallic nanohelices have been synthesized by electrodeposition using porous anodized alumina (PAA)-porous silica hybrid template, electrodeposition using direct laser writing (DLW), codeposition of Cu and Pt into PAA cylindrical pore, and by DNA template assembling.

Wu *et al.* [57] prepared a hybrid template which is composed of porous anodized alumina (PAA) and sol-gel synthesized porous silica to synthesize pure Ag nano-helical wire. The porous silica was prepared at the same condition of synthesizing SBA-15 mesoporous SiO_2. And such Sol precursor solution was infiltrated into the cylindrical pores of PAA by dip coating. After the mesoporous SiO_2 was fully developed, Ag was filled into the nano pores by alternating current (AC) electro-chemical deposition. By fixing the processing condition of porous SiO_2 and changing the diameter of PAA nanochannel, nanowires shapes vary from donut, single helix, double helix. To date, only single Ag or Ni metal wire have been prepared by this template. If choosing the electro-deposition wisely in this template method, a much broader range of materials can be synthesized. The composition of alloys can be controlled and adjusted by varying the electrodeposition and template condition.

Beyond this template method, Gansel *et al.* [58] have applied direct laser writing (DLW) to synthesize Au helix arrays. The process route includes spinning a positive photoresist onto conductive indium tin oxide layer. Then nano-helix holes inside the positive photoresist were created by DLW. Finally, the holes were backfilled by electrodeposition of Au. Moreover, Liu *et. al.* [59] used hydroxyl terminated PAA template to codeposite Cu and Pd. By tuning the pH and the concentration of the electroplating precursors, the Pd domain may wind up the Cu rod. Thus by selective etching of Cu rod, free-standing Pd helix wires can be obtained. Additionally, Chen *et al.* [60] used DNA as the soft template to guide Au

nanoparticles to form double helix shape. Compared with the $PAA - SiO_2$ template, DLW requires the special equipment which is not readily available and usually generates micron scale helices. Pd-Cu codeposition is not readily applied to wide range of metals and the DNA soft template easily collapse at elevated temperature.

2.4 Mesoporous Silica under Confinement

Mesoporous silica is formed as a result of the interaction between silicate and surfactant (classic product MCM-41 with cationic surfactant [61] , AMS-n with anionic surfactant [62] and SBA-15 with nonionic poloxamer block copolymer) self-assembly. In the case of SBA-15, the hydrated silicate oligomers from tetra-ethoxysilane (TEOS) interact with the EO block of triblock copolymer P123 ($EO_{20}PO_{70}EO_{20}$) [63] and polymerize within the EO block of the self-assembled P123. The nanohelices are formed as a result of P123-Silica ordered microphase frustration under cylindrical confinement by analogy to block copolymer melt microphase frustration under cylindrical confinement, which has been studied both experimentally and theoretically [64, 65]. Self consistent field theory is a great tool to understand and predict the morphology change induced by geometrical confinement [66, 60, 67, 68, 69, 70, 71, 72]. A cylinder forming asymmetric AB block copolymer melt ($f_a = 0.3, \chi N = 20$ where f_a stands for the volume fraction of A block, χ is the Flory-Huggins parameter and N is the degree of polymerization) in the bulk (shown in Fig. 2.4(a)) will curve up to release the frustration caused by the cylindrical confining ($D/L_0 = 1.65$ in this case, where D stands for the diameter of the confining pore and L_0 stands for the equilibrium period of block copolymer melt in the bulk), forming a spring of minority block in majority matrix.

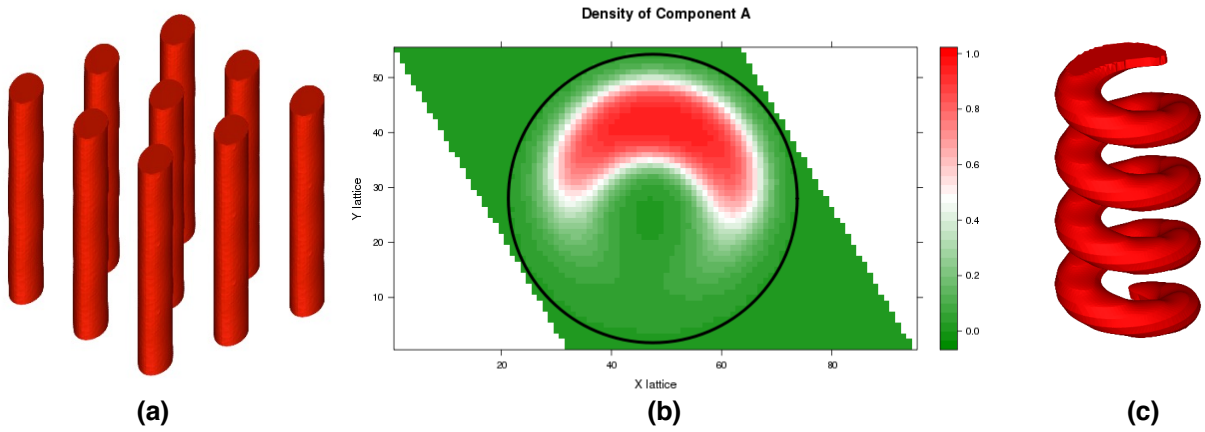

Figure 2.4: (a) Hexagonal packed cylinders in bulk AB block copolymer melt simulated by the Polyorder software [73] (b) Cross section cut of a spring shape asymmetric AB block copolymer under cylindrical confinement. The green parallelogram describes the calculation space in the x-y plane. The black circle shows the confining pore and the scale bar shows the concentration of A block from 0 (green) to 1(red). (c) A single helix simulated by self consistent filed theory ($f_a = 0.3, \chi N = 20, D/L_0 = 1.65$)

2.5 Electrodeposition of Fe-Pd Binary Alloy System

One of the most important considerations involved in the co-deposition of an alloy is that the corresponding ions must be present in a plating bath in which their individual deposition potentials are reasonably close or even the same. Static equilibrium potential is indicative of the energy difference that accompanies the redox reaction and is a good starting point to predict whether the alloy co-deposition will happen or not. Fe^{2+}/Fe and Pd^{2+}/Pd pairs have standard electrode potentials of -0.44 V vs. standard hydrogen electrode (SHE) and 0.99 V vs. SHE respectively [74]. The big difference of their standard electrode potential leads to the reduction of Pd by $Fe(Pd^{2+} + Fe^0 -- > Pd^0 + Fe^{2+}$ and $Pd^{2+} + Fe^{2+} -- > Pd^0 + Fe^{3+})$. Therefore, direct deposition from ferrous and palladium simple salt solution is not possible for reproducible Fe-Pd alloy deposition. There are several methods to bring the static reversible potential of different metals closer: the plating bath can be designed to be more dilute for the more noble metal (which is more resistant to oxidation), or a complexing agent or other

addition agents can be added. According to the Nernst equation,

$$E_{rev} = E^{\theta} - \frac{RT}{zF} ln \left(\frac{a_r}{a_o} \right) \tag{2.5.1}$$

where E_{rev} is the reversible potential of M/M^{z+} pair at the temperature of interest, E^{θ} is the standard electrode potential, R is the gas constant (8.34 $JK^{-1}mol^{-1}$), T is the absolute temperature, z is the number of moles of electrons transferred, F is the Faradays constant ($9.65e^4 Cmol^{-1}$), and a_r and a_o ($a = Cf$, where C is the molar concentration of the ion and f is the activity coefficient) are the chemical activity of the reduced species and oxide species respectively.

There will only be a 0.1183/z V change in the reversible potential for every hundred-fold change of metal salt concentration. Furthermore, if the concentration of the more noble metal is less than 1% of the less noble metal, rapid composition change during electrodeposition will lead to poor reproducibility [75]. Therefore, high-quality *Fe-Pd* alloys cannot be deposited by merely decreasing the concentration of Pd^{2+}. Adding other kinds of additives has been well studied for their ability to modify the crystal structure and as an agent to enhance the brightness in other research [76].While the use of addition agents to bring the dynamic potentials of metals closer together has not been thoroughly studied. Therefore adding a complexing agent may be a general method to modulate the electrode potential of different metals. The reversible potential with complexing agent for M/M^{z+} pair is given by:

$$E_{rev} = E^{\theta} - \frac{RT}{zF} ln \left(\frac{a_r}{a_o} \right) - \frac{RT}{zF} lnK \tag{2.5.2}$$

where K is the stability constant for formed complex. Thus using the proper complexing agent for iron and palladium in order to bring their reversible potential closer is essential for the plating bath design and to achieve co-deposition.

The research of *Fe-Pd* electrodeposition started in 1994 when Juzikis *et al.* [77] first reported the deposition of *Fe-Pd* binary alloy thin film from an ammoniacal bath. They designed a plating bath containing $PdCl_2$ and $Fe_2(SO_4)_3$ with sulfosalicylic acid (5-ssa) as a complexing agent for Fe at a pH ranging from 7 to 8 using a pulse plating method. The

final stoichiometry of their thin film could be modified between 30 wt.% Pd and 85 wt.% Pd by changing the applied current density and electrolyte parent metal composition. They found that under the pulse deposition condition the chemical composition of as-deposited *Fe-Pd* film did not vary much with the pH value ranging from 5.5 to 8.0. Their research also showed that the alloy chemical composition had little fluctuation for pulse durations from 0.001 s to 1 s. In 1998, Baumgaertner [78] developed another plating bath which used $FeCl_3$ and $[Pd(NH_3)_4]Cl_2$ as metal sources and ammonium citrate as the complexing agent with ammonium sulfate as a supporting electrolyte to enhance the conductivity. Baumgaertner reported this plating bath to be stable at pH range of 7.5 to 10.5 and that it is able to produce *Fe-Pd* alloy compositions ranging from 15 at.% Fe to 85 at.% Fe. These two aqueous based electrolytes are the most widely used so far. Most of the existing work on *Fe-Pd* alloy electrodeposition utilizes the plating baths developed by Juzikis or Baumgaertner with modified concentrations of bath components. Watanabe *et al.* [79] developed a new *Fe-Pd* plating bath by complexing Fe^{2+} with ammonium tartrate. They reported a wide range of Fe at.%, from 22.9 at.% to 92.2 at.%, with this novel electrolyte.

All of these electrolytes can serve as a stable plating bath to synthesize *Fe-Pd* alloys with a wide composition range. For all kinds of electrolytes (sulfosalicylic acid based, citrate acid based and tartaric acid based electrolytes) the fraction of less noble Fe will increase with increasing cathodic current density, which is typical anomalous co-deposition (ACD, a term to describe an electrochemical deposition process in which the less noble metal is preferably deposited under most plating conditions) behavior. Fe at.% will increase with decreasing Pd^{2+} concentration in the parent bath [77, 80, 79]. Therefore, in order to obtain a specific *Fe-Pd* stoichiometry, the cathodic current density/cathodic overpotential and Pd^{2+} concentration in parent plating bath should be optimized.

The shape of the deposited *Fe-Pd* alloy can be varied by using different working electrodes. For example, using a flat conductive electrode, *Fe-Pd* thin film with a wide range of composition was fabricated using sulfosalicylic acid, citric acid or tartaric acid based electrolytes. When membranes with cylindrical pores are utilized as the working electrode, the

deposited *Fe-Pd* alloys inherit the cylindrical void and form nano-rods or nano-tubes. To date, the membranes used for fabricating *Fe-Pd* nano-rods/tubes are porous anodic alumina (PAA) [81, 82, 83, 84] or track-etched polycarbonate (PC) [85] membrane. As the diameter of the cylindrical pore decreases, electrodeposition within the nano-void will be more challenging due to the increased difficulty of template wetting. The state of the art technology fabricated thinnest *Fe-Pd* nano-wire was 20 nm in diameter, synthesized from the sulfosalicylic acid based bath (pH=5) by AC deposition in PAA template [81]. Under such deposition conditions (AC 25 V, 50 Hz), Fe atomic fraction up to 60 at.% was achieved. However, there was no clear result showing any relationship between the AC deposited *Fe-Pd* alloy stoichiometry and deposition parameters. Larger *Fe-Pd* nanorods/tubes up to 300 nm in diameter were fabricated by galvanostatic deposition [86],potentiostatic deposition [85] or galvanostatic pulse deposition [83].

The existing work on *Fe-Pd* electrodeposition shows that DC and pulse deposition have better control over the *Fe-Pd* alloy average composition than AC deposition. The average Fe at.% of the deposited alloy clusters can be readily modulated by changing the current density/overpotential in DC and pulse deposition without changing the composition of the plating bath. However, Jeon *et al.* [83] reported that a composition gradient along the length of a single *Fe-Pd* nano-rod grew by galvanostatic DC technique exists. They proved that such variance along the length of the *Fe-Pd* nanowire can be resolved by using galvanostatic pulse deposition technique (pulse on and off time for 0.5 s each) . When the effective electrode area is hard to measure, the potentiostatic pulse technique seems to be more frequently applied. Haehnel *et al.* [82, 87] synthesized 70 nm *Fe-Pd* nanorod in PAA with potentiostatic pulse deposition technique from 5-ssa based electrolyte at pH 5. In their study, a cathode potential E_1 was applied for 60 s during which the reduction of metal ions occur. A more positive potential E_2 (-0.5 V, -0.3 V or -0.1 V) was then applied at the successive resting step for 180 s to allow the recovery of ion depletion during the deposition step and to release any gas bubble caused by hydrogen evolution. By adding this resting step, the homogeneous filling of the nanowire was obtained and the $E_2 = -0.1V$ generated the solid continuous single

phase Fe-Pd nanowire.

The crystal structure of the alloys formed by electrodeposition might not be the same as what is formed metallurgically. Slight variations of crystallographic structure exist between alloys deposited from different plating baths and techniques. Several researchers found out that different phases exist in the as-deposited Fe-Pd alloy at different stoichiometries. Doi [79] measured X-ray diffraction pattern for Fe-Pd alloys of various stoichiometries and reported the structure evolution of Fe-Pd thin films deposited from tartaric acid based bath onto the copper electrode using the galvanostatic technique. The as-deposited film was of $\alpha - Fe$ solid solution when the Pd at.% is lower than 14.3 at.%. When the Pd fraction ranges from 28.5 at.% to 61.6 at.%, the crystal structure is a mixture of α-Fe solid solution and (γ-Fe,Pd) fcc solid solution. When the Pd atomic fraction increases to 69.5 at.%, the deposited Fe-Pd film exists as the (γ-Fe, Pd) fcc solid solution. Haernandez [80] reported that Fe-Pd thin films deposited from a citric acid based bath onto an Au electrode exhibits the bcc phase when the Pd fraction varies from 18 at.% to 26 at.%. When the Pd fraction is 62 at.% the Fe-Pd $L1_0$ phase exists. And the film structure shows fcc phase when the Pd fraction is up to 81 at.%. Haehnel [87] reported that the Fe-Pd nano-rod deposited from a 5-ssa based bath into PAA with potentiostatic pulse technique shows the bcc structure at 30 at.% Pd. These results suggest that as the Fe at.% increases in the alloy, as-deposited Fe-Pd alloy structure will evolve from fcc phase to mixed bcc and fcc phase and finally to bcc phase. The Fe at.% threshold for the appearance of bcc phase and disappearance of fcc phase might vary with different plating conditions.

As-deposited $Fe_{70}Pd_{30}$ might exist as a single bcc solid solution phase [87, 88] or α-Fe and Fe-Pd mixed phase [79] depending on different deposition conditions. Therefore annealing at high temperature (1043 K for bulk Fe-Pd based on the equilibrium diagram) is necessary to form a single phase fcc (γ-Fe,Pd) solid solution. Wang [88] presented for the first time the fcc-fct reversible phase transformation for Fe-Pd alloys fabricated by the electrodeposition method. The thin film was deposited from a tartaric and citric acid based plating bath on Pt electrode with galvanostatic deposition technique. The as-deposited $Fe_{70.2}Pd_{29.8}$ thin film

had a single bcc structure. After annealing at 900 °C for 45 min encapsulated inside a vacuum quartz tube, the sample was quenched in ice water to prevent equilibrium phase separation of $Fe_{70.2}Pd_{29.8}$ to α-Fe and Fe-Pd mixed structure. Their *in situ* temperature changing XRD measurement shows a narrow temperature hysteresis of fcc-fct phase transformation of about 10 °C and a martensite starting temperature at -30 °C.

Chapter 3

EXPERIMENTAL PROCESSING OF FE-PD NANOHELICES

In order to obtain the designed $Fe_{70}Pd_{30}$ linear nanoactuator, the spring of this actuator need to have good geometry as a mechanical spring and also possess a martensite phase transformation with a precise atomic composition. Therefore the geometry control and the composition control are the two key parameters in the synthesis procedure. Considering the practicability and cost efficiency, the following two template-based methods are conducted for Fe-Pd nanospring fabrication: (1) Synthesis of Fe-Pd nanohelices by Si template; (2) Synthesis of Fe-Pd nanohelices by PAA-SiO_2 hybrid template.

3.1 Synthesis of Fe-Pd Nanohelices by Si Template

Formation of helical holes in single crystal Si wafer by Pt nanoparticle assisted chemical etching was first observed by Tsujino *et. al.* [89]. Pt particles are generated on top of Si wafer by electroless chemical deposition ($PtCl_6^{2-}(aq) + Si^0(s) + 6F^-(aq) = Pt^0(s) + SiF_6^{2-}(aq) + 6Cl^-(aq)$). Such Pt serves as catalyst and accelerated the etching of the Si wafer in HF/H_2O_2 etchant (metal cathode reaction: $H_2O_2 + 2H^+ -> 2H_2O + 2h^+$, $2H^+ + 2e^- -> H_2\uparrow$; anode reaction: $Si + 4h^+ + 4HF- > SiF_4 + 4H^+$, $SiF_4 + 2HF- > H_2SiF_6$; Overall reaction: $Si + H_2O_2 + 6HF- > 2H_2O + H_2SiF_6 + H_2\uparrow$ [90]). When the HF/H_2O_2 ratio is high, helical pores are generated instead of straight cylinders which might be attributed to the microscopic difference in etching rate on different locations of Pt catalyst. The resulted helical hole diameter is identical to the diameter of the Pt catalyst which is related to the electroless deposition time. Such helical pores can be used as the template to be backfilled with Fe-Pd ionic solutions. During a thermal reduction procedure, the Fe and Pd cations were reduced and they form alloy at high temperature.

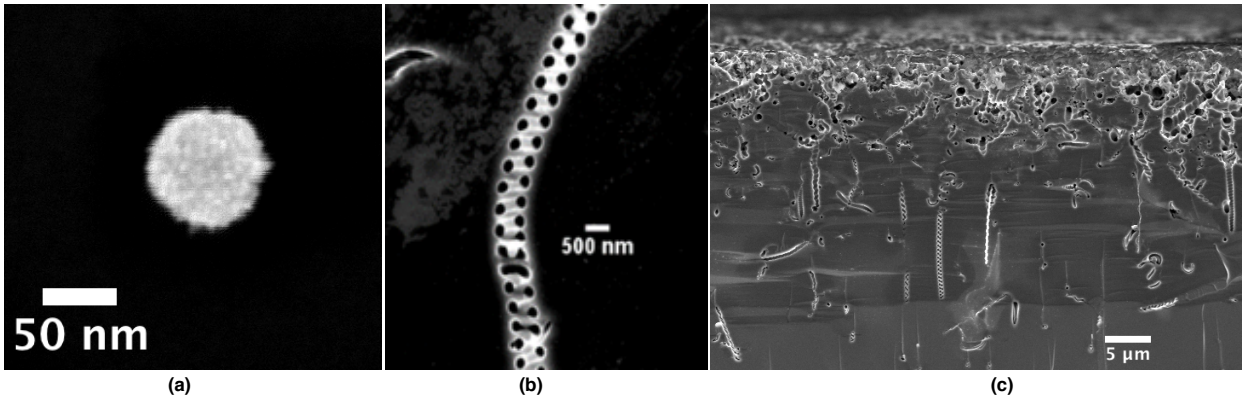

Figure 3.1: (a) Single Pt nano particle (78 nm in diameter) formed on top of Si wafer by electroless deposition. (b) Cross section of a single helical hole on Si wafer at the etchant composition of 52.2 M [HF], 3 M [H_2O_2] (pore diameter, outer loop diameter and pitch is 220 nm, 700 nm and 480 nm , respectively). (c) Cross section view of helical pores born in Si wafer.

3.1.1 Fabrication of Si Template with Helical Pores

n-type $\langle 100 \rangle$ Si wafer (ρ= 90-120 ohm-cm,Shin-Etsu handoutai, Inc) was subsequently cleaned in acetone (ultrasonic bath) for 5minutes, deionized water (DIW) for 10minutes, a CP-4A etchant which is composed of 49.2% HF:69.5% HNO_3: CH_3COOH =3:5:3(V) for 5 minutes, and 7.3 mM HF for 5 minutes. Then the electroless deposition of Pt is carried out in dark by immersing the pre-treated Si wafer in the aqueous solution consist of 1mM H_2PtCl_6 and 15 mM HF. Then the Si wafer is cleaned by soaking in DIW for 2 min. The Pt assisted etching of Si was conducted in the dark in an aqueous solution of 52.2M [HF] and 3M[H_2O_2]. After the etching process, the Si wafer was cleaned with DIW and ethanol. The sample was then cleaved into halves, exposing the cross section for SEM imaging.

The generated Pt particles by the above electroless deposition are spherical particles with bumpy surface sitting on the Si surface (shown in Fig. 3.1(a)). The relationship of the deposited Pt catalyst diameter and the deposition duration is shown in Fig. 3.2(a). As the electroless deposition duration increases from 5 min to 120 min, the average diameter of Pt particles increases from 77 nm to 282 nm. The standard deviation (the vertical bar

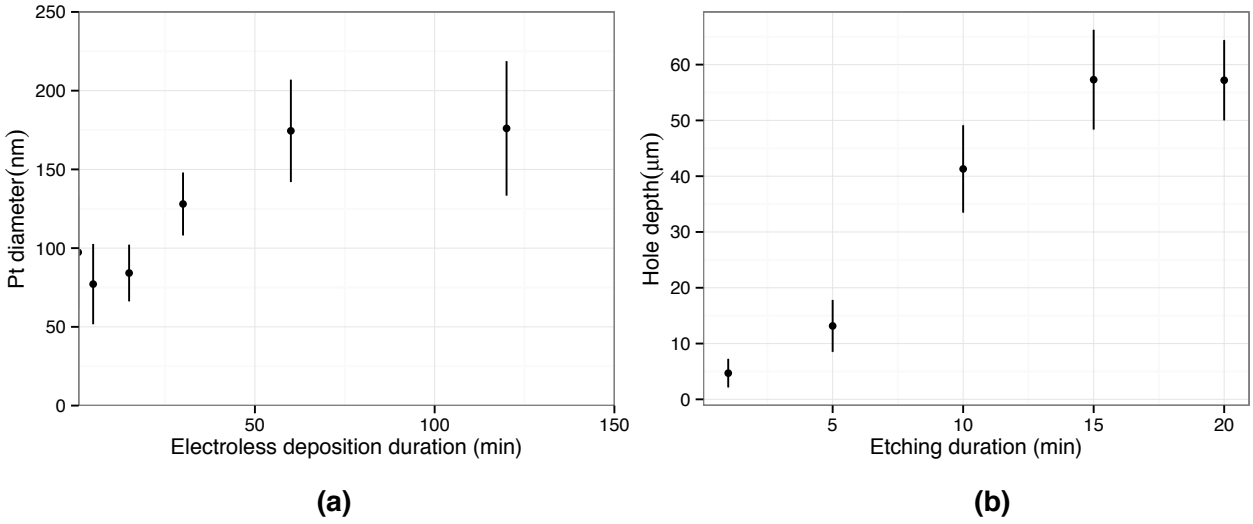

Figure 3.2: (a) The effect of electroless deposition duration on the diameter of Pt catalyst particles. (b) The effect of etching duration on the depth of helical pore in Si wafer (The average Pt catalyst diameter in this study is 80 nm).

in the plot) indicates that there is a large variance for Pt catalyst particles generated in each condition and the variance become larger for longer electroless deposition duration. Such variance in Pt catalyst size results in the same variety of helices with different pore diameters. A typical SEM image in Fig. 3.1(b) shows the helical holes generated with Pt assisted etching of Si. The average length of the helical holes inside Si wafer increases with increasing etching duration. It reaches the maximum value of 57 µm (Fig. 3.2(b)). Fig.3.1(c) shows the enlarged view of helical pores in Si. The shape of the pores ranges from curved cylinders to helical pores. The preferred direction of the helical pore is along the thickness direction of the Si wafer.

3.1.2 Back filling of Fe-Pd by Ion Reduction

Si wafer with helical pore etched in 52.2 M $[HF]$ and 3M$[H_2O_2]$ for 20 min were thinned down to 50 µm by mechanical polishing to make open helical holes on both ends. Then

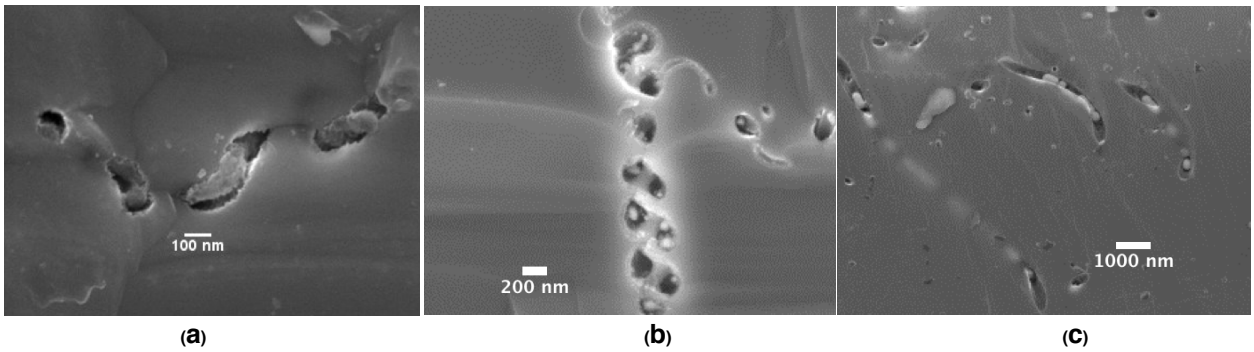

Figure 3.3: SEM cross-sectional view of (a) *Fe-Pd* segments in helical pore. (b) *Fe-Pd* beads in helical pore. (c) *Fe-Pd* segments in curved pores.

the Si template was cleaned with DIW and ethanol and put inside the vacuum chamber (on the order of $10^{-7}Pa$). A precursor solution containing 0.2 M $Fe(acac)_2$ and 0.0878 M $Pd(acac)_2$ in triethylene glycol was injected into the vacuum chamber and completely immerse the template. After 30 min, the template in precursor solution was brought to the ambient environment and kept stirring in precursor solution for 48 h. In the end, the sample with precursor solution was heated at 850 °C for 15min in Ar/5 $\%H_2$ by microwave (Microwave Generator Unit MMG-213V-2P, Micro-Denshi Co. Ltd). The filling condition was characterized by SEM.

The filling condition of *Fe-Pd* in helical pores are shown in Fig. 3.3. Once the solvent evaporated, the volume of reduced metal ions is smaller than the original liquid volume filled in the nanopores, leading to the partial filling of the pores. Only small segments of *Fe-Pd* nanowires or *Fe-Pd* beads are obtained with the ionic reduction at elevated temperature. This processing route was proved not suitable for fabrication of *Fe-Pd* nanosprings due to the poor filling condition.

3.2 Synthesis of Fe-Pd Nanohelices by PAA-SiO_2 Hybrid Template

Fe-Pd nanohelices can be fabricated by electrodeposition with $PAA-SiO_2$ hybrid template. Fig.3.4 illustrates the flowchart for the whole scheme. A PAA thin film (500 nm to 1000

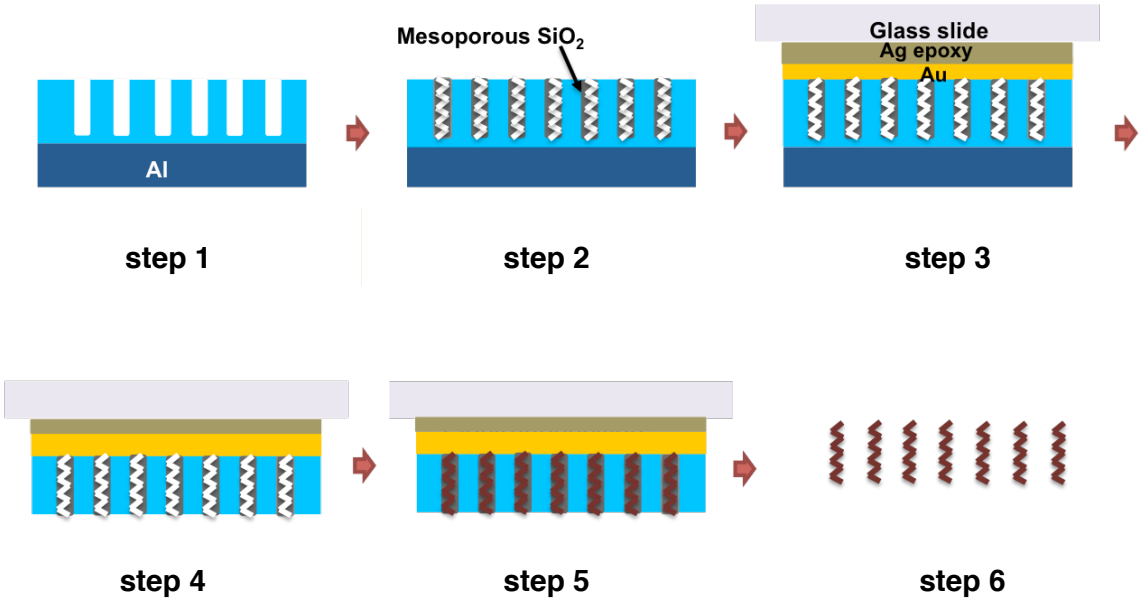

Figure 3.4: Schematic illustration for the electrodeposition of Fe-Pd alloy in $PAA - SiO_2$ hybrid template. Step 1. synthesis of PAA membrane, Step 2. synthesis of $PAA - SiO_2$ hybrid template, Step 3. fabrication of laminate electrode, Step 4. removal of back Al and Al_2O_3 barrier layer, Step 5. electrochemical deposition of Fe-Pd alloy, Step 6. Release of Fe-Pd nano-helices.

nm thick in this work) is synthesized by the well-known two-step anodization method [91], providing hexagonal packed highly uniform cylindrical nanopore arrays. Then the SiO_2 sol is injected into the PAA pore by dip coating. After gelation, mesoporous SiO_2 with different shapes of nanoholes is formed confined inside PAA. To prevent the damage of brittle PAA film during the back Al and barrier Al_2O_3 layer removal step, a 200 nm conductive Au layer is sputtered onto the open end of the PAA pores, and the $Au|PAA - SiO_2|Al$ layers are attached to glass slide by silver epoxy (approximately 30 µm in thickness). The probe of electrochemical workstation will be attached to conductive silver epoxy by copper tape. Later on, the back Al and barrier Al_2O_3 layer are fully removed to make a path to the Au contact surface and $Fe\text{-}Pd$ plating bath. Then $Fe\text{-}Pd$ can be electrodeposited inside the nanovoid and finally be released after the template is etched.

3.2.1 Fabrication of Porous Anodic Alumina (PAA)

Porous anodic alumina (PAA) was synthesized by two-step anodization first developed by Masuda and Satoh [92]. In addition, a third anodization in phosphoric acid was conducted to make the barrier layer thinner. Anodization experiment was conducted using a homemade $Teflon^{TM}$ Cell (shown in Fig.3.6). The three-step anodization procedure is illustrated as follows: The pre-treament of Al foil (Fig. 3.5 (a)) includes the following steps. The 99.9995% pure aluminium foil 0.13 mm) is first degreased in acetone by ultrasonic bath for 5 min to remove organic residuals. Then electropolishing at voltage of 20 V is conducted in a 95 vol.% H_3PO_4 (85 wt.%), 5 vol.% H_2SO_4 (95 wt.%), 20 g/L CrO_3 solution for 30 seconds at 85 °C. After electropolishing, the aluminium foil is washed with DI water then soaked in a 3.5 vol.% H_3PO_4 (85 wt.%), 45 g/L CrO_3 solution for 3 min at 95 °C. Then the aluminum foil is cleaned by DI water and dried by compressed Ar gas. The first aluminium anodization (Fig. 3.5 (b)) was carried out at a constant voltage of 40V for 10 hours in 0.3 M oxalic acid at 15 °C. The porous alumina formed in the first anodization step was completely removed by immersing the sample foil into a 6 wt.% phosphoric acid and 1.8 wt.% chromic acid solution for 14 hours at 60 °C (Fig. 3.5). The second anodization step was carried in

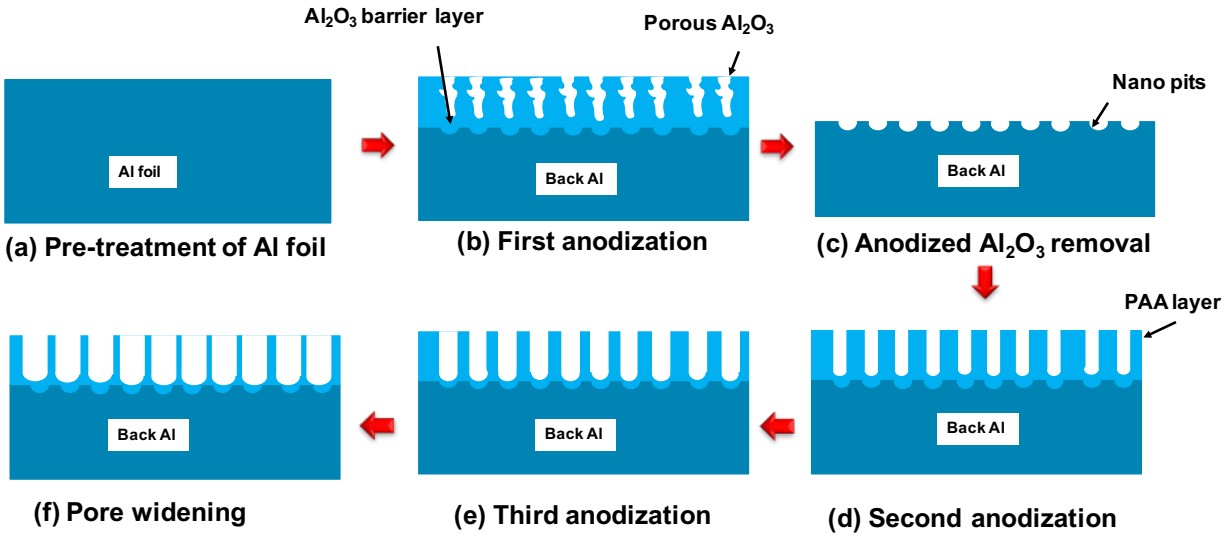

Figure 3.5: Schematic illustration for the three-step anodization procedure of PAA. (a) Pre-treament to clean the surface of Al foil. (b)The first anodization generates disordered nanopores. (c) The disordered nanopores are removed to leave nanopits on Al. (d) The second anodization generates hexagonal packed nanopores. (e) The third anodization decrease the barrier layer thickness and widens the pore. (f) Post pore-widening produces nanopores with adjustable diameters.

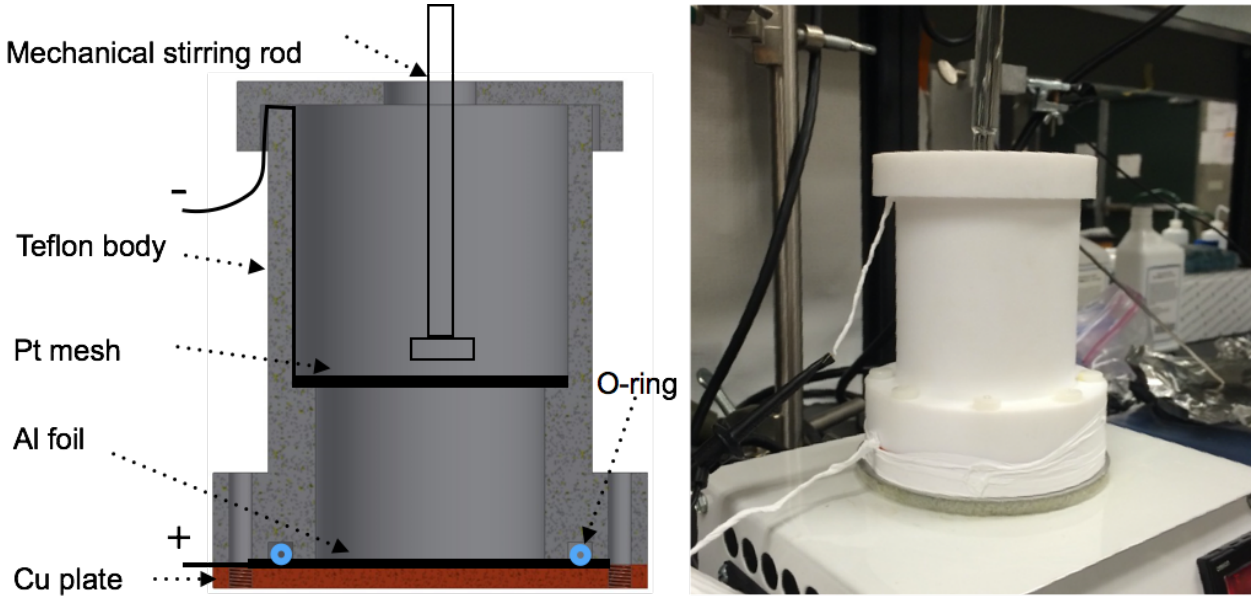

Figure 3.6: Experimental setup for PAA anodization.

the same condition of the first anodization but for 10 min to get a thin layer of ordered PAA structure. A third anodization in 0.2 M Phosphoric acid was conducted for 10 min at 15 °C to widen the PAA pore diameter and at the same time to decrease the barrier layer thickness. This lab-made PAA template was then used as the confining template to synthesize porous SiO_2 by Sol-gel method.

After the above three anodization steps, a very brittle transparent film (PAA) is formed on top of the Al foil. SEM observations show the honeycomb structure of the nanopores from the top view in Fig.3.7. The side view for PAA layer shows cylindrical pores in the direction of Al thickness. Each pore is standing individually without interrupting with each other. The thickness of PAA layer is determined by the 2nd anodization duration. In our study, we typically use PAA with the thickness of less than 1µm. The average pore size is 29.7 nm (SD=5.12 nm), the inter-pore distance is 110nm, and the thickness of alumina barrier layer at the bottom of such nano-pore generally range from 40 nm to 60 nm. To expand the pore size, the hole-widening can be carried out by etching the as-anodized PAA in 5wt.% H_3PO_4.

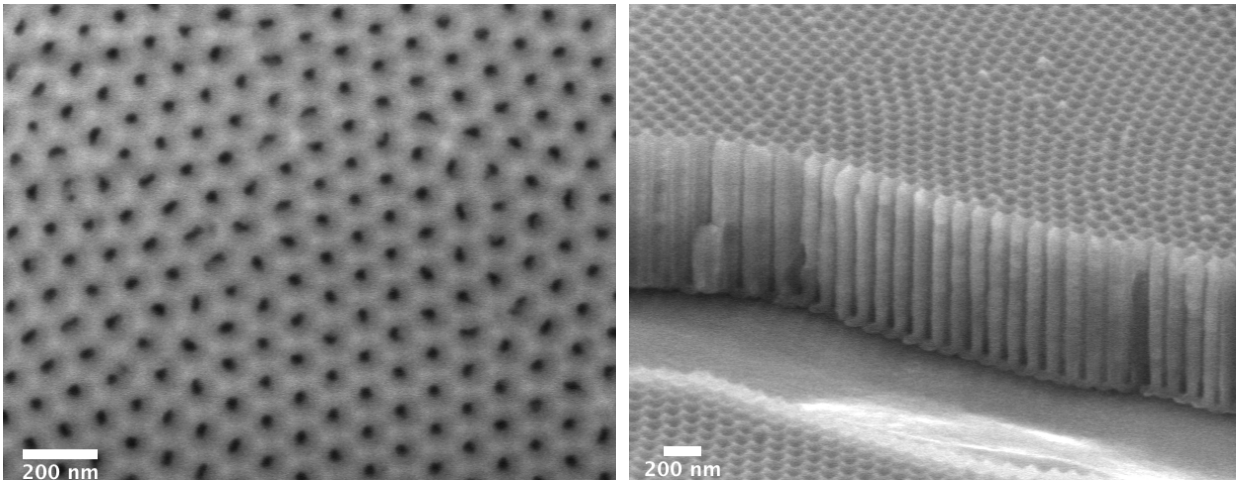

Figure 3.7: SEM images of as-synthesized PAA after three anodization steps. (a) Top view showing a hexagonal arranged pore structures. (b) Cross section view showing cylindrical pores standing individually along the thickness direction of PAA membrane.

Since the wet chemical etching in H_3PO_4 is isotropic, the diameter of the cylindrical pores increase simultaneously along the length. The influence of etching duration in H_3PO_4 on pore size of PAA is shown in Fig.3.8. The diameter of the cylindrical pores is measured by the SEM cross-section view of PAA etched in phosphoric acid for a various duration. It is clear that the PAA pore diameter increase with longer etching time. The median of the as-anodized PAA pore is 29 nm while it reach to 66 nm at 50 min etching (Fig. 3.8). This lab-made PAA template was then used as the confining template to synthesize porous SiO_2 by Sol-gel method.

3.2.2 Fabrication of Porous Anodic Alumina (PAA)-Mesoporous Silica Hybrid Template

In a typical experiment, 10.4 g tetraethylorthosilicate (TEOS) was mixed with 5.4 ml HCl (pH = 2) and 15.21 ml ethanol under vigorous stirring by $Teflon^{TM}$ coated magnetic stirrer bar for 20 min at room temperature. Then the prehydrolyzed silicon alkoxide was mixed

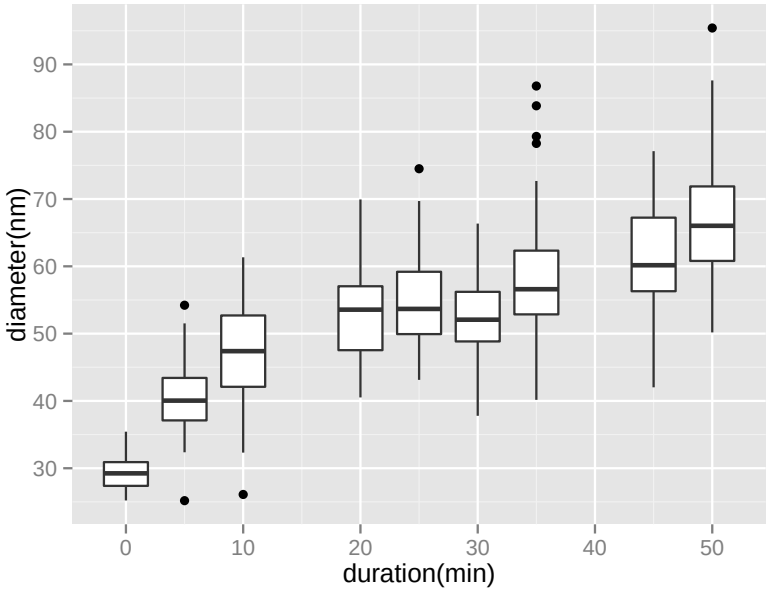

Figure 3.8: Relationship between PAA nano-pore size and the etching duration in 5 wt.% H_3PO_4 aqueous solution at 25°C.

with 2.73 ml $EO_{20}PO_{70}EO_{20}$ in 10.14 ml ethanol for 3 hours at room temperature. Later on this Si containing Sol infiltration into PAA nanopore was conducted by dip coating at a constant speed at room temperature. (The dip coating withdraw speed was modified to adjust the thickness of excess silica layer, see section 3.2.3). The PAA/Al template was then moved into environment chamber with relative humidity of 66% at 25 °C for 24 hours. Porous SiO_2 network was then further developed and triblock copolymer was removed by calcination at 500 °C in air for three hours (ramp rate 1 °C/min).

Fig.3.9 shows that the sol infiltrates into PAA nano-pores and form cylindrical nano-rods after polymerization. Further investigation of the free-standing SiO_2 rod under TEM indicates that hollow holes distribute along the body of silica rods, Fig.3.9(b). These hollow helical holes with small helical angle are 11 nm in diameter. In the electrodeposition step, Fe-Pd wires grow from the end of the hole which is in contact with Au conducting layer and inherit the geometry of the hollow holes.

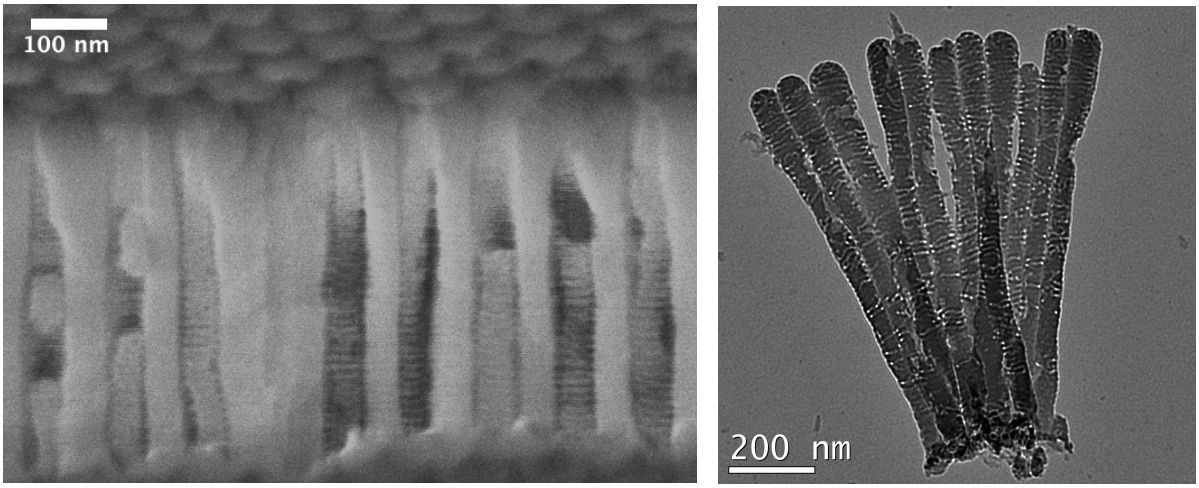

Figure 3.9: Electron microscopy images of porous silica confined within the PAA nanopores, (a) SEM profile of SiO_2 template which was made inside PAA. The cross section was exposed by cutting $PAA - SiO_2$ template with razor blade. (b) TEM image of free standing SiO_2 template with nanohelical holes. The porous SiO_2 nanorods were released from PAA template by etching in 5 wt.% H_3PO_4 aqueous solution.

3.2.3 Excess SiO_2 Layer Removal

As is shown in Fig.3.4 step 3, an Au layer is deposited onto the opening side of the PAA-SiO_2 hybrid template as the conducting layer for electrodeposition. The electric path from the bulk electrolyte to the Au interface must be clear to ensure the Fe-Pd deposition. However, during the sol infiltration by dip coating, excess silica sol that does not penetrate into the PAA pores forms an uneven mesoporous SiO_2 layer on the top surface of the PAA template after calcination. Fig.3.10 indicates the top view of a PAA-SiO_2 template after the sol-gel process, showing the region where PAA pore is exposed and the region covered by excess mesoporous SiO_2 layer. Profile of the unexposed region (Fig.3.10(b)) indicates that the entrance of PAA pores is covered with the excess SiO_2 layer. Such excess SiO_2 layer disrupts the direct contact of the conductive Au layer with the helical hole entrance, resulting in a low filling rate of the template. The thickness of the excess SiO_2 layer is

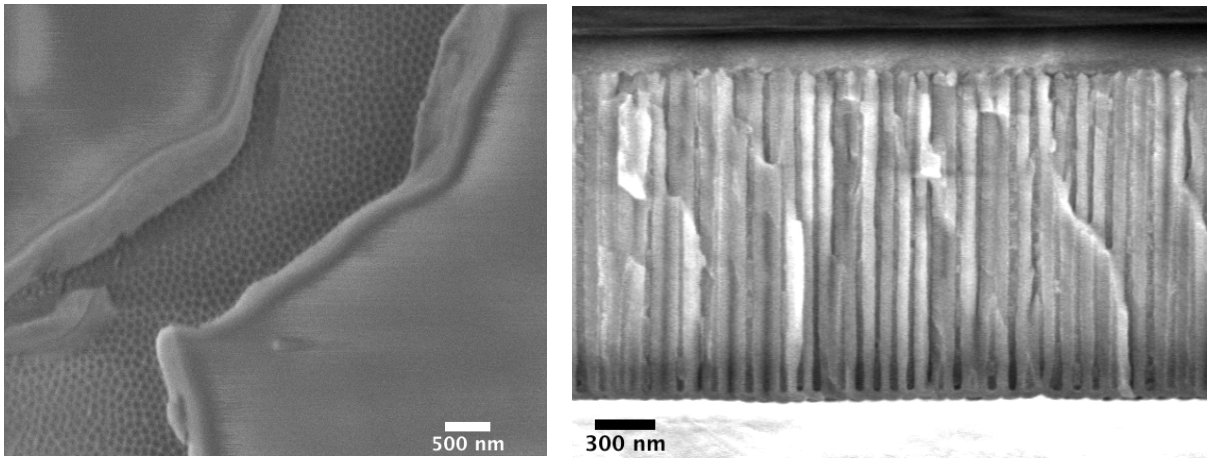

Figure 3.10: SEM images of excess SiO_2 on PAA surface (a) top-view and (b) cross-section view.

determined by the SEM cross-section view of $PAA-SiO2|Al$ layers after sol-gel infiltration. A highly scattered thickness across the template shows an average thickness of 297 nm and large variance of 535.5 nm (39 spots measured in total). The minimum thickness is 0 nm while the maximum value can reach as high as 2.5 µm.

50 nm Al_2O_3 was used as the abrasive for the mechanical polishing of excess SiO_2 layer. Owing to the large variance of excess SiO_2 thickness, the PAA-SiO_2 template can be easily damaged during the polishing process since the Al_2O_3 abrasive is in direct contact with the exposed area of the fragile PAA layer before the thicker SiO_2 layer is removed. Fig. 3.11 shows the PAA-SiO_2 template top view after mechanical polishing. There is no sign of any excess SiO_2 left after mechanical polishing. However, collapse and breakage of the PAA are often observed. Although it is theoretically possible to use mechanical polishing to remove excess SiO_2, it is practically time-consuming and low in success rate to produce faultless template. Other methods including wiping the PAA-SiO_2 top surface before full gelation to remove excess Sol precursors, or changing dip coating to spin coating for silica sol infiltration were also tried to remove this excess SiO_2. However, complete excess silica removal have not

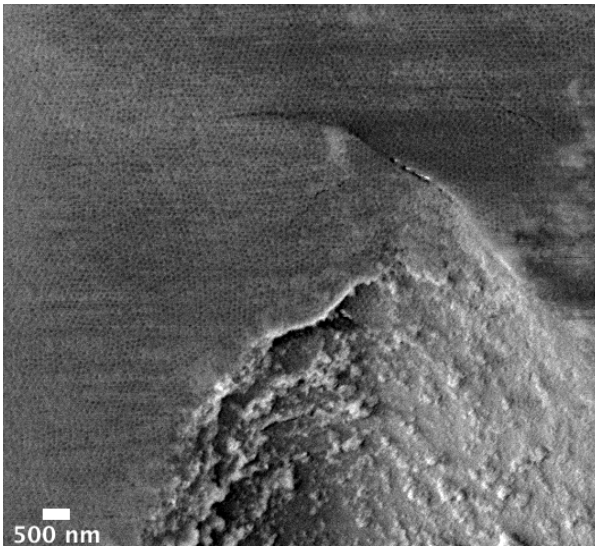

Figure 3.11: SEM image of $PAA - SiO_2$ template top surface after mechanical polishing.

been achieved.

The main challenge with excess silica removal is the large variance of its thickness. Since the thickness of SiO_2 inside PAA pore is usually from 500 nm to maximum 1 µm, it is difficult to remove the excess SiO_2 (min, max=(0, 2.5) µm) while preserving SiO_2 inside the pore at the same time. Therefore, thinner excess silica with smaller variance needs to be made before full gelation. The relationship between excess SiO_2 thickness distribution and dip coating withdrawal speed is studied for this purpose.

Three pieces of 1 cm by 1 cm $PAA|Al$ sheets synthesized under the same conditions were withdrawn from the same silica sol of 24 mm/min, 48 mm/min and 120 mm/min respectively. After template aging and calcination, the templates were cut by razor blade to expose the cross-section for SEM imaging. Measured excess SiO_2 thicknesses on different positions of one sample with respect to different withdrawal speed is plotted in Fig. 3.12. In a boxplot, the upper and lower hinges correspond to the first and third quartiles. The upper vertical bar extends from the hinge to the highest value that is within 1.5 times inter-quartile range (IQR) of the hinge. The lower vertical bar extends from the hinge to the lowest value within

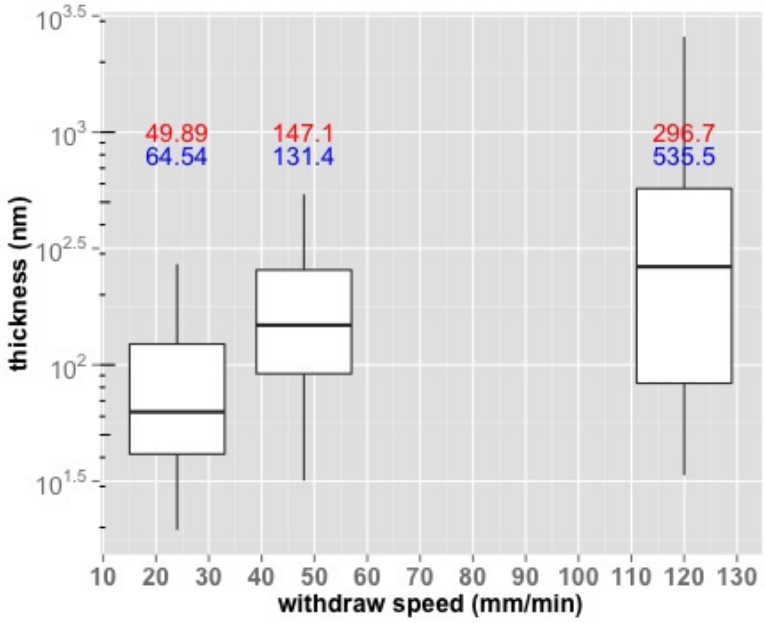

Figure 3.12: The effect of dip coating withdrawal speed on excess SiO_2 thickness (sample size for withdrawal speed of 24, 48 and 120 mm/min are 49, 45 and 39, respectively).

1.5 times IQR of the hinge. Data beyond these range is plotted as dots. The mean value and standard deviation is marked in red and blue separately for each condition. Fig. 3.12 indicates that as the withdrawal speed decreases from 120 mm/min to 48 mm/min then to 24 mm/min, the mean and standard deviation of the excess silica layer thickness decrease from 296.7 nm and 535.5 nm to 147.1 nm and 131.4 nm then to 49.89 nm and 64.54 nm. A thinner and more uniform excess SiO_2 layer is obtained using a 24 mm/min withdrawal speed.

Sample dip coated at 24 mm/min was further etched by reactive ion etching (RIE) (pressure 75 mTorr, radio frequency (RF) power 50 W, base pressure 75 mTorr, oxygen flow 5 sccm, CHF_3 flow 25 sccm) to remove the excess SiO_2 layer. Fig.3.13(c) shows that after etching by RIE for 5 min, the mean and standard deviation of the excess silica thickness decrease to 10.84 nm and 25.28 nm. And the median and 75th percentile of excess SiO_2 thickness reaches 0 nm (N=44), indicating that most $PAA - SiO_2$ template surface is ex-

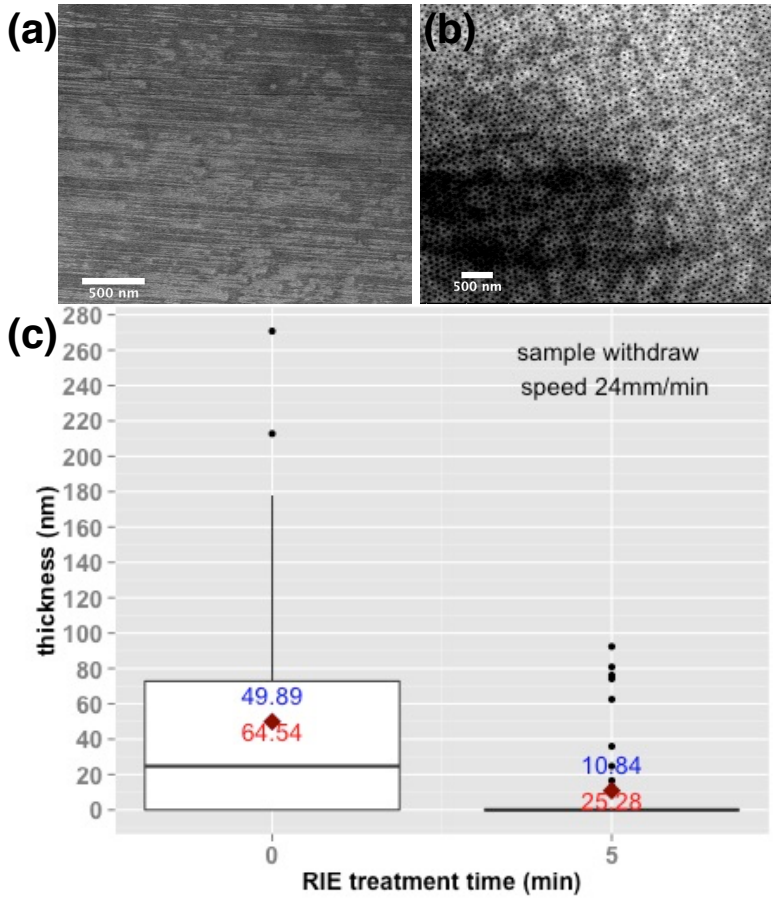

Figure 3.13: (a) top-view of PAA-SiO_2 template dip coated at withdrawal speed of 24 mm/min after full gelation (b) top-view of PAA-SiO_2 template dip coated at withdrawal speed of 24 mm/min after full gelation followed by a 5 min RIE treatment, and (c) the effect of RIE treatment on excess silica thickness for PAA-SiO_2 template dip coated at 24 mm/min.

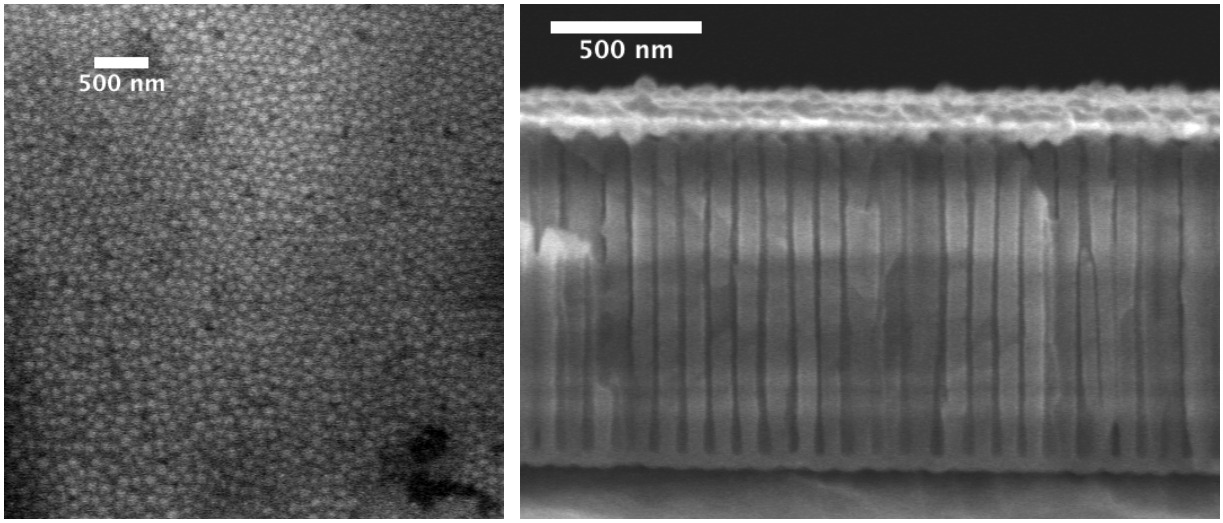

Figure 3.14: SEM images of (a) PAA-SiO_2 template viewing from alumina barrier layer side after removing back Al (b) cross section view of PAA-SiO_2 template sputtered with Au layer. From top to bottom shows the 200 nm Au layer, the PAA-SiO_2 hybrid template layer and a 40 to 60 nm thick alumina barrier layer.

posed without sacrificing too much SiO_2 inside the PAA pore. Fig.3.13(a) and (b) shows the top surface of PAA-SiO_2 template dip coated at 24 mm/min before and after RIE treatment. It verifies that excess silica layer is cleared by RIE for 5 min.

3.2.4 Fabrication of PAA-SiO_2 Working Electrode

After the excess SiO_2 layer is completely removed, a 200nm Au layer is sputtered on top of the PAA pore opening side. Such $Au|PAA-SiO_2|Al$ laminar structure is attached to glass slide by silver epoxy (Fig.3.4 Step 3). Following that, the back aluminum layer is removed by 1M $CuCl_2$, exposing a Al_2O_3 barrier layer ranging from 40 nm to 60 nm in thickness, as is shown in Fig.3.14. This barrier layer needs to be completely removed to ensure that the electroplating electrolyte penetrates into helical nanoholes. $5wt.\%H_3PO_4$ acid was used to etch away the dome shape barrier layer gradually at room temperature without stirring.

The barrier layer opening condition was monitored by SEM image. Fig.3.15 shows that

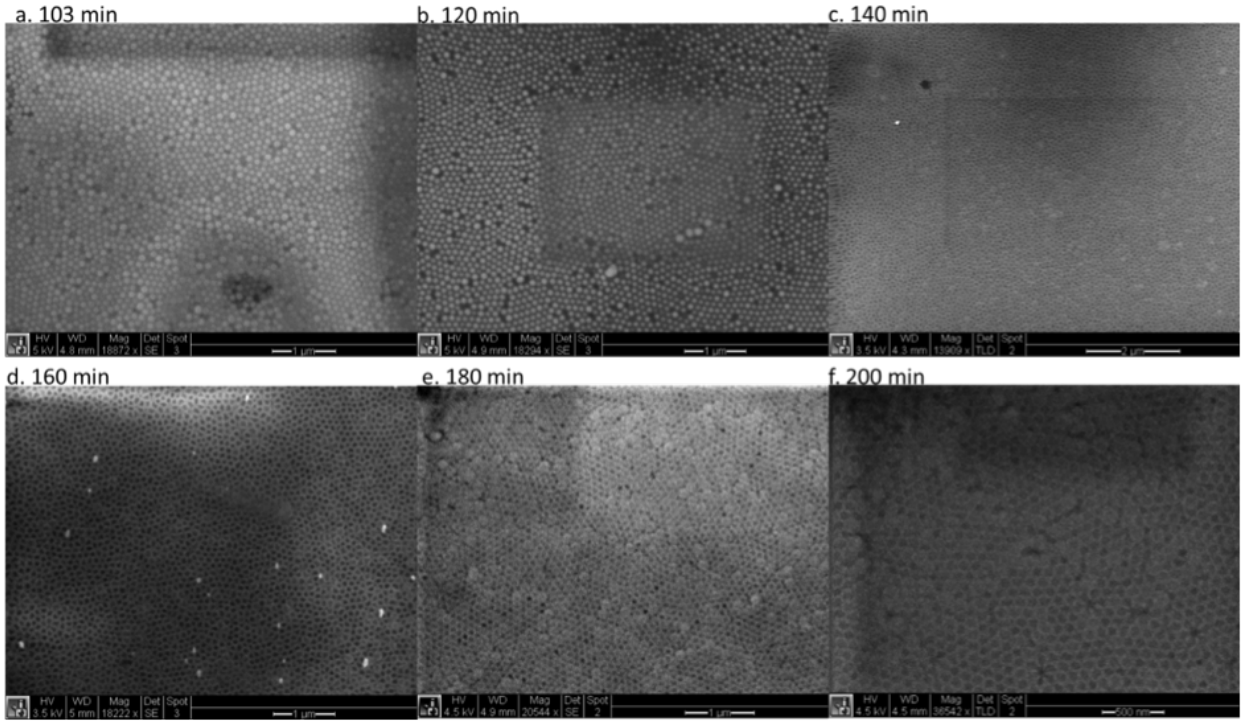

Figure 3.15: Barrier layer removal with respect to etching duration for $PAA - SiO_2$ hybrid template in 5 wt.% H_3PO_4, (a) 103 min, (b) 120 min, (c) 140 min, (d) 160 min, (e) 180 min, (f) 200 min.

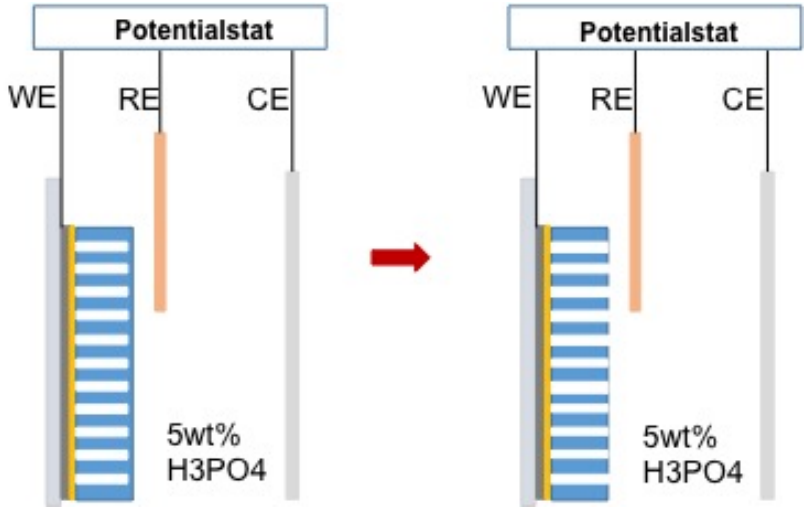

Figure 3.16: Schematic setup for barrier removal monitoring by electrochemical method.

with increasing etching time, the opening pores start to show up in the SEM image after 140 min. Before this full opening status, the dome shape barrier layer still exists for most of the pores (Fig.3.15(a), (b)). However, it is hard to tell the exact hole opening moment because of the resolution limitation of SEM. Further acid etching after 140 min ensures the full opening of all pores. Pore widening happens after full removal of barrier layer (Fig.3.15(d) (e) (f)).

By SEM monitoring, the nano-pore opening time can be determined to be between 140 min and 180 min. If the etching time is not long enough for the full opening of all holes, the filling rate of Fe-Pd nanohelices would be low. On the other hand, if the etching time is too long, the PAA will be over-etched, and a gap between confined SiO_2 and PAA might form. Such gap needs to be avoided since it might cause extra Fe-Pd deposition inside if it propagates to the Au layer. Excessive soaking in 5 wt.% H_3PO_4 solution also increases the possibility of delamination of the Au layer from PAA-SiO_2 layer. Thus a more reliable, accurate and real-time monitoring method needs to be used to determine the pore opening time in 5 wt.% H_3PO_4.

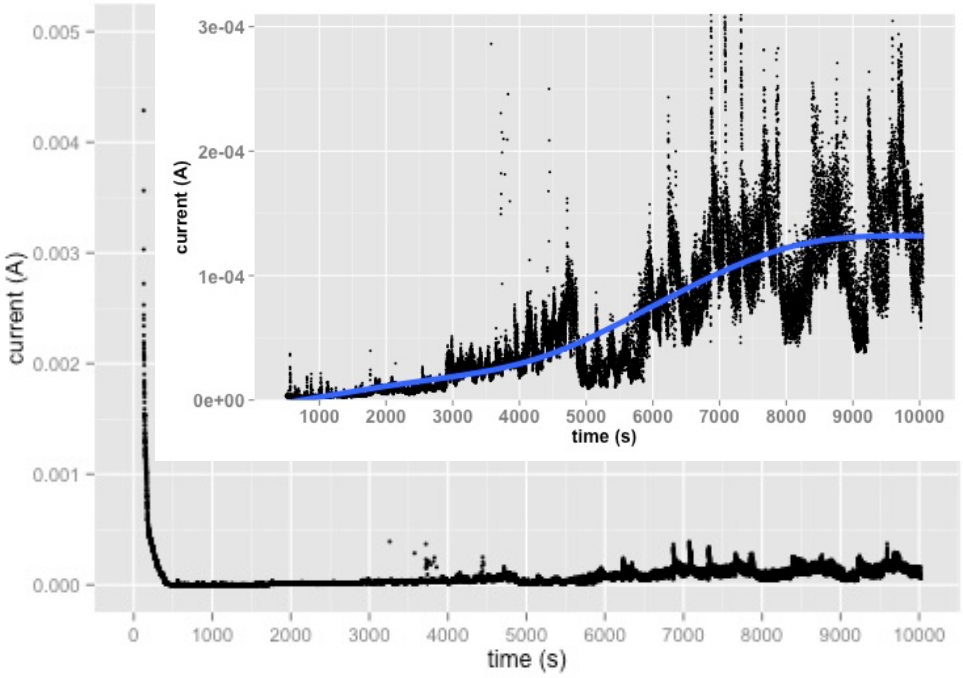

Figure 3.17: Current transient curve for barrier layer removal determination.

Real-time Electrochemical Monitoring Method

Lillo *et al.*[93] studied the pore opening behavior of PAA film by separating two-half permeation cells with a PAA membrane. Their concept can be applied in the real-time barrier layer removal in this research by designing an electric cell using the fabricated PAA-SiO_2(with barrier alumina)$|Au|Ag$ epoxy| glass slide directly as a working electrode and 5 wt.% H_3PO_4 as the electrolyte (Fig.3.16). The experiment was performed at room temperature, and the solution was stirred at 300 rpm. A constant 1 V voltage was applied to the working electrode and the current was obtained as an indication of the hole opening process. Before the barrier layer is removed, no current is expected since the electric pathway is shut off. The current increases once the barrier alumina is removed and the etchant (H_3PO_4) starts to wet the Au layer.

Fig.3.17 shows the current change over time during the barrier layer removal process. After the switch-on surge, the current maintains close to 0 A until around 3000 s. After 3000 s of etching, the current starts to rise. In order to tell the overall trend of the current change, a smoothing curve using a generalized additive model is fitted for data from 500 s to 10000 s. Fig.3.17 inset shows the zoom-in view of current change with the fitted curve after removing the inrush current. The current keeps increasing from 0 A at 3000 s to around 1.28×10^{-4} A at 7000 s. After 7000 s, the current fluctuates around 1.28×10^{-4} A. The current-time pattern predicts that the barrier layer is thinned down by 5 wt.% phosphoric acid until there is breakage at around 3000 s. After the initial breakage of the barrier layer, the nano-hole diameter keeps increasing rapidly until 7000 s.

To investigate the real pore opening condition during etching in phosphoric acid, a series of SEM photos of the barrier layer from the top-view and cross-section view were taken at 3000 s, 6000 s, 7000 s, 8000 s and 10000 s etching duration. The diameter of the opened pore size is measured as a function of etching time from the SEM top-view. Unfortunately, it is hard to detect the exact initial hole opening point because of the resolution limitation of SEM images. The pore diameter is set to be 0 nm at 3000 s since most of the pores appear covered by the barrier layer. Fig. 3.18 indicates that between 3000 s and 6000 s the hole opening starts and then the hole diameter increases. At 7000 s, the barrier layer is completely removed, and the diameter of the opened hole reaches 43 nm (median) which matches with the original diameter of the cylindrical nano-pore used in this set of experiments. After 7000 s, the hole size keeps increasing slowly which might correspond to the etching of the inner wall of PAA cylindrical pores. The trend of nanohole diameter change matches with the trend of the current change. Thus the electrochemical method can be used to monitor the real-time hole opening process and to decide precise etching time for each sample. The optimized etching time is determined to be at the turning point after a rapid increase in current.

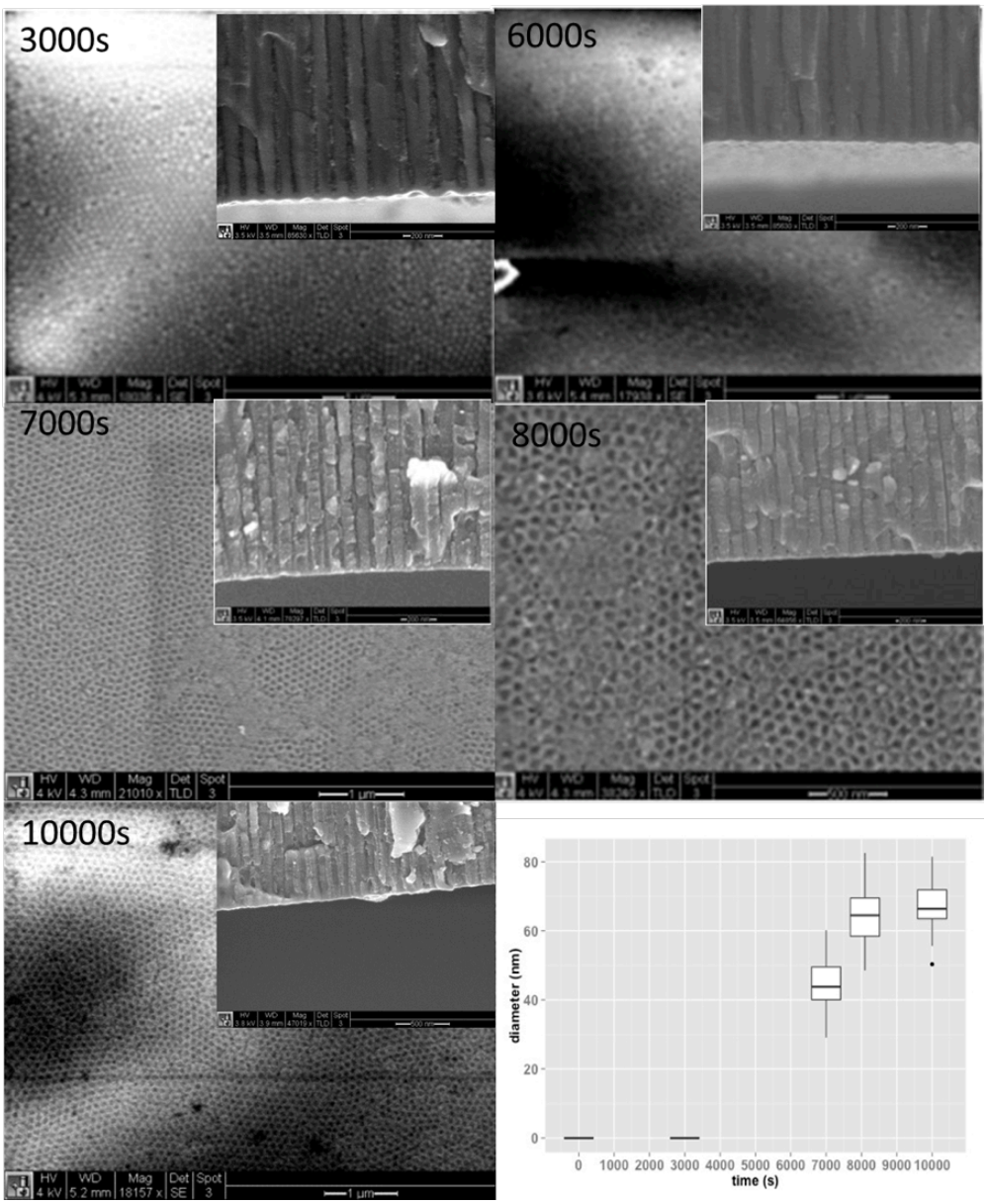

Figure 3.18: SEM images of the barrier layer removal process in 5 wt.% H_3PO_4 and the relationship between opened pore diameter and etching duration.

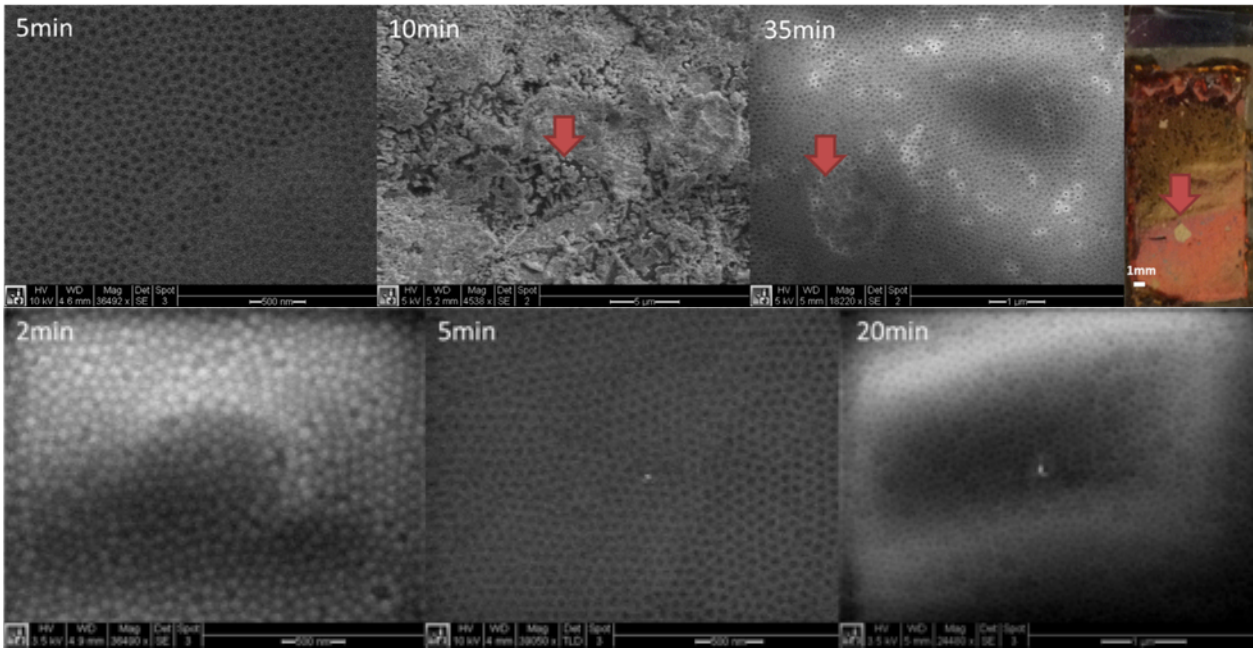

Figure 3.19: PAA-SiO_2 hybrid template viewed from barrier layer side etched at (top row) a pressure of 75 mTorr, RF power of 150 W, Ar flow of 25 sccm for various time and (bottom row) at a pressure of 75 mTorr, RF power of 100 W, Ar flow of 25 sccm.

Alternative Dry Etching Method

Besides H_3PO_4 wet chemistry etching, sputter etching was used to physically remove the top alumina barrier layer as an alternative method. PAA-SiO_2(with barrier alumina)$|Au|Ag$ epoxy| glass slide was placed in an asymmetric parallel-plate reactor in which the vertical etch rate far exceeds the lateral etch rate. Because of the anisotropy characteristic of this dry etching technique, the over-widening of nano-pores can be diminished.

Two etching conditions were tested to determine efficient removal of the barrier layer. In both conditions, Ar gas is set to be 25 sccm and the base pressure is set to be 75 mTorr. The RF power of the first set of experiments was set to 150 W. SEM images of the top view of barrier layers after RIE treatment are shown in Fig.3.19. After 5 min, the barrier layers are fully removed. Longer etching time removes more template layer and increases the surface

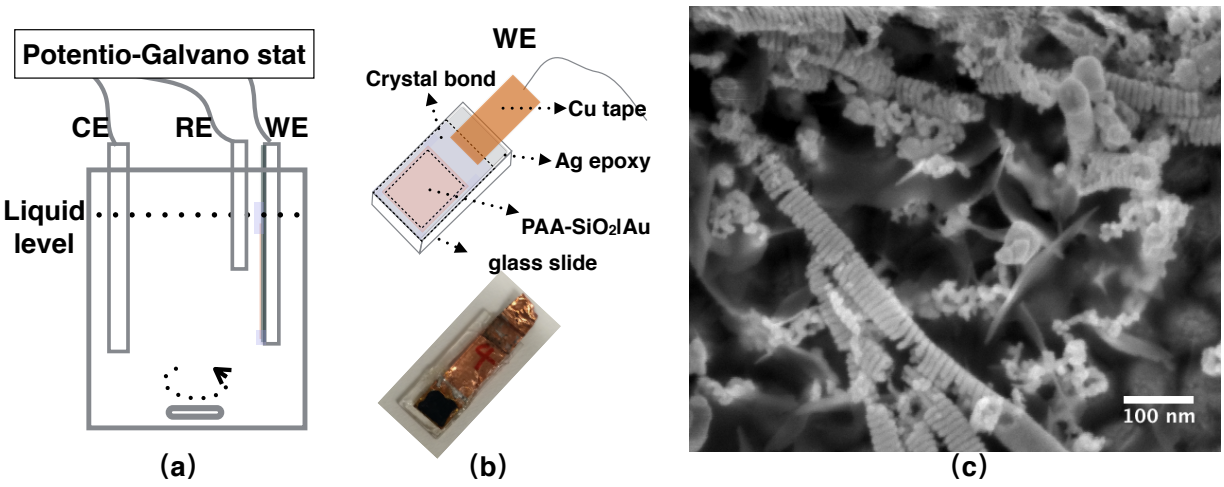

Figure 3.20: (a) Schematic illustration of electrodeposition setup; (b)Schematic illustration and a real $PAA - SiO_2$ template filled with Fe-Pd; (c) SEM image of extracted Fe-Pd nanohelices.

roughness. Under this condition, the locally damaged template is detected. Optical photo of template etched for 5 min shows that in some local areas, the template is peeled off from the substrate. A lower RF power of 100 W (lower row in Fig.3.19) shows that the barrier layer removal completes in 5 min. No damage is detected even if the template is etched for 20 min. In conclusion, the barrier layer removal can be carried out by sputter etching at a pressure of 75 mTorr, an RF power of 100 W, and an Ar flow of 25 sccm for 5 min.

3.2.5 Electrochemical Deposition

Electrodeposition was conducted in a three-electrode configuration with Metrohm Autolab PGSTAT 302N using the NOVA 1.10.1.9 software. Pt foil was used as the counter electrode (CE) and $Ag/AgCl(3MKCl)$ double junction electrode (Metrohm) was used as the reference electrode (RE). All potential values stated in this thesis are with reference to the $Ag/AgCl(3MKCl)$ electrode unless otherwise stated. The reference electrode was placed close to the surface of working electrode. The working electrode and counter electrode were placed vertically in the deposition beaker with the template surface of the working electrode

facing the counter electrode.The distance between the working electrode and counter electrode was kept at 2 cm in a beaker with 50 ml plating bath. The plating bath was deaerated by Ar gas flow for 15 min before each electrodeposition. All experiments were performed at room temperature with agitation at 300 rpm by a $Teflon^{TM}$ coated magnetic stirrer bar. Fig.3.20 shows the geometry of the electroplating cell and the configuration of the working electrode. Fig.3.20 (b) shows a typical working electrode after electrodeposition, where the nanopores of template were filled with *Fe-Pd*, showing a black color for an as-deposited sample. Fig.3.20 (c) shows the *Fe-Pd* nanohelices synthesized by this processing route after removing the PAA and SiO_2 template by $NaOH$.

A 1 cm^2, 200 nm thick Au layer was sputtered onto glass slide denoted as a flat Au working electrode. The 1 cm^2 $PAA|Au|Ag$ epoxy|glass slide working electrode is denoted as PAA electrode. The 1cm^2 $PAA-SiO2|Au|Ag$ epoxy|glass slide fabricated by the above method is denoted as helix template.

The plating bath composition are shown in table 4.1. Take Electrolyte2 as an example, 0.18 g $PdCl_2$ was fully dissolved in 1 ml 35 % HCl solution. Then the above transparent brown solution was mixed with concentrated ammonia to get a clear solution with pH within the range between 5 to 8. Then the above solution was mixed with 4.20 g $Fe_2(SO_4)_3$, 6.67 g $C_7H_6O_6S.2H_2O$ and 3.96 g $(NH_4)_2SO_4$. The final pH was adjusted to 5 by sulfuric acid and ammonia.

3.2.6 Annealing of Fe-Pd Nanowires

The annealing of *Fe-Pd* was conducted using tube furnace (Barnstead Thermolyne 21100 Tube). The *Fe-Pd* sample placed on top of a piece of quartz plate was inserted into a large quartz tube. The atmosphere was Ar balanced with $5\%H_2$ at a constant flow rate of 3 l/min. The temperature of the sample was measured by a K type thermocouple whose tip was placed right above but not touching the surface of the sample. Once the annealing was done, the tube furnace was slid away from the quartz tube and a fan was placed facing the sample spot for fast cooling. $Ar/5\%H_2$ gas flow was kept on through the whole process

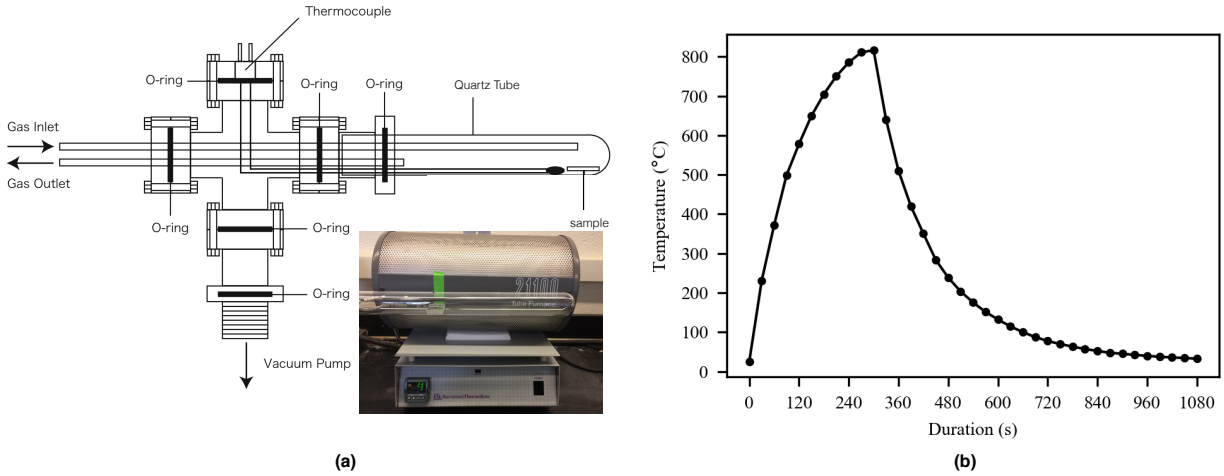

Figure 3.21: (a) Schematic illustration of the annealing setup. Inset photo shows the real experiment setup (b) A typical annealing history at maximum temperature of 800 °C for 1 min followed by compressed gas cooling showing an initial cooling rate of 5.7 K/s.

until the temperature drop down to room temperature. Fig.3.21(a) shows the annealing setup. The small tube furnace was manually slid onto and off the quartz tube. Fig.3.21(b) shows a typical annealing history of Fe-Pd nanohelices annealed at a maximum temperature of 800 °C for 1 min. Compared to bulk Fe-Pd samples, lower annealing temperature and shorter annealing duration is sufficient to get homogeneous crystal structure of nano Fe-Pd samples(as discussed in chapter 5).

Chapter 4

STOICHIOMETRY CONTROL OF AS-DEPOSITED FE-PD THIN FILMS AND NANOHELICES

4.1 Introduction

Fe-Pd binary alloy systems have attracted extensive research attention because of their unique properties originates from their chemical composition. It shows the hydrogen absorption characteristics for Pd-rich alloys [94], high magnetic anisotropy at $L1_0$ ordered $Fe_{50}Pd_{50}$ and most interestingly shape memory effect [95, 96], superelasticity and Invar effect at $Fe_{70}Pd_{30}$ [17, 97, 98, 99]. Fe-Pd with various chemical composition can be fabricated with different techniques like physical vapor deposition [100, 101, 102], melt spinning [103, 104], art melting [105, 106] and electrochemical deposition [79, 80, 81, 82, 83]. Among the above methods, electrodeposition is the most cost-effective and efficient method to deposit different structures with tunable chemical composition with a high technical potential. The main challenge of depositing Fe-Pd binary alloy with large standard reduction potential is to develop a stable plating bath by complexing Fe and Pd ions to bring their reduction potential closer. The two most widely used plating baths are an ammoniacal bath with sulfosalicylic acid as the complexing agent for Fe developed by Juzikis [77] and ammoniacal bath with citric acid as complexing agent for Fe developed by Baumgaertner [78]. Doi *et al.* [79] developed a novel bath by complexing the Fe with ammonium tartrate. With the above plating bath, by changing the parent ion ratio of Fe/Pd in the plating bath and the deposition parameters, Fe-Pd binary with various compositions can be generated. And by varying the types of working electrode, Fe-Pd with different shapes including thin film [107, 79, 108, 109] with flat working electrode, nanorods/nanotubes with porous anodic alumina (PAA) [81, 82, 83, 84] and polycarbonate membrane [85].

In the current study, *Fe-Pd* thin film generated from a flat gold working electrode and *Fe-Pd* nanohelices generated from a PAA-silica hybrid working electrode with the controllable composition are obtained by using a sulfosalicylic based ammoniacal plating bath with potentiostatic-galvanostatic mix pulse deposition technique.

4.2 Experimental Procedure

The plating bath used in this study is described in table 4.1. Iron(III) sulfate hydrate$Fe_2(SO_4)_3$ (Sigma Aldrich, 97%) and Palladium(II) chloride $PdCl_2$ (Sigma Aldrich, 99.999 %) were used as the metal source. 5-sulfosalicylic acid $C_7H_6O_6S.2H_2O$ (denoted as 5-ssa in the following session)(Sigma Aldrich, $\geq$ 99 %) and ammonia (EMD, 28$\sim$30 %) were used as the complexing agent for Fe and Pd respectively. Ammonium sulfate $(NH_4)_2SO_4$ (Sigma Aldrich,$\geq$ 99.0 %) was used as supporting electrolyte to enhance the conductivity. The final pH of the plating bath is adjusted by Sulfuric acid H_2SO_4 and ammonia. 200 nm thick Au was sputtered onto a glass slide as electrode for the synthesis of *Fe-Pd* thin film. $PAA-SiO_2$ hybrid template (detailed synthesis steps are described in chapter 3) was used for fabrication of *Fe-Pd* nanohelices. The cyclic voltammetry measurement and electrodeposition were carried out using Metrohm Autolab PGSTAT 302N equipped with NOVA 1.10.1.9 software. All experiments were performed in a deaerated three-electrode system with Pt foil as the counter electrode and Ag/AgCl (3 M KCl) double junction electrode as the reference electrode. The electrodeposition was carried out at a constant stirring rate of 300 rpm.

The spatial chemical composition of the template was measured by energy dispersive X-ray analysis (EDX). The deposited *Fe-Pd* thin film or *Fe-Pd* helices were sitting in the SEM (FEI-Sirion XL30) chamber equipped with Oxford EDX detector for imaging and measurement of spatial chemical composition over the template. The measurements were taken at a 36500 magnification, acceleration voltage 30 KV, spot size 4, process time 4 and working distance at 5 mm. The dead time was between 25% to 50 % for all the measurements. The quantitative analysis was performed with Aztec software with standardless ZAF correction. The bright field imaging, scanning mode imaging and chemical composition variance along a

	Electrolyte 1	Electrolyte 2	Electrolyte 3	Electrolyte 4	Electrolyte 5
$Fe_2(SO_4)_3$	0.1000	0.1005	0	0.1050	0.0937
$PdCl_2$	0.0200	0.0100	0.0100	0	0.0125
$C_7H_6O_6S \cdot 2H_2O$	0.2500	0.2625	0	0.2625	0
$(NH_4)_2C_4H_4O_6$	0	0	0	0	0.3750
$C_6H_8O_7 \cdot H_2O$	0	0	0	0	0.0625
$(NH_4)_2SO_4$	0.3000	0.3000	0.3000	0.3000	0
$(NH_4)Cl$	0	0	0	0	0.6000
$NH_3 \cdot H_2O$	moderate	moderate	moderate	moderate	moderate
pH	5	5	5	5	8

Table 4.1: Chemical concentration of plating bath (in unit mol/L)

Fe-Pd nanohelix wire were performed in TEM (FEI-Tecnai G2 F20) equipped with Oxford EDX detector.

4.3 Results and Discussion

4.3.1 Spatial Composition

Potentiostatic pulse deposition technique was applied for *Fe-Pd* deposition. One complete pulse cycle is composed of a deposition step in which a cathodic potential E_1 is applied for t_1 seconds and a successive resting step in which a cathodic potential E_2 is applied for t_2 seconds. For all potentiostatic pulse deposition experiments, E_2 was set to be -0.066 V. To determine the range for E_1, cyclic voltammetry (CV) was recorded on flat Au and PAA template, as is shown in Fig.4.1.

In Fig.4.1, the CV from Electrolyte 1 on flat Au shows a reduction peak at -0.7 V which can be related to the reduction of iron and palladium ions to solid state. At around -1.2 V, there shows a dramatic increase of current which can be attributed to the hydrogen evolution. For CV analysis conducted on 60 nm PAA template, reduction and oxidization peaks are found at similar potential (The collected signal is current instead of the current density since

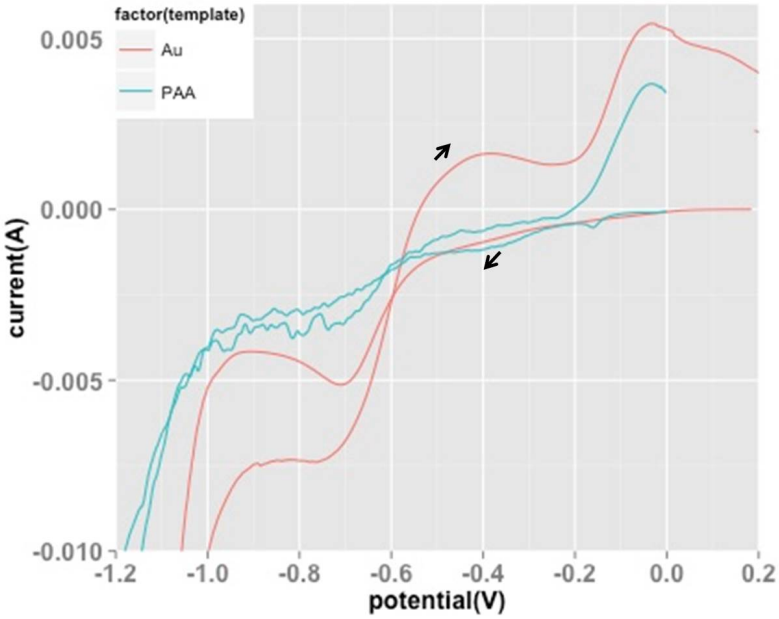

Figure 4.1: Cyclic voltammetry for deposition of Fe-Pd from Electrolyte 1 on flat Au electrode (red) and 60 nm (pore diameter) PAA (green), scan rate is 10 mV/s.

the effective electrode area is hard to measure for PAA template due to the partial wetting by electrolyte). Thus a cathodic potential that is more negative than -0.7 V is assigned to the Fe-Pd thin film and nanowire deposition.

Fig.4.2 shows a typical Fe-Pd filled template. The length of the Fe-Pd nanowire varies in the same template, and the average value is determined by the cathodic potential and deposition duration. The spatial composition of electrodeposited Fe-Pd nanohelices was measured from the top surface by SEM-EDX while the nanowires were still confined within $PAA - SiO_2|Au|Ag$ epoxy|glass slide laminated structure. For each sample, EDX quantified result was generated at 10 to 13 random spots across the surface of the template. As the penetration depth of the EDX beam is on the micron scale, the data collected is an average composition of different Fe-Pd nanowires over a micrometer scale area. Contamination cannot be defined because Al_2O_3, SiO_2, Au,Ag (and possibly Cl^-, Na^+, NH^{4+}, K^+ in silver

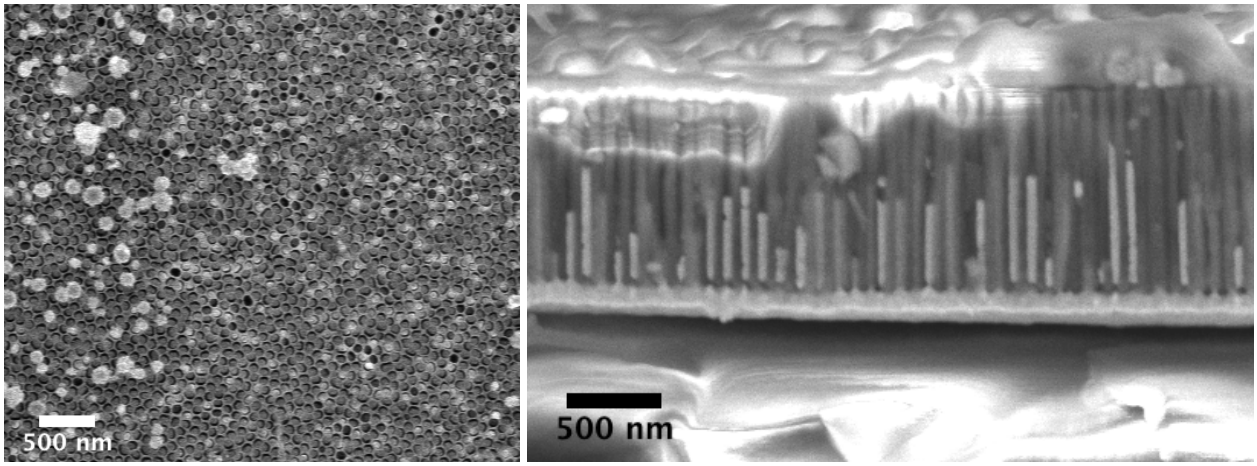

Figure 4.2: (a) SEM top view of PAA-SiO_2 template filled with Fe-Pd after etching in 0.1 M $NaOH$ for 2 min. (b) SEM cross section view of $PAA-SiO_2$ template filled with Fe-Pd nanohelices shown in the lighter cylinder region in the image.

epoxy) coexist in the sample.

Fig.4.3 shows the dependence of stoichiometry of as-deposited Fe-Pd alloy on applied cathodic potential E_1. For the deposition of Fe-Pd thin film on flat Au electrode shown in red, a trend of increasing amount of Fe component in the alloy is shown when a higher overpotential is applied. Such behavior indicates that the deposition of Fe-Pd system is anomalous co-deposition (ACD) in which the less noble metal (Fe here) is preferably deposited under most plating conditions. When the applied E_1 decreases from -0.86 V to -0.96 V, the atomic percentage of Fe in the deposited alloy experiences a significant increase from 32 at.% to 62 at.%. With further increase of overpotential, the Fe atomic percentage gradually reached 70 at.% at -1.16 V and plateaus until -1.30 V. At even more negative potential -1.36 V and -1.40 V, the spatial variance of deposited Fe-Pd film becomes much larger and the median of Fe percentage decreases to 65 at.%.

Such Fe composition change at different overpotentials can be explained based on the CV analysis of single metal plating bath. Fig.4.4 indicates that by complexing the Pd^{2+} with ammonia and Fe^{3+} with 5-sulfosalicylic acid, there exists an overlap of reduction potential

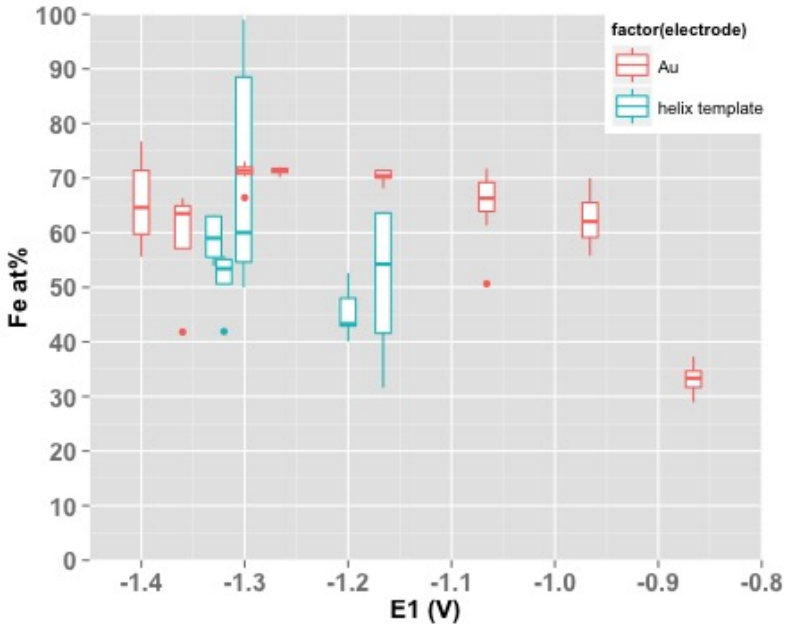

Figure 4.3: Influence of cathodic potential E_1 on Fe concentration in Fe-Pd alloy deposited from Electrolyte 1 in Fe-Pd thin film deposited on flat Au electrode (red) and Fe-Pd nano helix deposited inside a PAA-SiO_2 hybrid template (green).

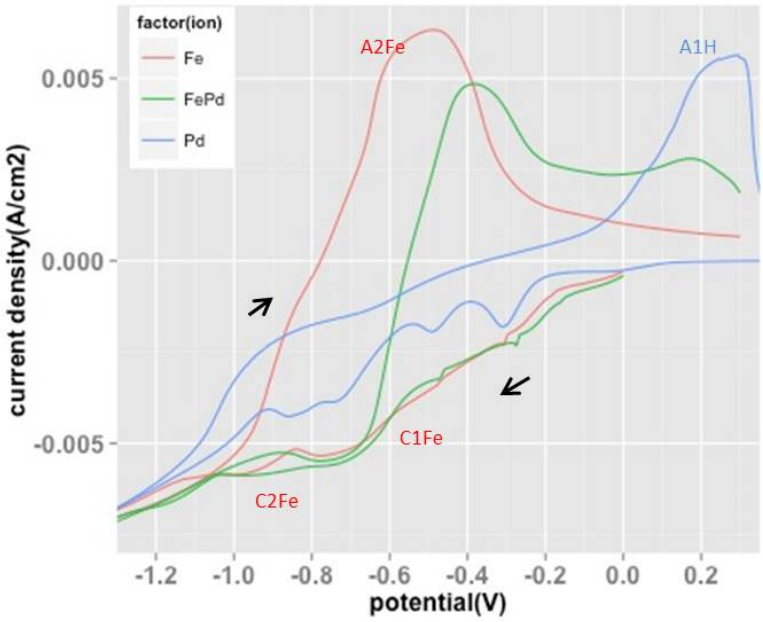

r

Figure 4.4: Cyclic voltammetry for Electrolyte 2 (green), Electrolyte 3 (blue) and Electrolyte 4 (red) on flat Au electrode, scan rate is 50 mV/s.

region for Fe and Pd. The small difference of reduction potential for both ions permits the co-deposition of Fe-Pd alloy. In the CV of Electrolyte 4 (Fig. Fig.4.4 red), there are two reduction peaks at -0.77 V and -1.00 V. These might be related to the reactions of Fe^{3+}-5-ssa to Fe^{2+}-5-ssa and Fe^{2+}-5-ssa to Fe^{0}. When a low overpotential E_1 is applied, Fe might be deposited through the underpotential co-deposition which is common for iron deposition on a noble metal [110, 111]. At more negative cathodic potential -0.97 V, the bulk Fe deposit starts and causes the sudden increase of the fraction of Fe in the deposited alloy. The Fe percentage in the alloy then keeps increasing with increasing overpotential and finally levels off suggesting that the deposition of Fe goes through an activation controlled region, an activation and mass transport mixed controlled region to the mass transport controlled region. A larger spatial composition variance of the sample shows up at around -1.40 V owing to the disturbance of rapid hydrogen evolution. The chemical composition of as-deposited Fe-Pd thin film on the flat Au electrode suggests that E_1 values ranging between -1.1 V and -1.3 V are desired to get the target 70 at.% Fe in a thin film.

Spatial composition data for Fe-Pd nano-spring with E_1 ranging from -1.16 V to -1.33 V are presented as blue box in Fig.4.3. Fe-Pd helix has lower Fe fraction than Fe-Pd thin film deposited at the same condition. The variance of Fe-Pd helix spatial composition is much larger compared to the Fe-Pd thin film samples. Further study of the kinetic behaviors for Fe-Pd deposition into 10 nm nano-helical electrode assembly is necessary to explain such difference caused by the change in scale. The desired $Fe_{70}Pd_{30}$ sample was not obtained by potentiostatic pulse deposition from Electrolyte 1.

In order to reach 70 at.% Fe for helix template at a relatively low overpotential, the concentration of Pd^{2+} in the plating bath was reduced to 0.01 M. Then potentiostatic pulse deposition for Fe-Pd thin film was conducted on flat Au to get optimized E_1 values corresponding to $Fe_{70}Pd_{30}$ for Electrolyte 2. Fig.4.5 red box plots show that with increasing overpotential the Fe fraction increases from 25 at.% -0.87 V to 77 at.% -1.07 V. Further increase of overpotential caused a drop of Fe fraction and also a large spatial composition variance.

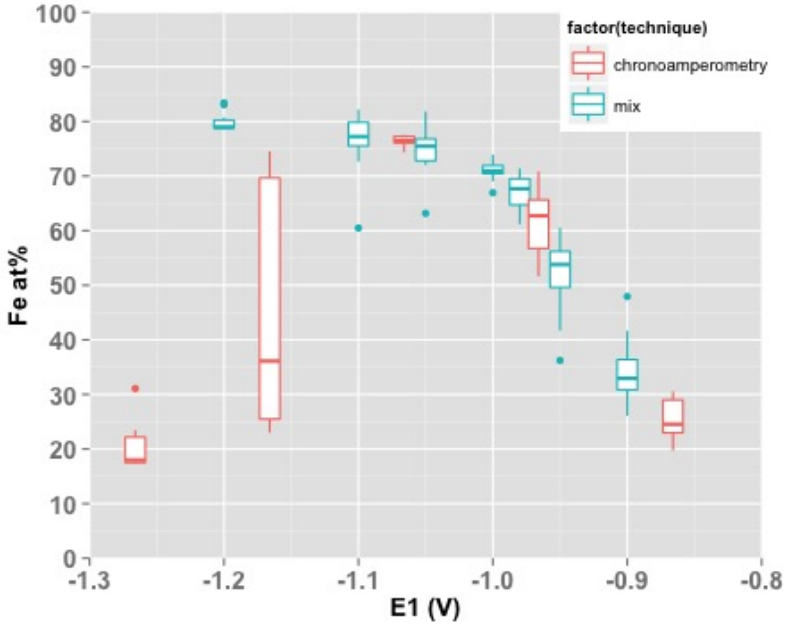

Figure 4.5: Influence of cathodic potential E_1 on Fe concentration in Fe-Pd alloy deposited from Electrolyte 2 in Fe-Pd thin films deposited on a flat Au electrode with potentiostatic pulse technique (chronoamperometry technique in red) and mixed technique (mix technique in green).

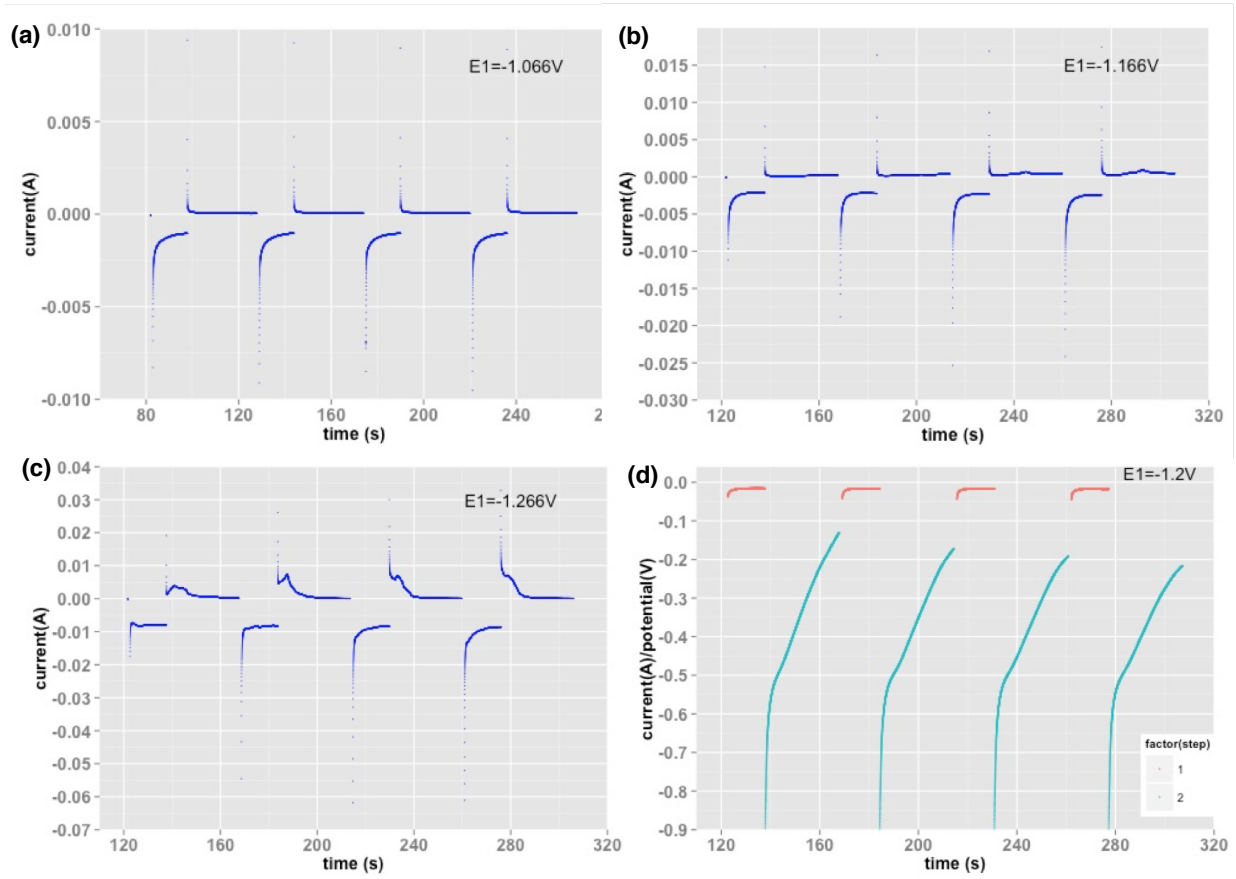

Figure 4.6: Current transient I-t (first four cycles) of Fe-Pd deposition from Electrolyte 2 at E_2=-0.066 V, t_1=15 s, t_2=30 s,(a) with applied E_1=-1.066 V, (b) E_1=-1.166 V (c) E_1=-1.266 V,. and (d) the I-t, P-t of Fe-Pd deposited from Electrolyte 2 with E_1=-1.200 V, I_2=0 A, t_1=15 s,t_2=30 s.

The observations on the current transient I-t curve with potentiostatic pulse technique suggest that such compositional variance results not merely from the hydrogen evolution at higher overpotential region, but also from the possible dissolution that happens at the resting step with applied E_2=-0.066 V. According to Haehnel [82], the resting step allows the cation concentration to recover after the depletion at the deposition step. Ideally, at the resting step, neither deposition nor dissolution of already deposited metal should happen. Fig.4.6(a) shows an ideal current transient curve from Electrolyte 2. When cathodic potential changes there is a surge of current caused by the charging of electric double layer. Then the current gradually decreases until it reaches a diffusion-controlled region and levels off. For the Fe-Pd film deposited at E_1=-1.166 V, the current at the resting step stabilizes at around 0 A, indicating no redox reaction present at the working electrode. At E_1=-1.166 V, it starts to show anodic current after two cycles of deposition. The increase in the anodic current is more visible in the current transient for Fe-Pd film deposited at E_1=-1.266 V. Considering the drastic decrease of Fe fraction in the deposited film (Fig.4.5 red) at -1.166 V and -1.266 V, it is rational to conclude that the dissolution of deposited Fe takes place during the resting step at larger overpotential. The CV of Electrolyte 2 on the Au electrode (Fig.4.4 green) shows a strong oxidation peak at -0.4 V, which can be linked to $Fe^0 -> Fe^{2+}$-5-ssa. After the first monolayer of Fe-Pd is deposited on the Au electrode, the solid electrode becomes Fe-Pd alloy on which the deposition of Fe and Pd might have a different oxidization/reduction potential. The electrode surface composition change and solution ion concentration change after the deposition step at higher overpotential might be responsible for the shift of equilibrium potential of $Fe^0 -> Fe^{2+}$-5-ssa, thus causing a higher anodic current at the resting step.

To eliminate the disturbance of Fe dissolution at resting step, potentiostatic-galvanostatic mix pulse deposition technique is proposed. A static potential of E_1 is applied at the deposition step, and a constant zero current is applied at resting step. By mixing the chronoamperometry and chronopotentiometry techniques, any redox reaction happening at the resting half cycle can be avoided. Fig.4.6(d) shows the current transient of deposition step and potential transient at the resting step with potentiostatic-galvanostatic mix technique. The

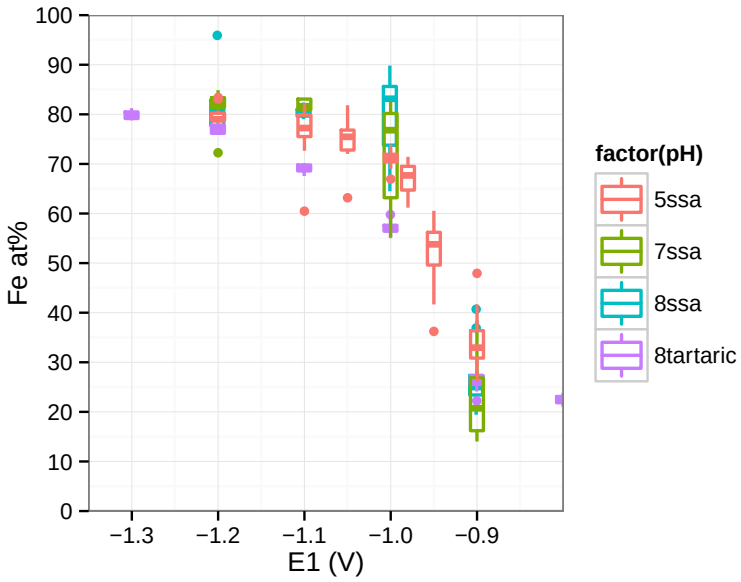

Figure 4.7: Influence of cathodic potential E_1 on the Fe composition in Fe-Pd thin films deposited from different plating bath on the flat Au electrode with mixed technique.

current curve at the deposition half cycle follows the same as with the potentiostatic pulse technique. And the potential in Fig.4.6(d) shows that the equilibrium potential shifts to more negative value as the deposition goes on for several cycles.

The effect of the applied cathodic potential E_1 in the deposition step on the Fe-Pd thin film composition with the potentiostatic-galvanostatic mix technique is indicated as the green boxplot in Fig.4.5. Fe fraction again experiences a rapid increase from -0.9 V to 1.0 V, reaches the target composition of Fe 70 at.% at -1.0 V, then saturates at Fe 80 at.% at higher overpotential. Compared with Fe-Pd films deposited with the pulse chronoamperometry method, Fe-Pd films deposited with the mix deposition technique shows a more stable composition with much lower variance at larger overpotential region. This proves that the mixed deposition method is more suitable for the composition control of Fe-Pd alloy.

The effect of pH value of sulfosalicylic acid-based plating bath and tartaric acid-based plating bath on the spatial composition variation of deposited Fe-Pd alloy is also investi-

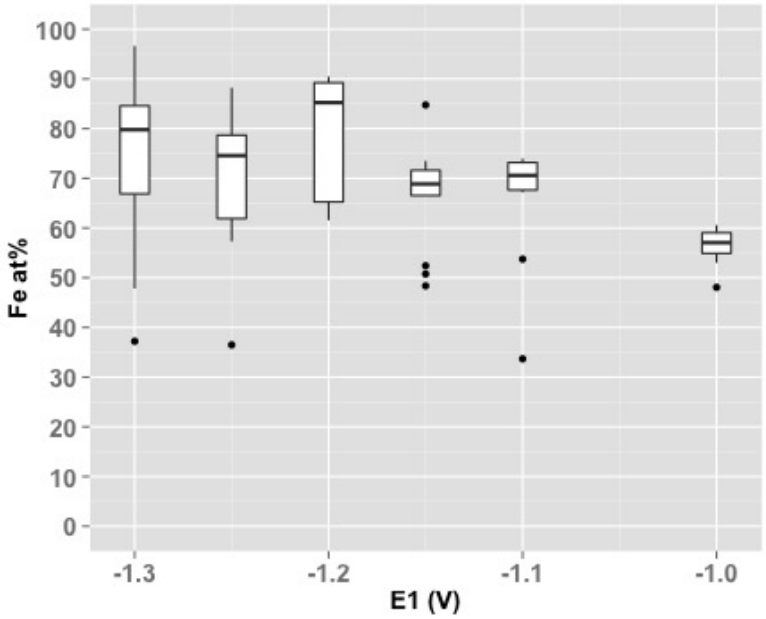

Figure 4.8: Influence of cathodic potential E_1 on Fe composition in Fe-Pd nanohelix from Electrolyte 2 with the mixed technique.

gated. Fig.4.7 shows the spatial composition of the Fe-Pd thin film deposited from different plating bath with the mixed deposition technique. For sulfosalicylic plating bath, the median of the deposited alloy composition does not vary much for different pH values 5, 7 and 8. The variance of the composition does not vary much at Fe and Pd diffusion region. While at the Fe activation region, pH=5 plating bath gives the lowest variance. For tartaric acid plating bath, the variance of the composition is low for all regions. Thus sulfosalicylic acid of pH=5 or tartaric acid based plating bath are both suitable for $Fe_{70}Pd_{30}$ deposition.

Fig.4.8 indicates the spatial composition of Fe-Pd nano-helix deposited from Electrolyte 2 with mix deposition technique. The median of Fe atomic percentage increases from 56% to 85% when E_1 decreases from -1.00 V to -1.20 V. The desired composition of $Fe_{70}Pd_{30}$ nanohelix is obtained in the range from E_1=-1.10 V to -1.15 V. At a higher overpotential than -1.2 V, the median of Fe fraction fluctuates around 85% with a much larger variance

Fe-Pd	Electrolyte	E_1(V)	t_1(s)	I_2 (A)	t_2 (s)
Thin film	Electrolyte 2	-1.0	15	0	30
	Electrolyte 5	-1.1	15	0	30
Nanorods	Electrolyte 5	-1.1	15	0	30
Nanohelices	Electrolyte 2	-1.10 to -1.15	15	0	30

Table 4.2: Summary for synthesis conditions to get $Fe_{70}Pd_{30}$.

than low overpotential, which might be caused by the disturbance of hydrogen evolution at higher overpotential (typically around the standard potential of -1.23 V) for electrolysis of water .

The optimized electrodeposition condition to get 70 at.% Fe for thin film, nanorods(detailed explanation can be found in chapter 5), and nanohelices is presented in Table 4.2.

4.3.2 Composition along the Axis of Fe-Pd Nanohelices

Some researchers also reported a composition gradient along the length of electrodeposited *Fe-Pd* nanotube [112]. Pulse deposition with a shorter time in each step seems to both enhance the continuous filling of nano-pore and also to generate a more homogeneous chemical composition of *Fe-Pd* alloy [83, 113]. The effect of pulse deposition duration on composition over 350 nm to 500 nm length of *Fe-Pd* single nano-wire was investigated. Fig.4.9 shows the TEM image of the freestanding *Fe-Pd* helix released from the PAA-SiO_2 template with the EDX line profile scanning data (orange line in the image shows the sampling position). For potentiostatic pulse deposited sample from Electrolyte 1 with 60 s t_1 and 120 s t_2 (Fig.4.9(a)), there is an obvious variance of the composition at different positions of *Fe-Pd* helical wire. The variance of the composition comes from several reasons including the electrode surface change, the disturbance from hydrogen evolution, the depletion of ions and also the dissolution of already deposited *Fe*, which is discussed in the previous section. When a much

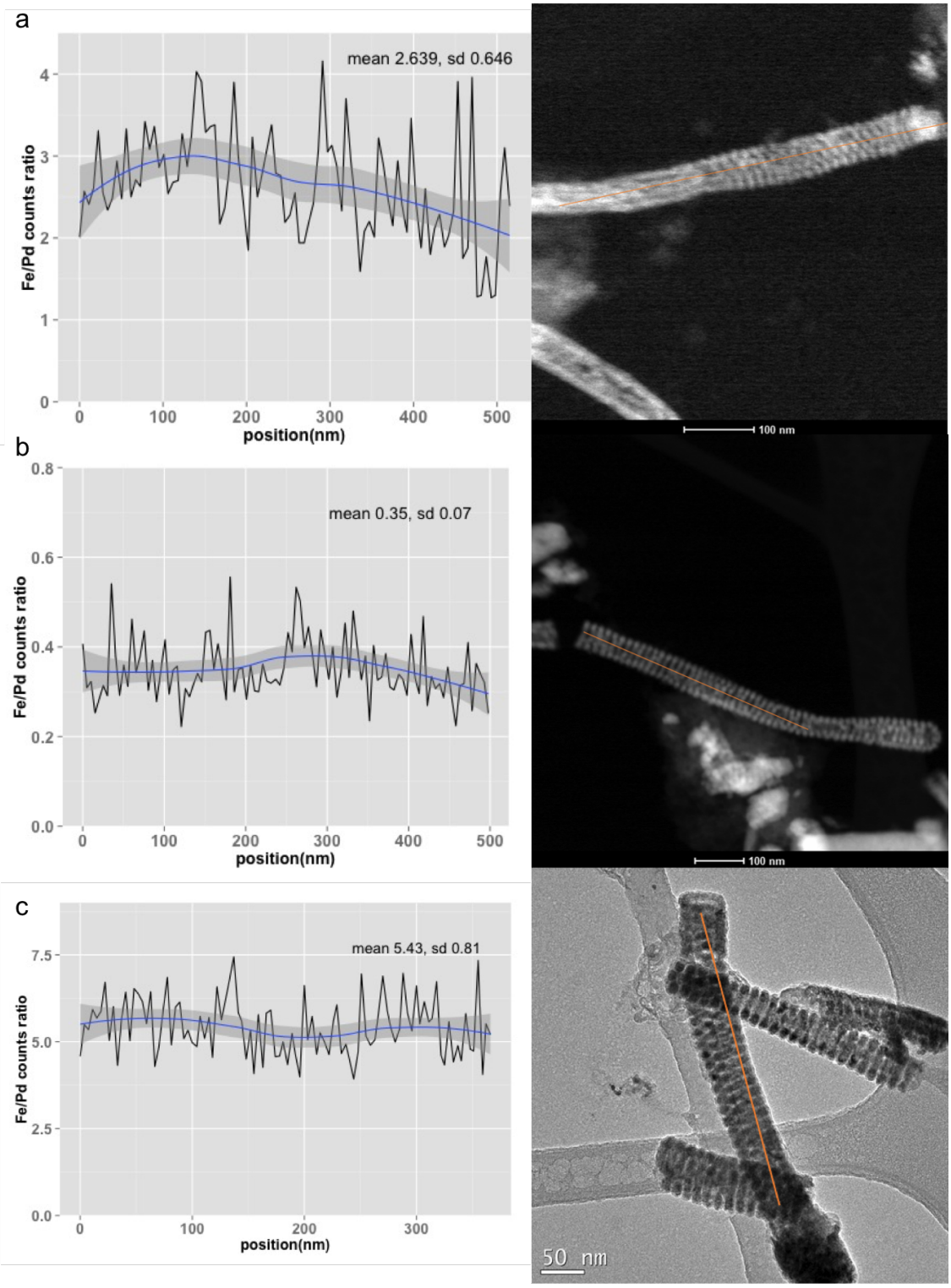

Figure 4.9: TEM image of a Fe-Pd nanohelix and corresponding EDX Fe/Pd counts ratio along the length of nano-wire deposited (a) from Electrolyte 1 with potentiostatic pulse technique at E_1=-1.166 V, t_1=60 s, E_2=-0.066 V, t_2=120 s (b) from Electrolyte 1 with potentiostatic pulse technique E_1=-1.166 V, t_1=0.03 s, E_2=-0.066 V, t_2=1 s (c) from Electrolyte 2 with mix technique E_1=-1.100 V, t_1=15 s, I_2=0 A, t_2=30 s.

shorter deposition time (0.03 s) and resting time (1 s) is applied (Fig.4.9(b)), the variance of Fe fraction along the length is less visible. However, quantitative EDX analysis based on spot data shows a dramatic drop of Fe at.% to 10 at.% for helical wire deposited at t_1=0.03 s compared with Fe at.% of 57 at.% for sample deposited at t_1=60 s.

By analogy with the deposition of $Fe-Ni$ alloy system [114], the increase of Pd fraction at a shorter deposition time might result from the preferred deposition of the more noble component at the initial stage of deposition. However, Fe-Pd thin film deposited from similar plating bath at slightly alkaline state with galvanostatic pulse technique shows only a slight Fe fraction drop when the pulse duration decrease from 1 s to 0.001 s [77]. Thus the Fe fraction drop in this study is mainly caused by the Fe dissolution at the prolonged resting step (1 s/0.03 s>120 s/60 s).

Fe-Pd nano-helixes deposited from Electrolyte 2 with potentiostatic-galvanostatic mix technique (t_1=15 s and t_2=30 s) are shown in Fig.4.9(c). The EDX line scanning profile shows a more homogeneous composition along the wire length. Quantitative analysis shows that the Fe atomic percentage is 72.3 at.% for this sample. In conclusion, with the new deposition technique, the composition variance of single Fe-Pd nano-spring is decreased while maintaining the high fraction of Fe in the deposited alloy.

4.4 Conclusion

Fe-Pd thin films and Fe-Pd helices were electrodeposited from sulfosalicylic acid based ammoniacal plating bath and the effects of plating bath composition, plating techniques on the spatial and individual wire chemical composition were investigated. $Fe_{70}Pd_{30}$ thin films with homogeneous spatial composition was fabricated by potentiostatic-galvanostatic mix pulse deposition technique from Electrolyte 2 at $E_1 = -1.0V, t_1 = 15s, I_2 = 0A, t_2 = 30s$ and from Electrolyte 5 at $E_1 = -1.1V, t_1 = 15s, I_2 = 0A, t_2 = 30s$. $Fe_{70}Pd_{30}$ helices with homogeneous spatial and single wire composition was fabricated from Elecgtrolyte 2 at $E_1 = -1.10$ to $-1.15V, t_1 = 15s, I_2 = 0A, t_2 = 30s$.

Chapter 5

STRUCTURE OF ANNEALED $FE_{70}PD_{30}$ NANORODS AND NANOHELICES SYNTHESIZED BY ELECTRODEPOSITION

Fe-Pd binary alloy exhibit versatile physical properties at different stoichiometries. At equiatomic $Fe_{50}Pd_{50}$ with ordered tetragonal $L1_0$ crystal structure exhibits strong uniaxial magnetocrystalline anisotropy along the easy 'c' axis, leading to a promising application as future high density magnetic recording media [95, 115]. At the stoichiometry around 70 at.% Fe, this binary alloy shows the reversible face-centered cubic (fcc) austenite to face-centered tetragonal (fct) martensite phase transformation. This martensite phase transformation induced by temperature, stress or/and magnetic field leads to the shape memory effect and superelasticity [36, 99].Compared to the conventional shape memory alloy (SMA), austenite-martensite phase transition and martensite variants reorientation can be triggered by magnetic fields along with temperature and stress. Among all FSMA, $Fe_{70}Pd_{30}$ system and Ni_2MnGa are the only two materials known to show large (> 0.006) magnetic field induced strain [36]. Furthermore, $Fe_{70}Pd_{30}$ shows several advantages for practical applications including its high magnetocrystalline anisotropy, high ductility compared to Ni_2MnGa. Moreover, the good biocompatibility of $Fe_{70}Pd_{30}$ allows the application of biomedical and clinical use [18, 40].Therefore, the advanced mechanical properties of $Fe_{70}Pd_{30}$ FSMA make it a promising sensing and actuating material.

The bulk SMA materials have attracted considerable attention as medical devices, couplings and fasteners, micro-actuators, adaptive materials and hybrid composites, and damping materials [33].With the recent trend that requires the creation of nano-devices, it is essential to fabricate and characterize the SMA in nanometer scale. Moreover, FSMA nanowires as sensors and actuators are expected to exhibit larger actuation frequency since the response

speed is not limited by the heat conduction.

The intent of this study is to investigate the martensite phase transformation behavior of $Fe_{70}Pd_{30}$ nanorods. First, We fabricated Fe-Pd nanorods by AAO template-assisted electrodeposition. The stoichiometry homogeneity of nanorods clusters and individual nanorod along the axis is characterized by SEM-EDX and STEM-EDX separately. The crystal structure of as-deposited and $Fe_{70}Pd_{30}$ nanorods are discussed based on the X-ray diffraction (XRD) spectrum. The martensite phase transformation of $Fe_{70}Pd_{30}$ is based on XRD and magnetic measurements.

5.1 Experimental Procedure

Detailed fabrication steps for PAA template and the electrodeposition schemes can be found in chapter and chapter 3 and chapter 4. The summary of the synthesis steps is presented as follows. The PAA membrane is synthesized by the well-known two-step anodization process developed by Masuda [92]. 0.13 mm-thick high purity (99.9995 %) aluminum foil is anodized at 40 V d.c. at 5 °C in 0.3 M oxalic acid aqueous solution. The pore length is controlled at 3 um by adjusting the duration of second anodization step. The anodized PAA template is immersed in 5 wt.% H_3PO_4 to widening the pore to 65 nm in diameter. A 200 nm thick Au layer is sputtered onto the opening side of PAA as the conducting layer. Then the AAO with back Al is stuck to a glass slide by silver epoxy. Finally, the back aluminum layer is etched out by 1 M $CuCl_2$. And the barrier layer is removed by 5 wt.% H_3PO_4.

The electrodeposition of Fe-Pd is carried out in the plating bath of 0.0937 M $Fe_2(SO_4)_3$, 0.0125 M $PdCl_2$, 0.375 M $(NH_4)_2C_4H_4O_6$, 0.0625 M $C_6H_8O_7$, 0.3 M $NH_3.H_2O$ and 0.6 M NH_4Cl. The pH of the final electrolyte was adjusted to 8 by $NH_3.H_2O$. All electrodeposition were conducted with Pt foil as counter electrode and Ag/AgCl (3M KCl) as reference electrode at room temperature stirring at 300 rpm. A potentiostatic-galvanostatic mix technique (t_1=15s for various applied potential E_1 and t_2=30 s for resting cycle that I_2=0 A). The as-synthesized Fe-Pd nanorods were annealed in Ar/H_2 (5%) at various temperature from 600 °C to 800 °C followed by compressed air cooling.

The electrodeposition was performed by potentiostat/galvanostat (Metrohm Autolab PG-STAT302N). The *Fe-Pd* nanorods were characterized by scanning electron microscope combined with energy dispersive X-ray spectroscopy (SEM, FEI Sirion XL30 with Oxford EDX detector), transmission electron microscopy (TEM, FEI Tecnai G2 F20), X-ray diffractometer (XRD, Bruker D8 Discover with IS 2-D XRD System). The magnetic property of *Fe-Pd* nanorods were performed by vibrating sample magnetometer (VSM, Quantum Design VersaLab).

5.2 Results and Discussion

5.2.1 Chemical Stoichiometry of Electrodeposited Fe-Pd Nanorods

The PAA template with potentiostatic-galvanostatic mix technique is proved to be excellent for the uniform electrochemical growth of *Fe-Pd* nanorods. Fig. 5.1(a) shows the typical *Fe-Pd* nanorods clusters extracted from PAA template. As stated in the introduction section, properties of *Fe-Pd* alloys are high stoichiometry sensitive. Therefore first we verified the spatial chemical composition of the fabricated *Fe-Pd* nanorods clusters by SEM-EDX. Fig.5.1(b) indicates the effect of the applied cathodic potential E_1 at the deposition half cycle on the stoichiometry of *Fe-Pd* nanorods. The content of *Fe* at.% in the nanorods ranges from 27.8% to 81.2% as E_1 changes from -0.98 V to -1.2 V. The targeted 70 at.% *Fe* was achieved at around -1.1 V.With our current electrolyte and potentiostatic-galvanostatic mix technique generates spatially homogeneous stoichiometry of *Fe-Pd* binary alloy as indicated by the small standard error over the whole stoichiometry range. As the beam of SEM-EDX can penetrate the template at the micrometer scale, it characterized the averaged stoichiometry over many *Fe-Pd* nanorods clusters. Therefore STEM-EDX is necessary to characterize the chemical composition of a single *Fe-Pd* nanorod. The STEM-EDX line profile (Fig.5.2(b)) shows a very stable trend along the rod axis. Quantitative result from EDX spot spectrum (Fig.5.2(a)) indicates that the nanorod is at target composition of $Fe_{70.9}Pd_{29.1}$.

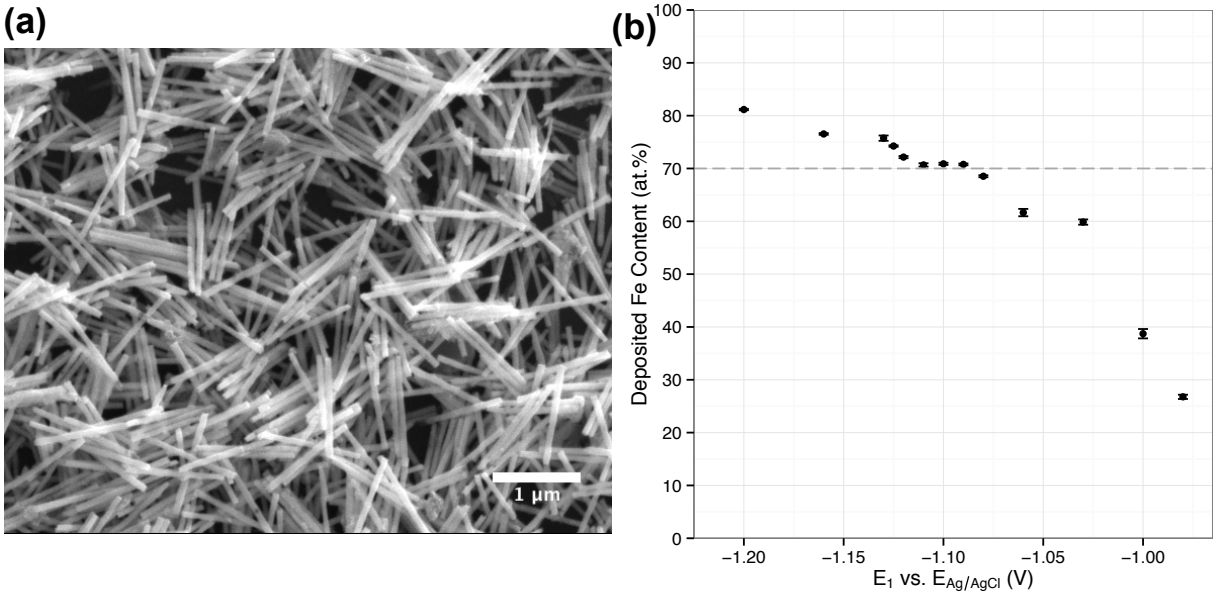

Figure 5.1: (a) SEM micrograph of as-deposited $Fe_{69.7}Pd_{30.3}$ with diameter of 65 nm and length of 1 µm extracted from AAO template (b) Dependence of Fe content in as-deposited Fe-Pd nanorods on applied potential E_1. The dashed line indicates the target stoichiometry of Fe 70 at.%. The dots and whiskers indicate mean and the standard error.

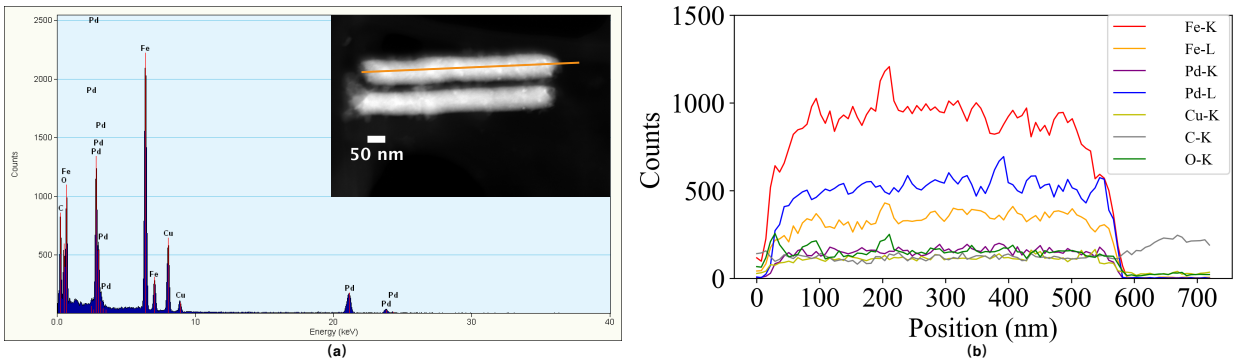

Figure 5.2: TEM investigation of as-deposited single Fe-Pd nanorod extracted from the PAA template: (a) EDX spectrum of one spot on the Fe-Pd nanorod, the quantified result gives 70.9 at.% Fe. The inset shows the STEM image of Fe-Pd nanorod. (b) STEM-EDX line profile across the length of one Fe-Pd nanorod along the orange line in (a) showing a homogeneous concentration along the rod length direction.

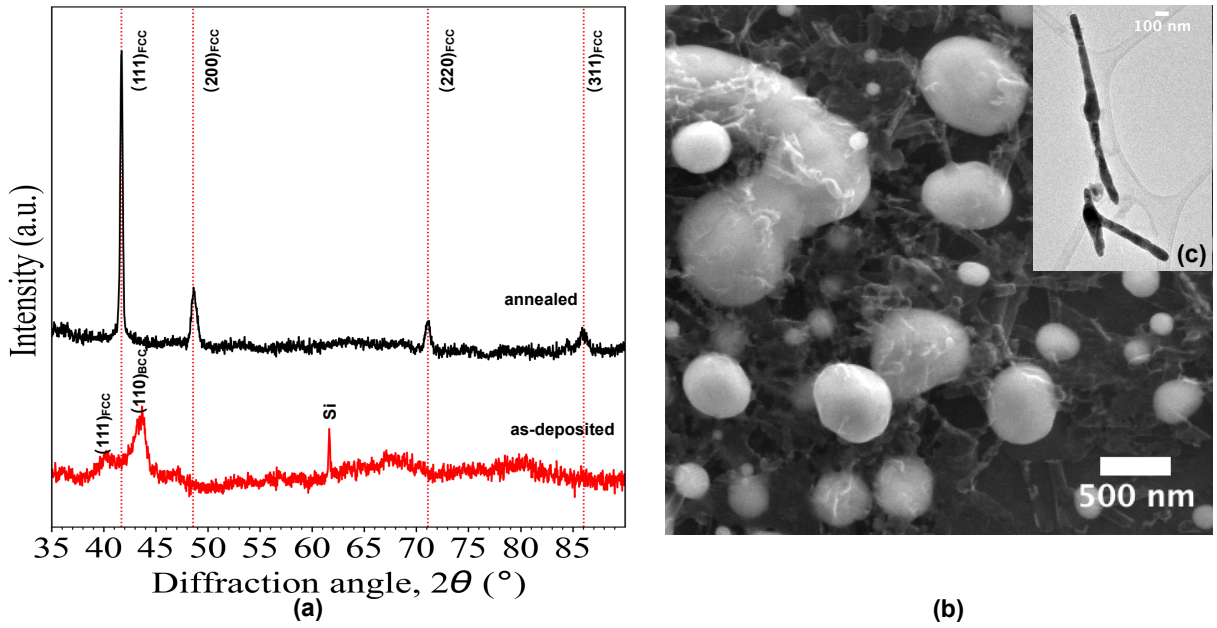

Figure 5.3: (a) XRD patterns at room temperature of as-deposited $Fe_{69.7}Pd_{30.3}$ nanorods (65 nm in diameter and 1 µm in length) extracted from PAA template and annealed at 800 °C for 30 min . The dashed line indicates the peak positions of bulk $Fe_{70.3}Pd_{29.7}$ according to Oshima [116](b) SEM image of annealed $Fe_{69.7}Pd_{30.3}$ nanorods on Si wafer (c) TEM image of annealed $Fe_{69.7}Pd_{30.3}$ nanorods without aggregation.

5.2.2 Crystal Structure of Electrodeposited Fe-Pd Nanorods

Prior to verify the phase transformation of fabricated $Fe_{70}Pd_{30}$ nanorods, we investigated the crystallography of the free-standing nanorods by XRD. A typical XRD pattern of as-deposited $Fe_{69.7}Pd_{30.3}$ shown in Fig.5.3(a) indicates that both bcc(α-Fe,Pd) solid solution (indicated by $2\theta = 43.70°$) and fcc (γ-Fe,Pd) solid solution (indicated by $2\theta = 40.26°$) coexist in the as-deposited $Fe_{69.7}Pd_{30.3}$ nanorods. The wide peaks indicates that the as-deposited Fe-Pd nano-rods are ultra-fine with very small crystallite size. And there might be a lot of defects and stress resulted from the low diffusion ability of the atoms during electrodeposition. Such result suggests that the as-deposited $Fe_{69.7}Pd_{30.3}$ nanorods by the current electrodeposition method are in equilibrium state which corresponds with the bulk

Fe-Pd binary alloy phase diagram [42]. For the reason of achieving $Fe_{70}Pd_{30}$ nanorods with shape memory and superelasticity, a single crystal phase is necessary. According to the bulk *Fe-Pd* phase diagram, $Fe_{70}Pd_{30}$ is stable as single fcc (γ-Fe, Pd) solid solution above 770 °C. Therefore, we annealed the as-synthesized nanorods at 800 °C in $Ar/5\%H_2$ followed by compressed gas cooling to get the metastable austenite fcc $Fe_{70}Pd_{30}$ nanorods at room temperature. Fig.5.3(a) illustrates the crystal structure of extracted freestanding $Fe_{69.7}Pd_{30.3}$ nanorods annealed on ⟨100⟩ Si wafer at 800 °C in $Ar/5\%H_2$ for 30 min. Four peaks belonging to disordered fcc (111) ($2\theta = 41.72°$), fcc (200) ($2\theta = 48.64°$), fcc (220) ($2\theta = 71.17°$), and fcc (311) ($2\theta = 85.94°$) are formed after annealing and quenching.This sharpening of XRD peaks after annealing indicates improved crystallinity and growth of crystallite size. The lattice constant of annealed $Fe_{69.7}Pd_{30.3}$ nanorods calculated from the XRD pattern $a = 3.75$Å is in good agreement with the literature value [116]. This indicates that *Fe-Pd* fcc austenite phase was successfully synthesized with correct stoichiometry of 70 *at.*% *Fe*.

It is necessary to point out that during thermal annealing, the agglomeration and growth of nano-wires usually occur. Fig.5.3(b) shows that after high-temperature thermal annealing, tightly packed contacting nanorods tend to grow into large spherical particles up to 700nm in diameter, While only loosely packed nano-rods during annealing still maintain the rod shape (Fig.5.3(c)). To avoid such uncontrolled growth of *Fe-Pd* nano-wires, thermal annealing is conducted while the binary alloy is embedded in the PAA template. For *Fe-Pd* nanorods, the thermal annealing is conducted for *Fe-Pd* embedded in PAA, while for *Fe-Pd* nano-helices, the annealing is conducted for *Fe-Pd* embedded in PAA-SiO_2 hybrid template. The thermal annealing of *Fe-Pd* nanorods and nanohelices embedded in PAA or PAA-SiO_2 template, however, is expected to induce residual stress in *Fe-Pd* nano-materials which influences their phase transformations [117].

5.2.3 Stoichiometry Effect for Fe-Pd Nanorods Embedded in PAA

Fig.5.4(a) shows the XRD pattern of *Fe-Pd* nanorods with different stoichiometry (measured

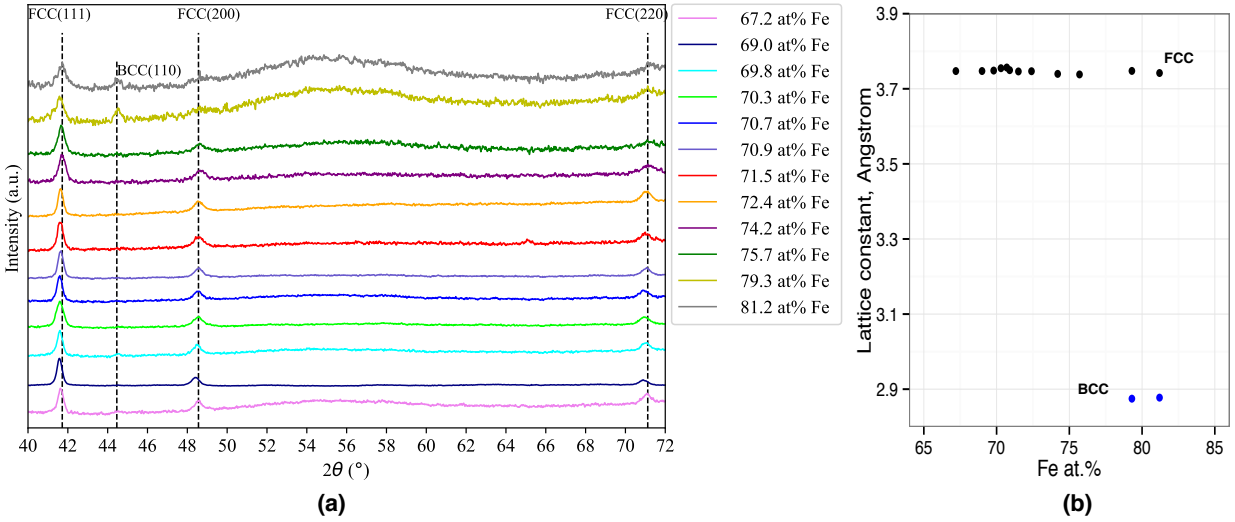

Figure 5.4: (a) XRD patterns of Fe-Pd nano-rods with various stoichiometry (from 67.2 at.% Fe to 81.2 at.% Fe) annealed inside PAA template at 800 °C for 1 min in $Ar/5\%H_2$ followed by rapid cooling (b) Variations of lattice constant of fcc phase and bcc phase with respect to the varying stoichiometry.

by EDX) annealed inside PAA template at 800°C for 1 min. Between the stoichiometry of 67.2 Fe $at.\%$ and 75.7 Fe $at.\%$, the annealed Fe-Pd nanorods show distinctive disordered fcc structure as indicated by three peaks of fcc (111), fcc (200) and fcc (220). The lattice parameter of fcc phase (shown in Fig.5.4(b)) is calculated with extrapolation method as a function of $cos^2(\theta)/sin(\theta)$. The lattice parameters are very close to 3.75 Å and show a slight trend of decreasing when the Fe content increase. When the stoichiometry reaches to 79.3 Fe $at.\%$, the small peak at $2\theta = 44.5°$ confirms the existence of bcc (α-Fe,Pd) solid solution phase, this indicates that the annealing temperature (800°C) is not high enough to dissolve the α-Fe precipitates of the as-electrodeposited Fe-Pd nanorods for Fe at.% higher than 79.3 %. The lattice constant of bcc phase is calculated based on the bcc (110) peak and is plotted in Fig.5.4(b).

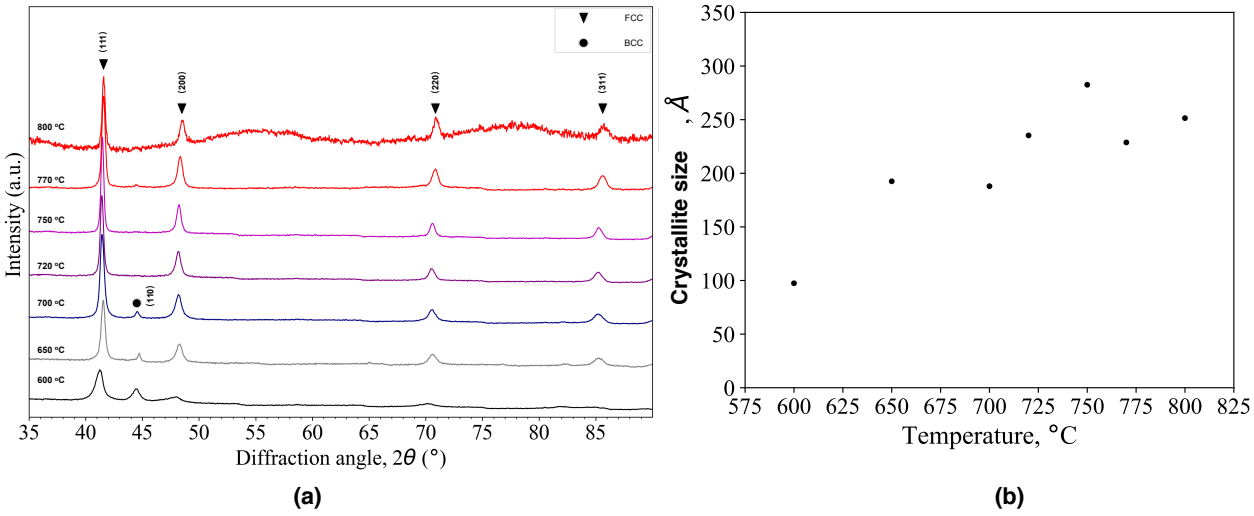

Figure 5.5: XRD patterns of $Fe_{71.3}Pd_{28.7}$ nano-rods (1) annealed at various temperatures (600 °C, 650 °C, 700 °C, 720 °C, 750 °C, 770 °C and 800 °C) for 1 min in $Ar/5\%H_2$ followed by rapid cooling (b) Crystallite size determined from XRD patterns.

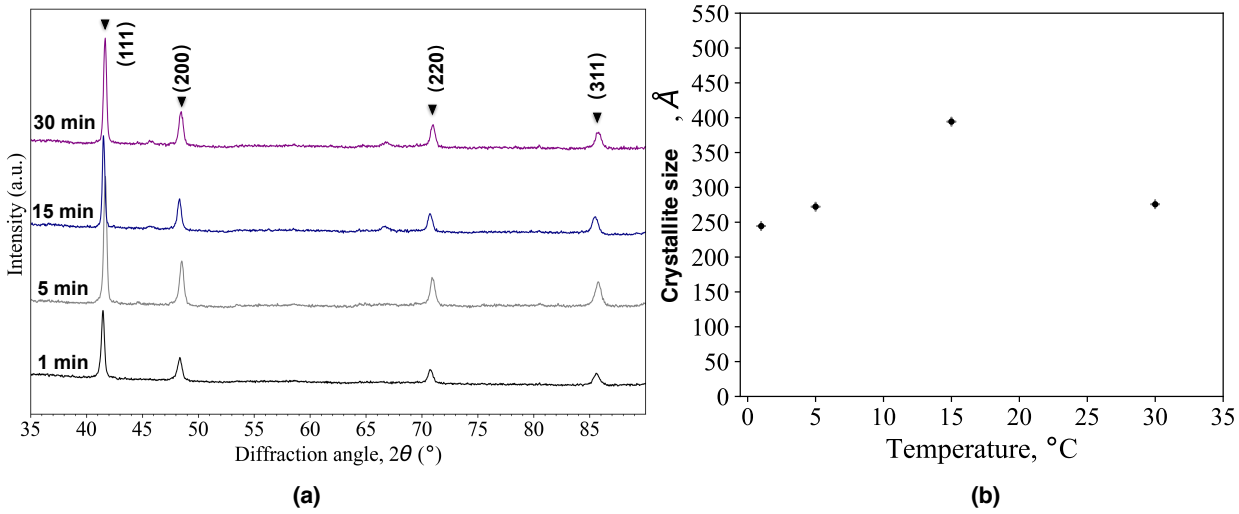

Figure 5.6: XRD patterns of $Fe_{71.3}Pd_{28.7}$ nano-rods annealed at 800°C for various duration (1 min, 5 min, 15 min and 30 min) followed by rapid cooling (b) Crystallite size determined from XRD pattern.

5.2.4 Annealing Temperature Effect for Fe-Pd Nanorods Embedded in PAA

Fig.5.5(a) shows the XRD patterns of $Fe_{71.3}Pd_{28.7}$ nano-rods embedded in PAA template annealed at different temperatures from 600 °C to 800 °C for 1 min. For thermal annealing temperature below 700 °C, the dominate phase is disordered fcc (γ-Fe, Pd) solid solution phase. At the same time, the weak bcc (110) peak ($2\theta = 44.5°$) still exist, indicating the incomplete homogenization of the crystal structure. When the annealing temperature reaches to 720 °C , the peak of bcc (α-Fe,Pd) solid solution phase completely disappear, indicating the formation of single disordered fcc (γ-Fe, Pd) austenite phase. This temperature is around 50 °C lower than the one for bulk $Fe_{70}Pd_{30}$ binary alloy [42]. Because of the small size effect, it is also expected that the martensite starting temperature (Ms) of nano-sized Fe-Pd alloy is lower than that of the bulk Fe-Pd alloy. The average crystallite size was calculated by Debye-Scherrer formula:

$$D = \frac{k\lambda}{\beta\left(\theta\right) cos\left(\theta\right)} \tag{5.2.1}$$

where D is the average dimension of the crystallites, k is the Scherrer constant (0.94 is used in this case), λ is the wavelength of X-ray source (1.5406Å is used in this case), B is the full width at half maximum of the peak intensity in radians on a 2θ scale and θ is the Bragg diffraction angle.

The average crystallite size of $Fe_{71.3}Pd_{28.7}$ nano-rods obtained at 600 °C, 650 °C, 700 °C, 720 °C, 750 °C, 770 °C and 800 °C are shown in Fig.5.5(b) respectively. Below the melting temperature of the nanorods, the grain continuously grows with the increasing annealing temperature. At 800°C, the crystallite size reaches up to 25nm. Fig.5.6 shows the XRD pattern and the calculated crystallite size of $Fe_{71.3}Pd_{28.7}$ nano-rods annealed at 800°C for different duration. When annealed at 800°C, the nanorods show the same disordered fcc austenite single phase. The crystallite size of Fe-Pd nanorods shows a slight increase with longer annealing time.

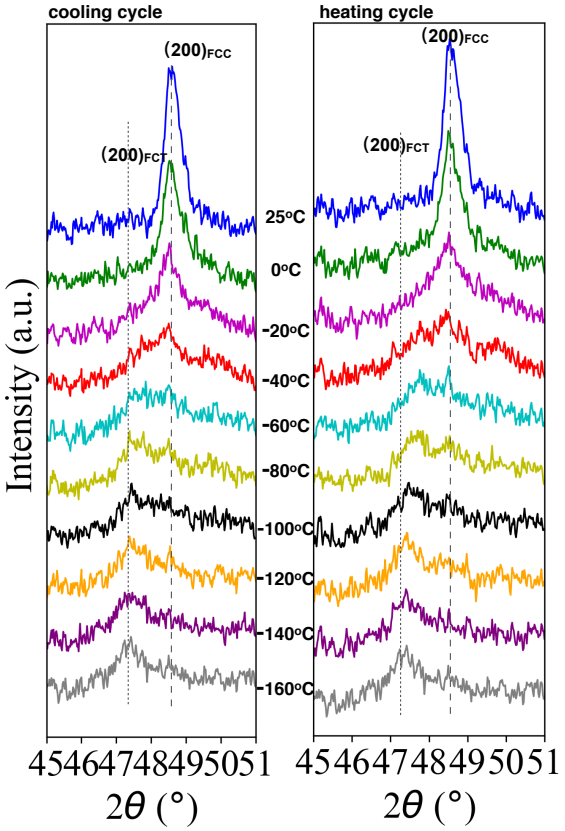

Figure 5.7: XRD pattern of extracted freestanding $Fe_{69.7}Pd_{30.3}$ nanorods annealed on Si wafer at 800 °C for 30 min during the (a) cooling and (b) heating cycle between 25°C and −160°C.

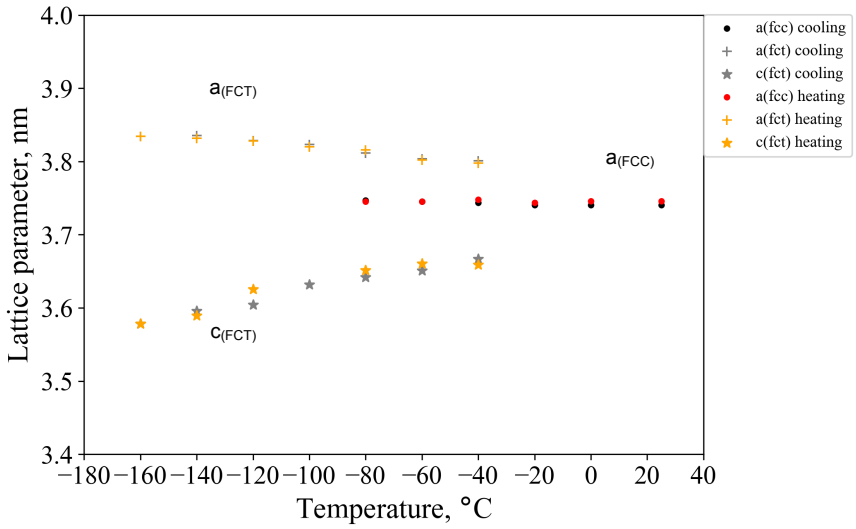

Figure 5.8: Change in lattice parameters of $Fe_{69.7}Pd_{30.3}$ of extracted free-standing $Fe_{69.7}Pd_{30.3}$ nanorods annealed on Si wafer at 800 °C for 30 min during the cooling cycle between 25°C and −160°C.

5.2.5 Thermal Elastic Behavior of Fe-Pd Nanorods

In order to investigate the phase transformation of $Fe_{70}Pd_{30}$ nanorods, we conducted *in situ* XRD measurement with cooling and heating cycles between room temperature and -160°C.The extracted free-standing $Fe_{69.7}Pd_{30.3}$ nanorods annealed on Si wafer was first investigated since the aggregation of nanorods during the annealing process makes it behave more closely to already known bulk $Fe_{70}Pd_{30}$ [116], which will verify the feasibility of $Fe_{70}Pd_{30}$ FSMA nanorods synthesis by our method. Fig.5.7 shows the *in situ* XRD measurements of extracted free-standing *Fe-Pd* nanorods annealed without PAA template during cooling cycle and heating cycle between room temperature and -160°C. At the cooling cycle, the fcc (200) ($2\theta = 48.6°$) peak gradually weakens until completely invisible at -100°C. The fcc (200) peak gradually weaken and split into two peaks which can be attributed to fct (200) and fct (002). The new peaks start to be visible on XRD data from -40°C and grow stronger while decreasing the temperature. At the successive heating cycle starting from -160°C, the fct (200) and fct (002) peaks merge to the center fcc (200) peak until disappear. The center fcc (200) peak grows sharper, and the intensity becomes higher from $-80°$ to room temperature. However, the position of the fcc (200) peak almost kept unchanged. The *in situ* XRD result during cooling and heating cycles indicates that the austenite-martensite transformation is fully reversible. It proves that FSMA $Fe_{70}Pd_{30}$ nanoalloy can be synthesized by the current electrodeposition in PAA followed by annealing and quenching.

The lattice parameters of fcc austenite phase and fct martensite phase are calculated from fcc (200), fct (200), and fct (002) at various temperatures (Fig.5.8). The lattice parameter of fcc austenite phase at room temperature is calculated to be $a = 3.74$Å calculated with extrapolation method as a function of $cos^2(\theta)/sin(\theta)$. And the lattice parameter of fct martensite phase at -160°C is calculated to be $a = 3.83$Å$, c = 3.59$Å. (Note that the lattice parameters of fct martensite phase of bulk $Fe_{70.3}Pd_{29.7}$ reported by Oshima [116] at -80 °C are: a = 0.3860 nm and c = 0.3636 nm.) When there is only single fcc phase, the lattice parameter keeps unchanged with changing temperature. Between -40°C and -80°C ,both fcc

and fct phases coexist. Moreover, the a-axis of the fct phase keeps increasing, and c-axis of fct phase keeps decreasing with decreasing temperature from −40°C to −160°C. The martensite starting temperature (Ms) for extracted $Fe_{69.7}Pd_{30.3}$ nanorods annealed on Si is estimated to be −40°C when the martensite phase is first observed. And the martensite finishing temperature is estimated to be −80°C as the austenite fcc peak completely disappear. These Ms and Mf are close to the data of the bulk *Fe-Pd* due to the aggregation of nanorods during the thermal annealing process. The austenite starting and finishing temperature (Mf) can be estimated as the fcc (200) showing up temperature and the fct (200)/fct (002) peaks disappearing temperature. However, in the current XRD data, such hysteresis is not captured because of the large measurement interval (20°). The lattice parameters calculated in heating cycle almost overlap with those in cooling cycle, suggesting that the temperature hysteresis of the austenite-martensite transformation is very small.

The next step is to verify the martensite phase transformation in $Fe_{70}Pd_{30}$ nanorods with well defined size. The solution to avoid aggregation is to conduct the annealing while the *Fe-Pd* nanorods are still embedded in PAA template. We fabricated $Fe_{70}Pd_{30}$ nanorods with mean diameter of 65 nm and length around 1µm. Then we investigated the thermal-elastic behavior of the well defined nanorods by temperature dependent *in situ* XRD measurement and temperature dependent magnetization VSM measurement. TEM image of extracted *Fe-Pd* nano-rods from PAA template after annealing (Fig.5.9(b)) shows that the physical separation of *Fe-Pd* nano-rods by PAA template effectively prevents any agglomeration even annealed at high temperature (800°C). The diameter and length of the nano-rods are the same as the as-deposited samples. Fig.5.9(a) shows the XRD pattern of $Fe_{72.4}Pd_{27.6}$ nanorods (65nm in diameter and 1µm in length) at room termperature and −160°C. The peak at room temperature indicates the FCC austenite phase. At −160°C, no extra peaks of fct phase can be detected . However, a weakening of the fcc (200) peak suggests the incomplete martensite transformation might have already taken place at −160°C. Fig.5.10 shows the temperature dependence of magnetization of $Fe_{72.4}Pd_{27.6}$ nano-rods inside PAA template at 3000Oe on cooling between 400K and 50K. The magnetization keeps decreasing

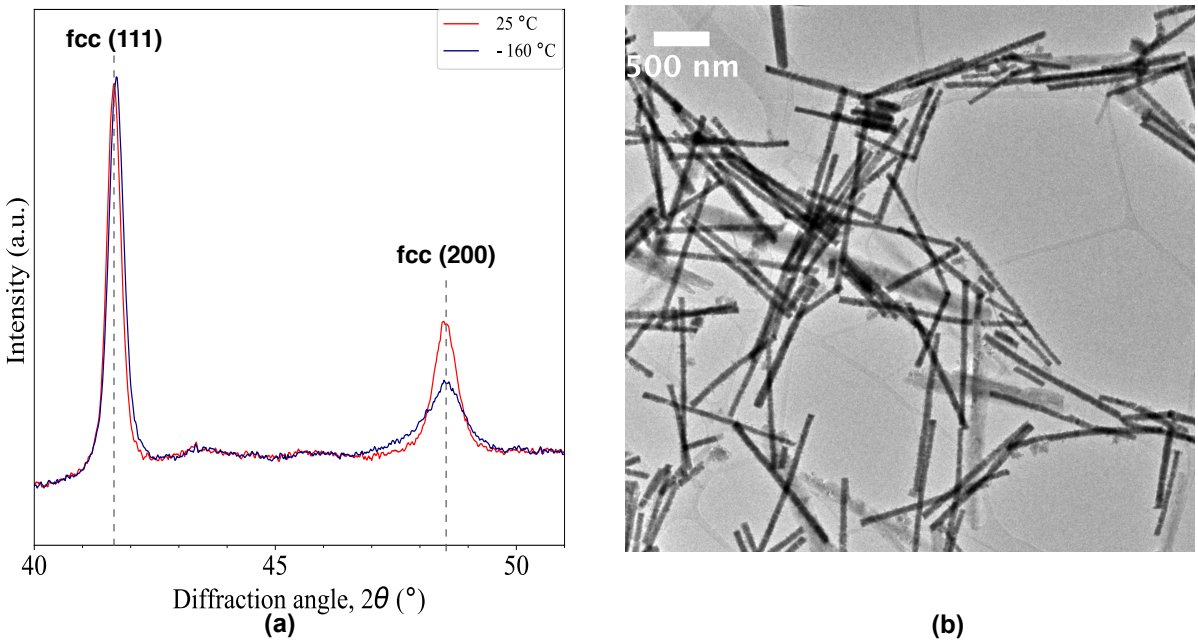

Figure 5.9: (a) XRD pattern of $Fe_{72.4}Pd_{27.6}$ nanorods with mean diameters of 65nm and length of 1µm embedded in PAA template annealed at 800°C for 1min at 25°C and −160°C. (b) TEM image of $Fe_{72.4}Pd_{27.6}$ nano-rods extracted from PAA template after annealing.

with decreasing temperature until $100K$, this visible change at $100K$ which is very close to the observed austenite weakening by XRD (Fig. 5.9) might suggest the starting point of the martensite transformation. Compared to aggregated Fe-Pd nanorods whose starting martensite transformaion temperature is −40°C, the phase transformation of well defined nano-rods are much lower (around $100K$). Such difference is caused by the large strain energy in small sample that requires large driving force for the phase transformation [118] .

5.2.6 Magnetic Property

Hysteresis loops measured for annealed $Fe_{71.3}Pd_{28.7}$ nanorods in PAA template are shown in Fig. 5.11. From the shape of the hysteresis curve, the easy axis for magnetization is perpendicular to the main axis of nanorods which oppose the shape anisotropy of a single metal wire. The perpendicular aligned easy magnetization axis cannot be explained by the dipolar

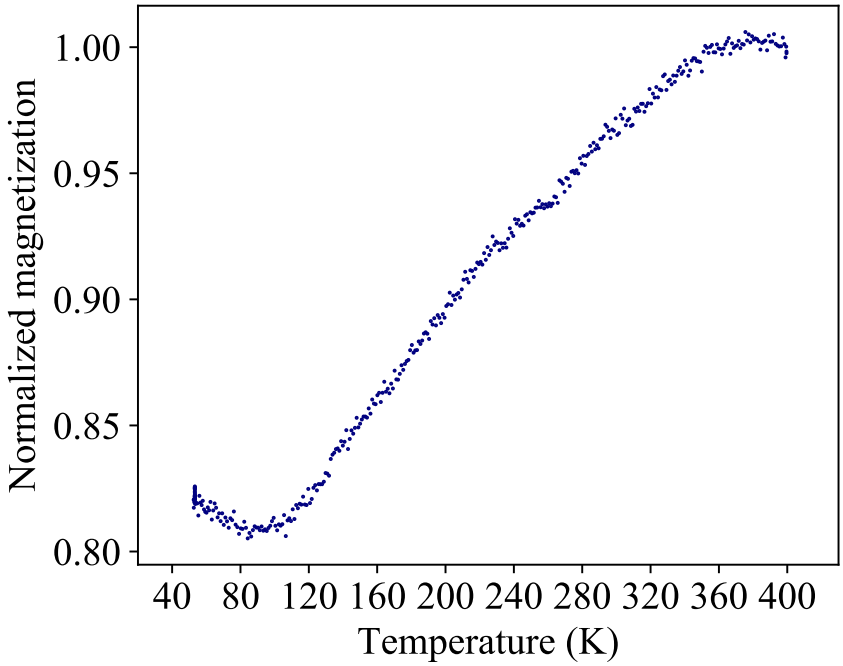

Figure 5.10: Normalized magnetization as a function of temperature of the $Fe_{72.4}Pd_{27.6}$ nanorods annealed inside PAA at 800°C for 1 min . Measured when nanorods are embedded in PAA at an applied magnetic field of 3000 Oe, along the length of nanorods.

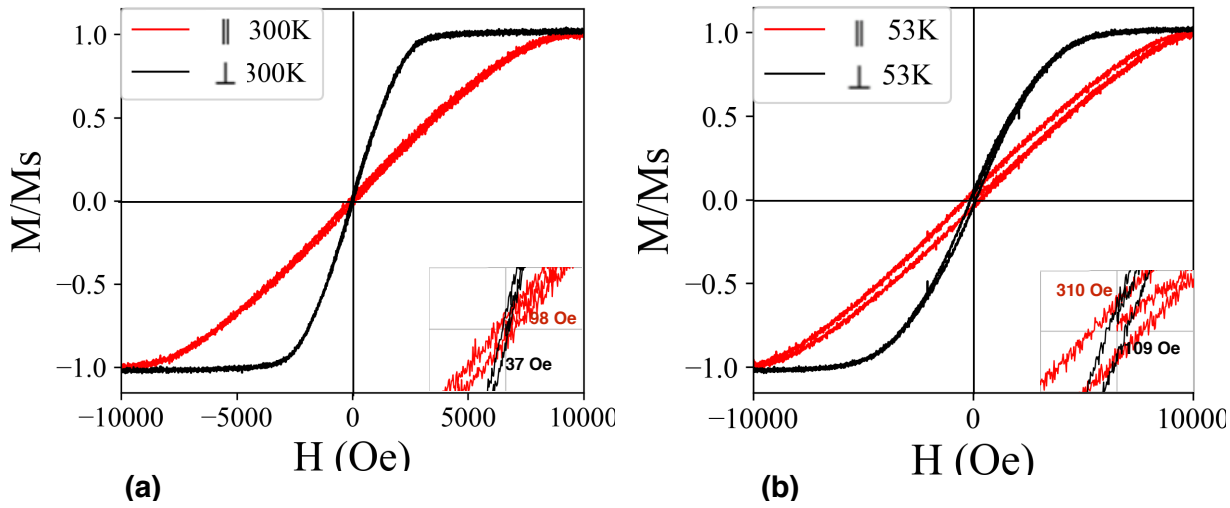

Figure 5.11: M-H hysteresis loops measured on an array of annealed $Fe_7$1.3$Pd_2$8.7 nanorods (65 nm in diameter) embedded in PAA tempalte annealed at 800 °C for 15 min with the magnetic field applied parallel (red plot) and perpendicular (black plot) to the rod axis at (a) 300 K and (b) 53 K.

coupling between magnetic nanowire array. Based on Encinas-Oropesa [119] *et al* 's mean-field model, the demagnetization factor is related to the volume fraction of nano-cylindrical holes of the template (P), leading to demagnetization factor of P parallel the nanorod axis direction and the demagnetization factor of $(1-P)/2$ perpendicular to the nanorod axis direction. For an ideal PAA template with hexagonally packed cylindrical pores, the volume fraction of the cylindrical pores can be calculated as $P = \frac{\pi}{2\sqrt{3}}\left(\frac{D_p}{D_{int}}\right)^2$ where D_p is the pore diameter (which is 65 nm here) and D_{int} is the distance between the centers of adjacent pores (which is 110 nm here). The calculated demagnetization factors are 0.317 and 0.342 in the parallel and perpendicular direction, indicating that the hysteresis loop is very close considering the shape anisotropy and dipolar interaction between nanorods. The large difference of the experimentally measured hysteresis loop on different directions to the nanorods must origins from other anisotropy factors, like magnetocrystalline anisotropy and magnetoelastic anisotropy. The magnetocrystalline anisotropy of $Fe_{70}Pd_{30}$ austenite phase only slightly prefers the [111] direction [17]. Moreover, the Fe-Pd nanowires are packed with a preferred orientation in the [111] direction as is evidenced by the XRD data (One typical XRD pattern of Fe 69.8 at.% nanorods in Fig. 5.4 shows a [111] to [200] peak intensity of 3.86 which is much larger than the standard value of 2.28 (obtained from ICDD 04-006-5955)). Therefore, the magnetocrystalline anisotropy is not responsible for the magnetic reversal behavior in our Fe-Pd nanorod array. The most possible reason for the easy magnetization perpendicular to the nanorods might result from the magnetoelastic anisotropy in metal nanorods in PAA template resulted from the thermal expansion coefficient difference [120]. Indeed, our nanorods annealed in PAA are under residual stress (By comparing the two nanorods samples of the same chemical composition determined by SEM-EDX that are annealed without ($Fe_{69.7}Pd_{30.3}$ in Fig.5.3(a)) and within ($Fe_{69.7}Pd_{30.3}$ in Fig.5.4(a)) PAA template, the [111] peak shift from $2\theta = 41.72^\circ$ to lower angle $2\theta = 41.60^\circ$). As the measuring temperature decrease to 53 K, the hysteresis loop open up for both parallel and perpendicular applied field direction, showing increased coercivity. This is caused by the drop of thermal fluctuation at lower temperature, requiring a greater magnetic field to help to overcome the magnetic

anisotropy energy.

5.2.7 Crystal Structure and Thermalelastic Phase Transformation of Fe-Pd Nanohelices

Crystal Structure of Electrodeposited Fe-Pd Nanohelices

Transmission electron microscopy (TEM) analysis is performed for a single nanohelix with average Fe atomic percentage of 55.4 at.% and 72.3 at.% determined by EDX individually. The measured crystallite size based on the dark field image is averaged to be 6.4 nm for 55.4 at.% Fe helix and 7.4 nm for 72.3 at.% Fe helix. The electron diffraction pattern for the Fe 55.4 at.% helix shows a fcc polycrystalline structure with the calculated lattice constant a=0.366 nm by electron ring diffraction pattern. The high-resolution image is taken with the beam direction [011]. Based on the $[\bar{1}1\bar{1}]$ interplaner distance, the lattice constant is calculated to be 0.384 nm. The electron diffraction pattern of 72.3 at.% Fe helix shows mainly bcc phase (indexed in orange) and some fcc phase. The lattice constant calculated from the ring diffraction pattern for the fcc phase is 0.357 nm while for the bcc phase is 0.268 nm. The lattice constant calculated from the HRTEM is 0.293 nm for the bcc phase. This suggests that both the $(\gamma - Fe, Pd)$ fcc solid solution and $\alpha - Fe$ solid solution coexist for $Fe_{72.3}Pd_{27.7}$. The lattice constants measured from electron diffraction pattern are lower than the literature values. While the lattice constant measured from HRTEM image is in a good agreement with other researchers [79].

Similar annealing procedures are applied to Fe-Pd nanohelices synthesized by $PAA - SiO_2$ hybrid template at 800°C for 1min followed by compressed gas cooling. $Fe_{70.7}Pd_{29.3}$ helices shows single fcc austenite phase at room temperature after annealing in template. When the measuring temperature is lowered to -160 °C, the splitting of (200) peak is not observed, and no obvious weakening as in Fe-Pd nanorod case is observed. The significant lowering of martensite starting temperature (Ms) can be explained by the size effect in nanohelices. Seki *et. al.* [118] observed a monotonically decreased martensite starting temperature with decreasing grain size. They attribute the significant lowering of Ms in

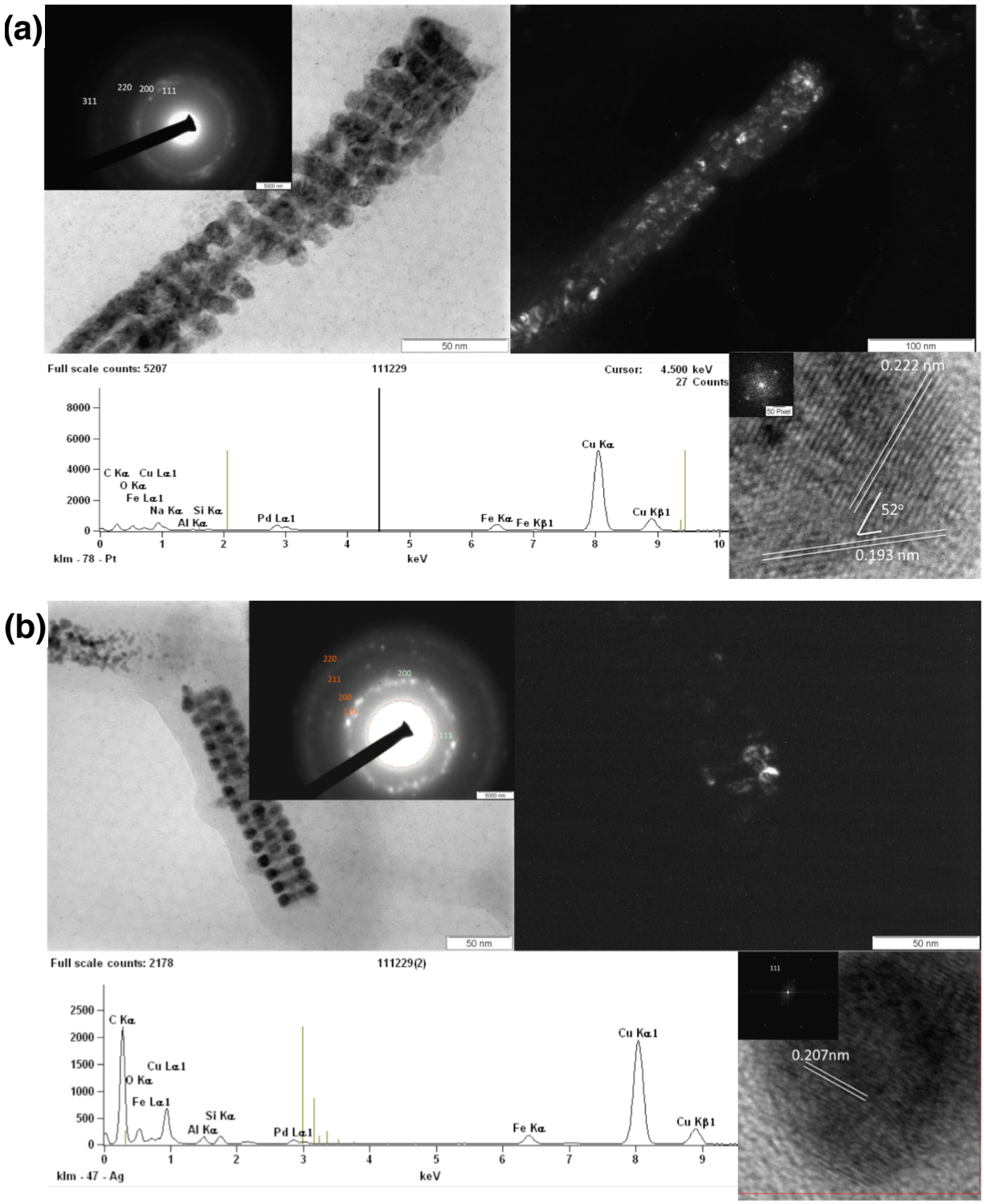

Figure 5.12: TEM bright field image with the corresponding electron diffraction, dark field image, EDX spectrum and high resolution image for (a) 55.4 at.% Fe deposited from Electrolyte 1 at E_1=-1.166 V, t_1=60 s, E_2=-0.066 V, t_2=120 s (b) 72.3 at.% Fe deposited from Electrolyte 2 at E_1=-1.100 V, t_1=15 s, I_2=0 A, t_2=30 s.

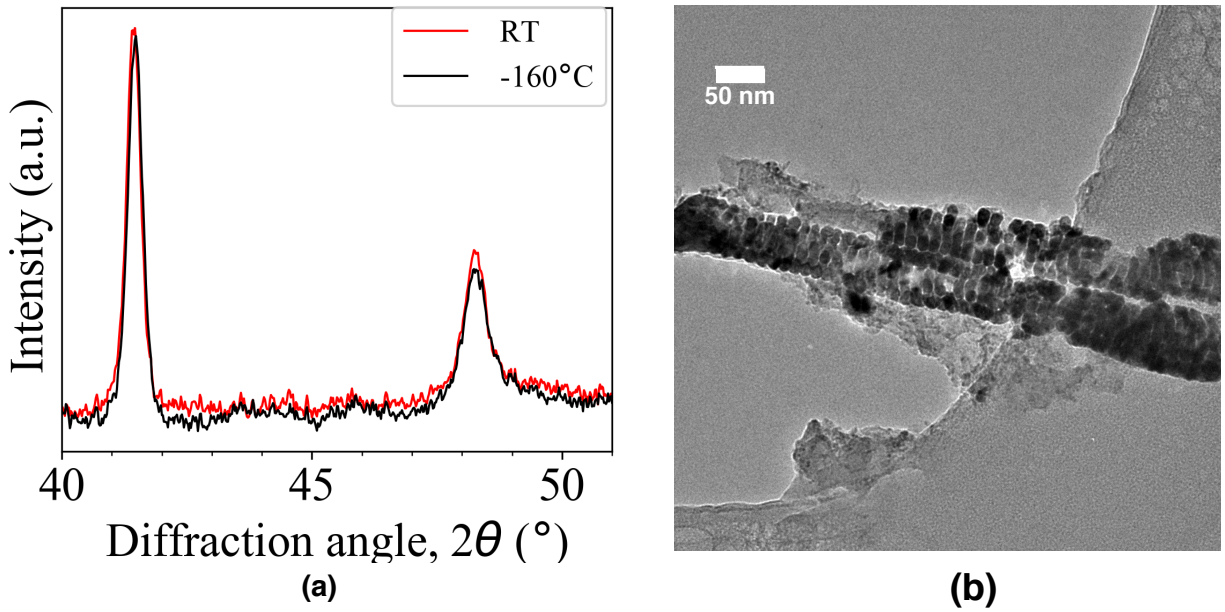

Figure 5.13: Ta) XRD pattern of $Fe_{70.7}Pd_{29.3}$ nanohelices with a diameter of 10 nm embedded in $PAA - SiO_2$ template annealed at 800°C for 1min at 25°C and −160°C. (b) TEM of $Fe_{70.7}Pd_{29.3}$ nanohelices extracted from $PAA - SiO_2$ template after annealing.

nanoparticle to that (1) the free energy on the surface of nanoparticle prevents the formation of martensite variants and (2) the nanoparticles easily relax the stored strain during the rapid cooling process which is advantageous for martensite formation. By analogy to the polycrystalline material, it is also possible that the nanorods go through the single nano-variant mode in which the large strain energy has to be compensated by larger chemical free energy. We recently studied this subject to conclude that the shape of Fe-Pd nano-materials has a strong influence on the phase transformation behavior where the effect of residual stress plays a key role [117].

5.3 Conclusion

We successfully synthesized $Fe_{70}Pd_{30}$ nanowires with homogeneous spatial and single wire chemical composition. The as-deposited $Fe_{70}Pd_{30}$ nanowires exhibit a mixture of fcc and

bcc phases at room temperature. When the nanowires are annealed higher than 720 °C for at least 1 min followed by compressed air quenching, a single fcc austenite phase is formed. For $Fe_{70}Pd_{30}$ nanorods which is 65 nm in diameter and 1 µm in length annealed without PAA template (which shows partial sintering with agglomerated particle size up to 700 nm), the reversible thermal elastic phase transformation is observed by XRD with martensite starting temperature at around -40 °C. For the $Fe_{72.4}Pd_{27.6}$ nanorods annealed inside PAA template, which retain the 65 nm diameter and 1 µm length, shows the sign of decreasing of fcc austenite phase at -160 °C. The annealed $Fe_{70}Pd_{30}$ nanorods array shows a reverse easy magnetization direction which might result from the magnetoelastic anisotropy. $Fe_{70.7}Pd_{29.3}$ nanohelices with a wire diameter of 10 nm shows no martensite phase transformation above -160 °C.

Chapter 6

MORPHOLOGY OF *FE-PD* NANOWIRES ORIGINATED FROM BLOCK COPOLYMER-SILICA CO-SELF-ASSEMBLY UNDER CYLINDRICAL CONFINEMENT

Block copolymers (BCPs) are macromolecues composed of two or more chemically distinct polymeric chains (blocks) that covalently linked together. Depending on the number of different components (such as AB diblock copolymer and ABC triblock copolymer), the compositions of different blocks and the linking chain architecture (such as linear, star, branched and cyclic), they form a variety of different systems. When the different blocks are immiscible, phase separation occurs to minimize the contact between dissimilar blocks. However, opposed to the mixture of immiscible polymers, the macrophase separation is avoided by the connection between the immiscible blocks. Thus, the competition between the entropic chain-conformational energy and the enthalpic interaction energy causes the remarkable property of block copolymers to self-assemble in the melt into a variety of ordered structures with the periodic domain ranging from 5 nm to 100 nm [121]. Such periodic micro-structure is controlled by the chain architecture, relative composition of each block (f_i), the degree of polymerization (N) and monomer-monomer interaction (characterized by Flory-Huggins interaction parameter χ). For the simplest linear AB diblock copolymer melt, the microphase structures including lamella, hexagonally packed cylinders, body center cubic spheres and a bicontinuous gyroid phase are observed experimentally and theoretically [122, 123]. The large varieties of ordered patterns formed by block copolymer microphase separation enable their applications in nanolithography [124, 125], fabrication of mesoporous networks [126, 127], periodic self-assembled photonic band gap materials [128, 129].

More interesting, by placing block copolymers in geometrical confinement whose scale

is comparable with the block copolymer domain spacing, varieties of novel morphology are formed as a result of the interaction between block copolymer equilibrium morphology and the confinement environment symmetry. The compressing or stretching of polymer chains caused by the mismatch between the block copolymer domain spacing and the physical confinement is energetically unfavorable. Therefore, the block copolymer self-assembles into novel morphologies deviating from the bulk phase to release the compressing or stretching. In general, the geometrical constraints imposed by the physical confinement and the confinement surface-polymer interactions play the key role in the final morphology of confined block copolymers. Focused on these critical parameters, researches on the dimension (1D thin films, 2D cylindrical pores, 3D spheres) and geometry (size and shape) of the confinement environment, the interaction between polymer and confinement wall (neutral, attractive to a specific block) have attracted considerable attention.

Computer simulation methods play an important role to understand the mechanism of confined self-assembly of the block copolymer and to predict the phase separation of a specific block copolymer under a certain environment. In recent years, a large amount of computational studies are dedicated to describe the microphase separation of confined BCPs by simulated annealing technique [130, 131, 65, 132, 133, 134], self consistent field theory [66, 60, 67, 68, 69, 70, 71, 72], dynamic density functional theory (DDFT) [135, 136, 137] and Monte Carlo simulation [138, 139, 140, 141]. Under 1D slab confinement, the degree of incommensurate (characterized by the ratio between the film thickness t and the BCP bulk period L_0) and the polymer-wall surface interaction determine the orientation of the periodic structure (whether parallel to the slab wall or perpendicular to the slab wall) and the appearance of the novel structure deviating from the bulk phase [135, 137, 130, 69]. Under 2D cylindrical confinement, lamella forming AB diblock BCPs generally forms concentric cylinders [138, 140]. Yu *et al.* [132] explored a larger parameters space of the degree of confinement (D/L_0 where D is the diameter of confining pore) and cylinder wall-polymer interaction with a simulated annealing technique and concluded that (1) for strong polymer-cylinder wall interaction, concentric cylinders are always formed (2) for neutral cylinder

wall, perpendicularly stacked lamella are always formed regardless of the degree of frustration while (3) for weakly attractive wall, more complex structure like helices might form. For cylinder-forming AB diblock copolymer melt under cylindrical confinement, Shi's group conducted a systematic study on the microphase evolution of cylinder-forming AB BCP melt from highly frustrated pore (D/L_0=0.5) to moderately frustrated pore ($D/L_0 = 4.5$) for majority block attracting, minority block attracting and neutral wall [65, 134]. The simulation result of Shi's group shows that for $D/L_0 < 2.7$, variety of microstructure evolutions covering a string of spheres, straight cylinder, twisted cylinder, a single helix, a double helix, a set of degenerate structures of single helix, stacked toroids and double helix are observed. When the diameter of the confining cylinder increase to $D/L_0 > 2.7$, a two layers structures are formed. With either helices or stacked toroids as the outer layer, the structure of the new layer evolution follows the formation sequence above: from a string of beads to a set of degenerate structures (S-helix, stacked toroids and double helix). In addition, Yu *et al.*'s simulation [65] also points out that the curvature of the cross-section of the cylindrical pore is responsible for the formation of helices or toroids structure, while the non-circularity of the pore cross section favors the formation of cylinders packed along the axis of the confining pore length.

Experimentally, lamella- and cylinder- forming block copolymers are studied under 1D confinement [142, 137]. It is found that the confinement wall surface-polymer interaction and film thickness are the controlling factors for the resulted morphology. In the case of lamella-forming block copolymers, parallel lamella with period deviating form the bulk phase is formed if the confinement surface strongly attracts one block. While the weak or neutral wall preferential towards the blocks, perpendicular lamella might form due to the mismatch between the film thickness and block copolymer equilibrium period. In the case of cylinder-forming block copolymers, the interplay between the confinement wall-polymer interaction and the geometry frustration lead to rich morphologies from patterned dots, parallel oriented cylinders, perforated thin film networks and perpendicular oriented cylinders. On the other hand, block copolymers under 2D confinement, especially cylindrical confinement owing to

the development of well established porous anodic alumina (PAA) with uniform cylindrical pore size ranging from 10 nm to 400 nm, has brought more novel microphase morphology which can not be observed in the bulk and 1D confinement case. Sun *et al.* [143] observed concentric cylinders by confining lamella forming PS-b-PMMA in PAA nano-pores. Ma *et al.* [144] produced concentric lamella nanofibers by coaxial electrospinning of poly (styrene-b-dimethylsiloxane) (PS-b-PDMS) block copolymer as the core component and poly (methacrylic acid) (PMAA) homopolymer as the shell. Especially, Russell's group conducted a series of experiments by confining lamella-, cylinder- and sphere-forming PS-b-PBD inside PAA nanopores with various sizes [145, 146, 147, 148, 64]. For lamella forming PS-b-PBD, they observed concentric cylinders at large degree of frustration $D/L_0 > 3.4$ (where D is the diameter of the PAA pore and L_0 is the bulk block copolymer period) and at $D/L_0 \approx 1.9$. While at $D/L_0 \approx 2.6$, a stacked-disc or toroidal-type structure was observed. For sphere-forming PS-b-PBD, concentric cylinders, discontinuous spheres, zigzag patterned spheres are observed. For cylinder forming PS-b-PBD, they observed hexagonally packed cylinders with a period greater than the bulk L_0 oriented parallel with the axis of PAA pore. For highly incommensurate geometries, they observed a series of morphologies deviating from the bulk phases. From highest to relative lower degree of incommensurate, they identified horizontally stacked discs at $D/L_0 = 0.92$, horizontally stacked donuts at $D/L_0 = 1$, single helix at $D/L_0 = 1.27$, double helix at $D/L_0 = 1.6$, stacked donuts with center rod at $D/L_0 = 1.81$, single helix with center rod at $D/L_0 = 2.1$, double helix with center rod at $D/L_0 = 2.2$ and triple helix at $D/L_0 = 2.22$ of PBD block in PS matrix. In addition, Wu *et al.* [57] confined the Sol-gel silica-BCP composite system inside PAA template, creating mesoporous silica network with novel pore morphology resulted from the self-assembly of guiding BCP under cylindrical confinement. In a typical silica Sol-gel process using amphiphilic block copolymer as the structure directing reagent, the aqueous silica cations interact with the hydrophilic block of the BCP. Then the subsequent polymerization of the silica precursors within the domain of the hydrophilic blocks precisely replicates the original microphase separation of the block copolymer. Once the hydrophobic block is removed by calcination, the resulting

mesoporous silica network can be used as an ideal nanotemplate to cast morphologies of the hydrophobic block.

The common way to increase the period (as well as the hydrophobic domain) of the BCP-silica composite is to introduce organic swelling agent [126, 149, 150, 151, 152] or polymers [153, 154] that interact with the hydrophobic domain of the mesophases and ultimately expand they hydrophobic domain size as well as the equilibrium period.

In my Ph.D study, Fe-Pd nanowires were fabricated by electrodeposition using $PAA - SiO_2$ hybrid template with poly (ethylene oxide) (PEO) $_{20}$ poly (propylene oxide) (PPO) $_{70}$ poly(ethylene oxide) (PEO) $_{20}$ (P123) as structure guiding BCP. Various morphologies of Fe-Pd nanowires were investigated under different degree of confinement. A self-consistent field theory of AB BCP melt under cylindrical confinement was conducted to account for the morphology evolution of Fe-Pd nanowires. The second part of this study investigated the effect of Sol precursor concentration, different types of poloxamers, blending with small organic molecules, blending with different poloxamers and blending with poly (propylene oxide) homopolymer of different molecular weight on the equilibrium period of mesoporous silica thin film. This study guides the future work for the synthesis of Fe-Pd nanohelices with flexible scale.

6.1 Experimental Procedure

6.1.1 Experiment

PAA templates with various diameters were synthesized by the two-step anodization in 0.3 M oxalic acid at 40 V followed by various hole widening in 5 wt.% phosphoric acid. 10.4 g tetraethylorthosilicate (TEOS) was mixed with 5.4 ml HCl (pH = 2) and 15.21 ml ethanol under vigorous stirring for 20 min at room temperature. Then the prehydrolyzed silicon alkoxide was mixed with different structure guiding BCP (shown in Table.6.1) in 10.14 ml ethanol for 3 hours at room temperature. Later on this Si containing Sol infiltration into PAA nanopore was conducted by dip coating at a speed of 24mm/min at room temperature. The

PAA/Al template was then moved into environment chamber (ESPEC, TEMP. & HUMID CHAMBER PDL-3K) with relative humidity of 66% at 25 °C for 24 hours. Porous SiO_2 network was then further developed and triblock copolymer was removed by calcination at 500 °C for three hours (ramp rate 1 °C/min). To observe the bulk BCP period, the same Sol solution was dip coated onto a piece of Al foil and a piece of glass slide following the dip coating of PAA template at the withdrawal speed of 120 mm/min. For trimethyl-1,3,5 benzene (TMB) swelling experiment at elevated temperature, the precursor mixture was stirred at 45 °C for 3 hours, followed by dip coating at 120 mm/min at room temperature. After the dip coating, samples were immediately transfered to environment chamber for aging at 80 °C , 66 % RH for 24 hours.

To characterize the morphology of Fe-Pd nanowires, two types of samples are prepared in the following way (1) free-standing Fe-Pd nanowires were extracted from $PAA - SiO_2$ template by 1 M NaOH at 50°C. After cleaning *via* centrifugation with DI H_2O, the sample was transferred to a copper TEM sample grid or a silicon wafer for SEM characterization; and (2) Fe-Pd nano-wires together with $PAA - SiO_2$ template were embedded in epoxy resin followed by microtome slicing. Then the sliced cross-section of Fe-Pd in $PAA - SiO_2$ were transferred to a copper TEM sample grid.

To characterize the mesoporous silica, grazing incident small angle X-ray scattering (GISAX) (Bruker D8 Discover with IS 2-D XRD System) and atomic force microsopy (AFM, Bruker Dimension ICON) were performed on the silica thin film dip-coated on the glass slide. All the measurements were conducted with an incident angle of 0.25 °. Interpretation of the GISAXS patterns was aided by NANOCELL [155, 156], a Mathematica-based program that simulated quantitatively the positions of Bragg peaks at any incidence angle above the critical angle. This simulation program used the distorted wave Born approximation to account for the effects of refraction and reflection at coating-substrate and coating-air interfaces. To observe the cross-section of mesoporous silica thin film, silica thin film on soft Al foil was embedded in epoxy followed by microtome slicing. The sliced mesoporous silica on Al foil was transferred to a copper TEM grid.

6.1.2 Simulation

The bulk structures of the diblock copolymer melt are obtained using a pseudospectral self-consistent field theory (SCFT) numerical scheme ,with periodic boundary conditions in all three dimensions.Part of the simulation is based on an open-source C++ program Polyorder kindly provided by Liu [73]. The confinement in cylindrical geometry is realized by setting the end-segment distribution functions and polymer densities to be zero outside the surface of confinement. The modified program PolyorderConf for microphase calculation of block copolymer under cylindrical confinement is free for academic use upon request to the author of this thesis. In the calculation, $f_a = 0.3$ and $\chi N = 20$ are chosen for the AB block copolymer to ensure that the bulk phase is hexagonal packing cylinders. We start from random field initial guess, and varies the degree of confinement D/L_0. For different pore diameters, we changed cubic lattice size (lx $\times$ ly $\times$ lz) in the calculation from $32 \times 32 \times 32$ to $160 \times 160 \times 32$. The surface attracts B block of the diblock copolymer melt. The surface field is formulated as $\frac{H(\mathbf{r})}{\chi N} = v_0(e^{(|\mathbf{r}|-R)/\lambda} - e^{-\sigma/\lambda})$ for $R - \sigma \leq |\mathbf{r}| \leq R$, while $H(\mathbf{r}) = 0$ for $|\mathbf{r}| < R - \sigma$ [157], where v_0 is chosen to be 0.2 , σ=0.075 and λ=0.15.

precursor	Sol1	Sol2	Sol3	Sol4	Sol5	Sol6
Main polymer	2.78 P123	2.55 P123	3.05 P123	3.56 P123	2.78 L101	2.78 L121
Other agent	0	0	0	0	0	
precursor	Sol7	Sol8	Sol9	Sol10	Sol11	Sol12
Main polymer	2.78 L92	2.78 P103	2.78 P105	2.78 F127	2.78 P123	2.78 P123
Other agent	0	0	0	0	1.39 TMB	2.78 TMB
precursor	Sol13	Sol14	Sol15	Sol16	Sol17	Sol18
Main polymer	2.78 P123	2.78 P123	2.52 P123	2.22 P123	1.86 P123	2.52 P123
Other agent	4.17 TMB	5.56 TMB	0.26 L121	0.56 L121	0.92 L121	0.26 F127
precursor	Sol19	Sol20	Sol21	Sol22	Sol23	Sol24
Main polymer	2.22 P123	1.86 P123	2.78 P123	2.78 P123	2.78 P123	2.78 P123
Other agent	0.56 F127	0.92 F127	0.28 PPO	0.56 PPO	0.83 PPO	1.39 PPO

* In unit gram. P123: $EO_{20}PO_{70}EO_{20}$, L101:$EO_4PO_{59}EO_4$, L92: $EO_8PO_{47}EO_8$, P103: $EO_{17}PO_{85}EO_{17}$, P105: $EO_{37}PO_{56}EO_{37}$, F127: $EO_{106}PO_{70}EO_{106}$

Table 6.1: Structure guiding agents used in different Sol precursors

6.2 Results and Discussion

6.2.1 Morphology Evolution of Fe-Pd Nanowires under Cylindrical Confinement

To estimate the bulk P123-silica microphase period, Sol1 was dip coated onto the substrate to generate a 400 nm thick film. The cross sectional TEM image (Fig.6.1(a)) of such composite film from Sol1 shows a distorted hexagonally packed cylinders of PO block in an EO-silica matrix caused by uniaxial contraction along the film thickness direction (the contraction of the thin film is illustrated in Fig.6.1(c)). TEM image indicates that the 'a' axis of the cylinders is 12.93 nm and the 'b' axis is 18.35 nm. The AFM plan view of the cylinders arranged parallel to film surface shows a similar a value of 11.38 nm. The observed spots of the GISAX pattern of the P123-silicate thin film are in good agreement with the simulated c2mm structure with a=13.3 nm and b=18.6 nm by NANOCELL. The lattice parameters obtained from TEM, AFM and GISAX simulated result are very close to each other. There-

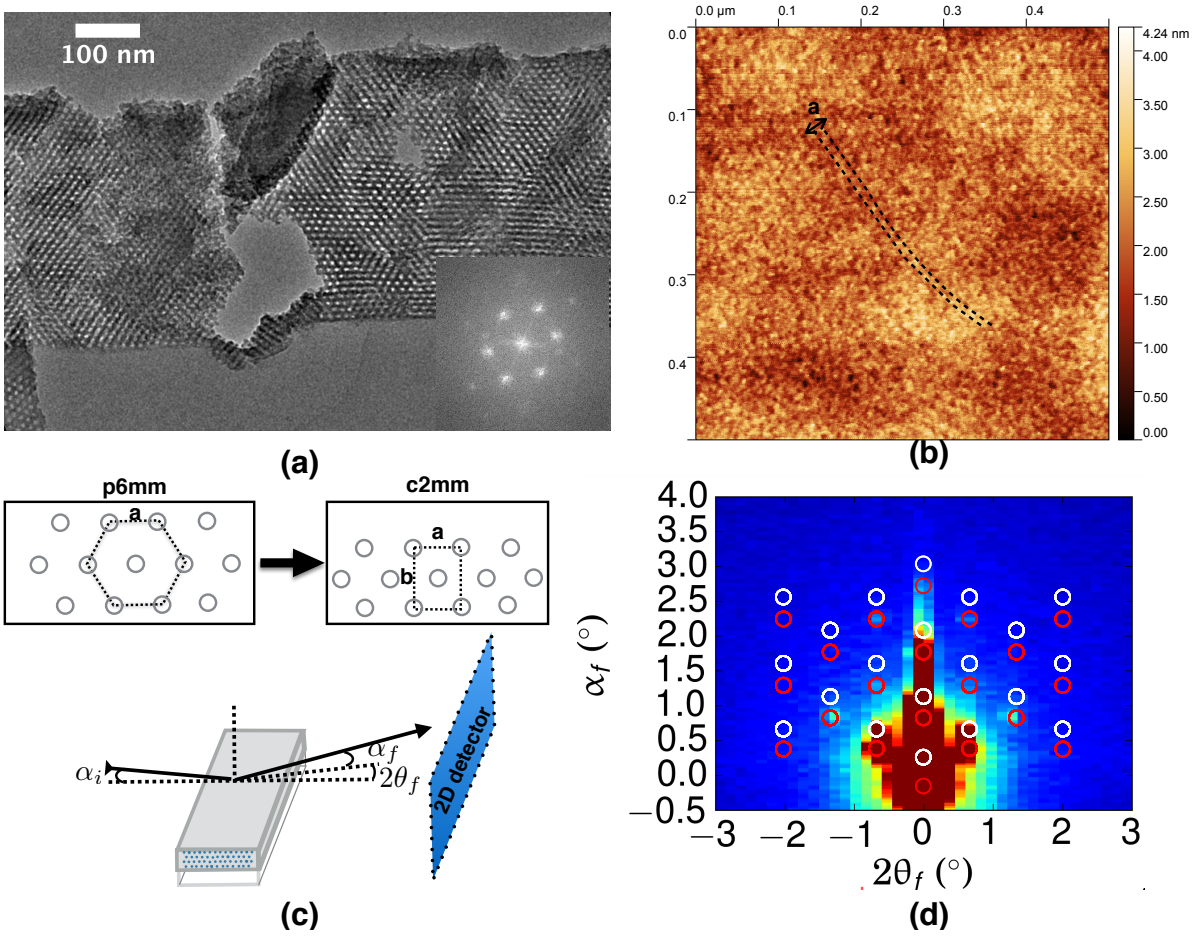

Figure 6.1: (a) TEM image of cross sectional view of as-synthesized P123-silica composite film showing that the a and c axis are parallel to the film plane. The inset is the corresponding FFT image (b) AFM micrograph of plan view of as-synthesized P123-silica composite film on glass slide showing parallel aligned tubes. The dotted line is guide for the eyes (c) Schematic illustration of GISAX data collection setup and the evolution from p6mm symmetry to c2mm symmetry (d) GISAX pattern of as-synthesized P123-silica thin film (Sol1). The overlay of simulated spots is from a NANOCELL simulation of c2mm . The red and white circles identify transmitted and reflected Bragg peaks, respectively.

fore Sol1 generates hexagonally packed cylinders with a period of around 13 nm outside cylindrical confining geometry.

When the sol-gel reaction is confined in cylindrical nanopores, novel morphologies besides the bulk hexagonal cylinders can be observed. Fig.6.2 shows a variety of morphologies of Fe-Pd nanowires deposited in cylinder forming BCP-silica composite as the diameter of PAA varies. The EO domain is occupied by silica to form the template; And the electrodeposited Fe-Pd nanowires inherit the morphology of PO domain. At highly incommensurate confinement geometry $D = 25.43$ nm, the Fe-Pd nano-wires show zigzag arranged spheres along the main axis. As the diameter of confining PAA increase, stacked inclined donuts show up at $D = 27.21$ nm followed by single helix, triple helix and double helix at $D = 30.81, 30.98$ and 31.39 nm. As the confining diameter keeps increasing, the morphologies become more complicated with a center rod, helix or toroid as the inner layer inside the helix or toroid outer layer. Single helices can be observed at $D = 30.81, 35.6, 44.30, 55.64\ nm$. Fig.6.3 shows the cross-sectional view of the Fe-Pd nanowires synthesized with various confining diameters. Single layer structure can be observed below 30 nm, and also at 36.15 nm, 37.61 nm, 37.88 nm, 40.11 nm, 40.93 nm, 43.01 nm, 45.09 nm, 59.29 nm, 61.93 nm, and 63.15 nm. These single layer structures give rise to the formation of nanohelices. Except these occasionally appeared single layer morphology, a general rule is that the layers of the resulted structure increase with increasing confining diameter: at small confining diameter below 30nm, the PO block forms single layer morphology in EO matrix. As the confining diameter increase, a second layer which is a center rod, or double wires, or helix/toroid structure show up. When the diameter becomes larger than 59.98 nm, a third layer which is a center rod, or multi rods appear inside the outer two helix/toroid layers. For the noncircular cross-sectional view at D= 43.18, 51.52, 53.71 nm, 56.79 nm, 61.91nm and 65.85nm, multiple rods are favored than helix/toroid structure which supports the simulation result that curvature of the confining cylinder is crucial for the formation of helix/toroid [65].

Fig.6.4 shows the structure evolution of AB block copolymer melt under cylindrical confinement when the cylindrical wall attract B block, $f_a = 0.3, \chi N = 20$. At the high degree

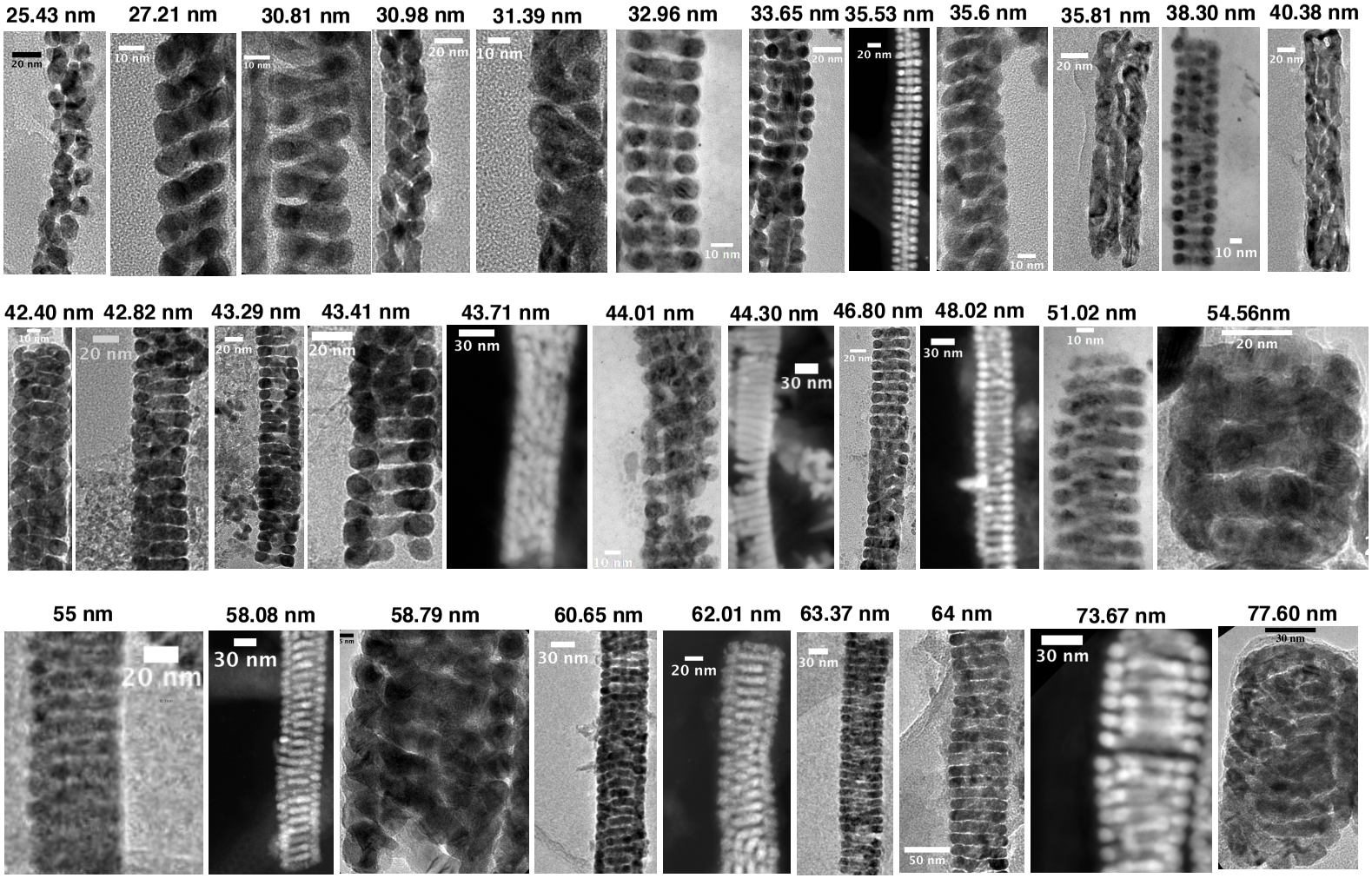

Figure 6.2: TEM images of free-standing *Fe-Pd* nanowires synthesized by bulk cylinder forming P123-silica composite (Sol1) inside PAA with various diameters viewing along the main axis of nanowires. The outer diameter of the *Fe-Pd* nanowires ranges from 25.43 nm to 77. 60 nm shown on top of each image.

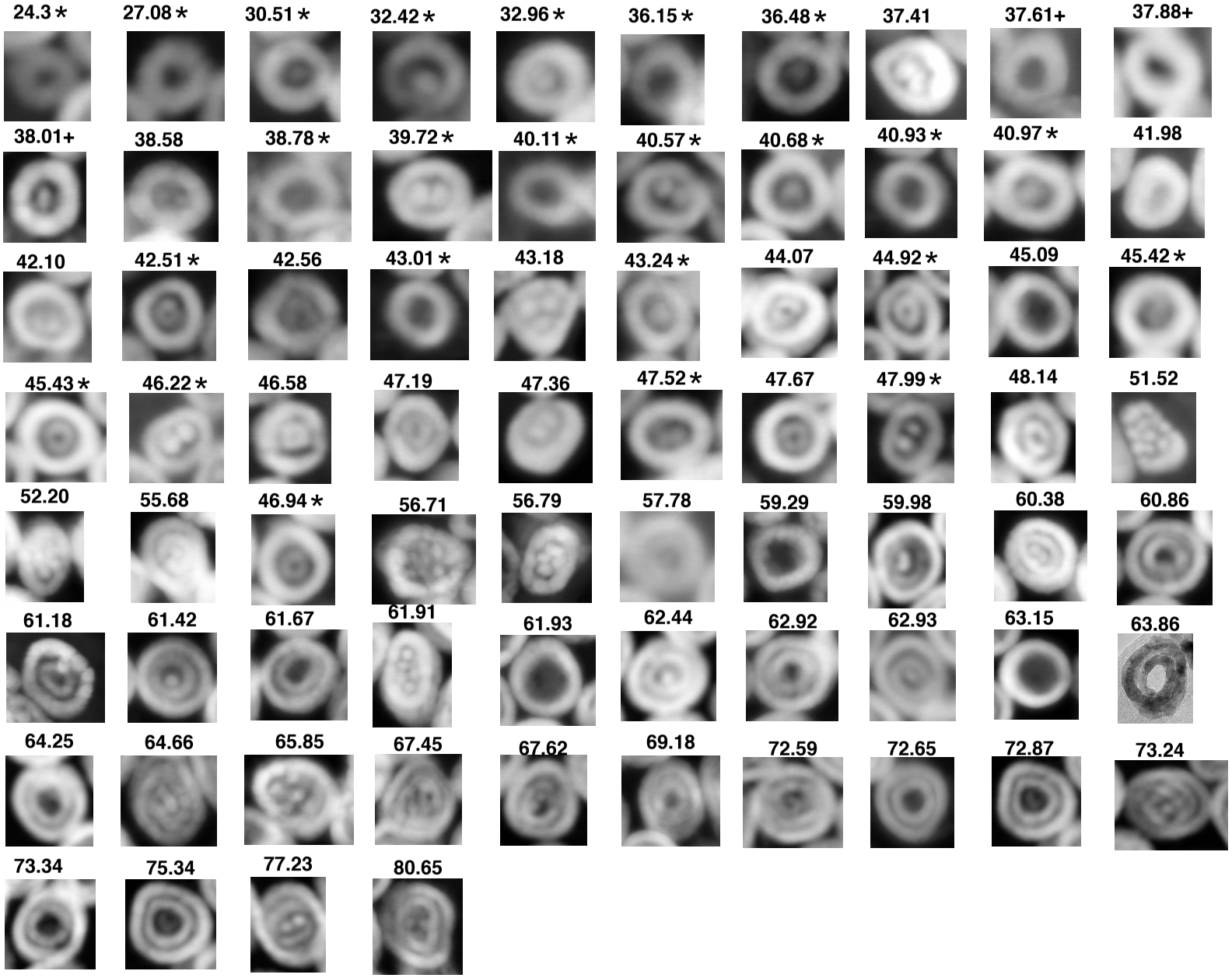

Figure 6.3: Cross sectional TEM images of free-standing *Fe-Pd* nanowires synthesized by bulk cylinder forming P123-silica composite inside PAA with various diameters (* samples are from Sol2, + samples are from Sol3 and the other samples are synthesized from Sol1).

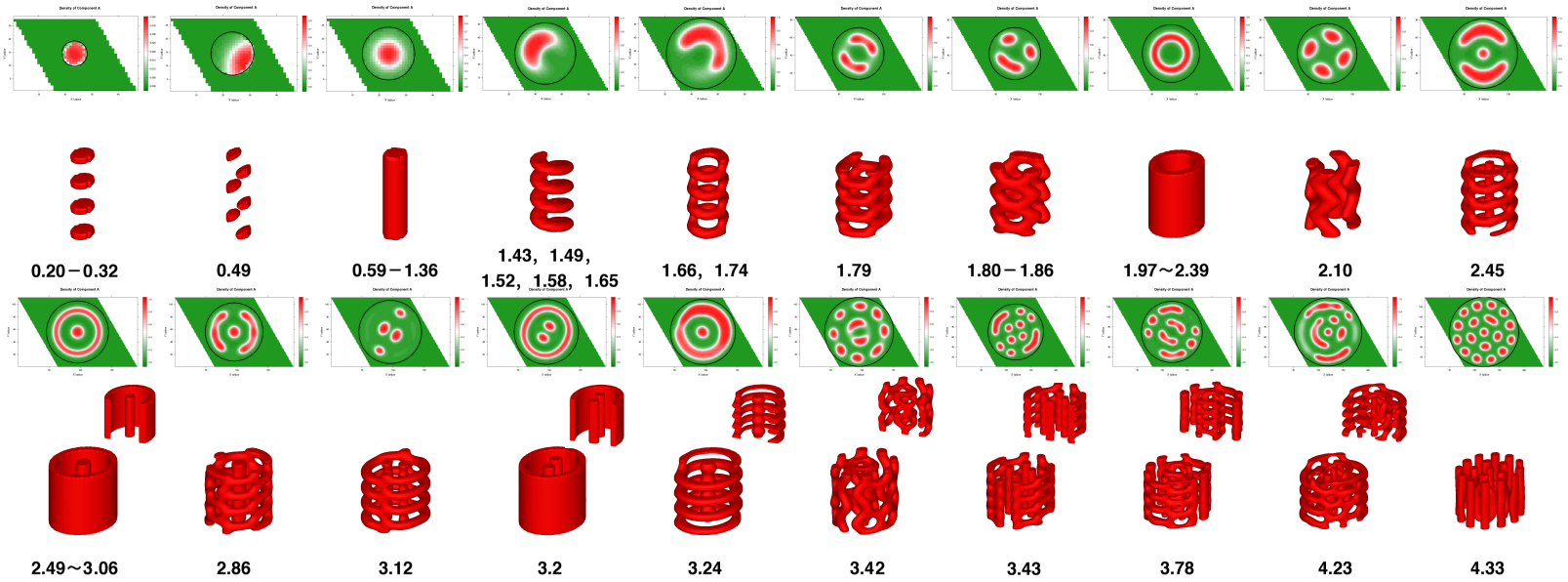

Figure 6.4: Self-assembled structures of AB block copolymer melt under cylindrical confinement with B attractive surface, as a function of D/L_0. The color scale from 0 (green) to 1(red) stands for the concentration of A block. The black circle in the 2D cut image stands for the confining circular. Only the A domain is shown in the 3D image. Some cut views are shown for clarity of multilayer structure.

of confinement of $D/L_0 = 0.20 - 0.32$, stacked discs of A domain arrange along the axis of the cylindrical pore. As the cylindrical pore diameter keeps increasing, zigzag arranged dots show up at $D/L_0 = 0.49$. When the pore diameter keeps increasing to 0.59 D/L_0, a single rod shows up and stables until $D/L_0 = 1.36$. The single helix structure shows up at $D/L_0 = 1.43, 1.49, 1.52, 1.58 and 1.65$ which is very close to the most incommensurate D and L_0 (half-integer D/L_0value). Other single layer structure such as connected toroids ($D/L_0 = 1.66, 1.74$), perforated cylinders ($D/L_0 = 1.79$), isolated perforated pieces ($D/L_0 = 1.80 - 1.86$), cylinders ($D/L_0 = 1.97$ 2.39) and curved rods ($D/L_0 = 2.10$) are observed as the confining pore diameter increase. At $D/L_0 = 2.45$, a second inner layer starts to show up. The second layer starts from one single rod at the center at $D/L_0 = 2.45$, increase to two rods then finally up to four rods before a third layer show up at $D/L_0 = 4.23$. The outer layer can either be connected donuts (for example $D/L_0 = 2.45, 3.12, 3.24$), perforated cylinders (for example $D/L_0 = 2.86, 3.42, 3.43, 3.78, 4.23$) or cylinders (for example $D/L_0 = 2.49$ 3.06). When D/L_0 increase to 4.325, cylinders along the pore axis are observed. The above simulation results indicate that if the confining diameter is too small to include one cylinder of A domain, discontinue phases of A domain is usually formed. And when the pore diameter is comparable with L_0, novel structures including helices, toroids, perforated walls is formed instead of the bulk hexagonal packed cylinders. At low incommensurate condition, for example, $D/L_0 = 1.00, 2.10$, rods or curved rods whose structures similar to the parent BCP bulk phase is observed. While at the high incommensurate condition, such as D/L_0 around 1.5, very complex structure like helices are formed under severe geometry frustration.

The absolute values of D/L_0 for experimental observed single helices (D/L_0=2.37, 2.74, 3.41, 4.23, 4.92) and simulated single helices (D/L_0=1.43, 1.49, 1.52, 1.58 and 1.65) are not in a good agreement. This disagreement is due to the fact that the simulation is of AB diblock melt, instead of ABA-silica sol precursor complex system. The interactions of between each block of BCP and the various inorganic components in Sol precursor are ignored. However, the general trend of the morphology evolution agree between experimental and simulation

work: the characteristic morphology for the high incommensurate condition is helix/toroid and increasing D/L_0 leads to increasing layers.

6.2.2 Equilibrium Period Control of Cylinder-forming Mesoporous Silica System

The expected single helix is mainly a result of the frustration degree (characterized by D/L_0), the interaction between the PAA pore wall and structure guiding BCP which is very hard to control in the experiment, and the BCP chain structure. Therefore, the bulk period L_0 of structure guiding BCP-silica bulk period in the Sol-gel process is the key parameter to enlarge the size of the single helix resulted from phase separation of BCP under cylindrical confinement. In the following section, I will discuss how to enlarge the guiding BCP-silica microphase period by five key design guidelines: (1) adjusting the volume ratio between the BCP and other inorganic components of the Sol-gel precursor; (2) adjusting the volume ratio of EO/PO block and the total molecular weight of the pluronic BCP; (3) swelling the BCP-silica system by small organic molecule trimethyl-1,3,5 benzene (TMB) at room temperature and at elevated temperature of 80 °C; (4) blending the main BCP P123 with other two types of Pluronic BCP (L121 and F127); and (5) blending the the main BCP P123 with the hydrophobic PO homopolymer of different molecular weights.

Ordered GISAX pattern of P123-silica composite thin film are shown in Fig.6.5. The volume fraction ϕ (ϕ is defined as $\phi = V_{pol}/(V_{pol}+V_{inorg}) = m_{Si(OH)_4}/\rho_{Si(OH)_4}+m_{HCl}/\rho_{HCl} \approx m_{SiO_2}/\rho_{SiO_2} + m_{H_2O}/\rho_{H_2O} + m_{HCl}/\rho_{HCl}$ [158]) of the P123 in the nonvolatile component of the precursor solution is chosen to be 0.44 (Sol2), 0.49 (Sol3), and 0.53 (Sol4) to ensure that the precursor generate hexagonal packed cylinder phase without confinement. All of the GISAX patterns are in good agreement with NANOCELL simulated pattern of c2mm with (01) direction oriented perpendicular to the film plane. The existence of the second or third order diffracted spots shows that the P123-silica thin film is highly ordered.As the volume fraction of P123 in the precursor solution increase from 0.44 (Sol2), 0.46 (Sol1), 0.49 (Sol3) to 0.53 (Sol4), the 'a' axis simulated by NANOCELL is 12.8 nm, 13.3 nm 13.4 nm and 13. 4 nm respectively. The 'b' length is around 10 nm which is much shorter than the other

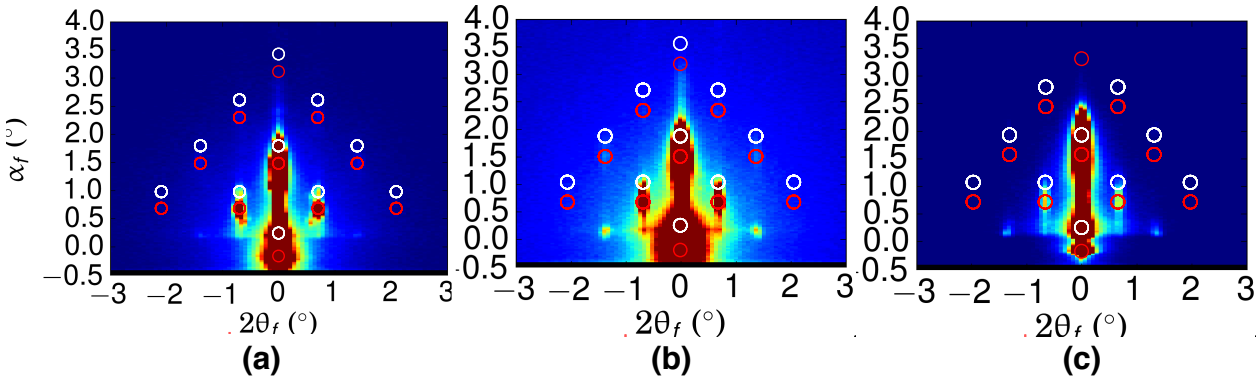

Figure 6.5: GISAXS patterns of the P123-silica composite thin film on glass slide with a and c axis parallel to the substrate surface. The overly is the simulated c2mm structure by NANOCELL.(a) synthesized by Sol2 with overlay c2mm a=12.8 nm, b=10.9 nm (b) synthesized by Sol3 with overlay c2mm a=13.4 nm, b= 10.9 nm (c) synthesized by Sol4 with overlay c2mm a=13.4 nm, b= 10.1 nm. This set of samples are aged in ambient for 60 days before GISAX measurement.

GISAX data in this session. This is caused by the extended aging time in ambient, causing more contraction of P123-silica thin film in the film thickness direction. The above GISAX result indicates that at the hexagonal cylinder forming region of P123-silica composite (ϕ is between 0.44 to 0.53), the change of volume fraction of structure guiding BCP does not affect the lattice constant very much.

2D GISAX patterns of BCP-silica thin film synthesized by other types of Pluronic BCPs besides P123 are shown in Fig. 6.6. Sharp diffraction spots are observed for BCP-silica thin films synthesized from L121, L92 and P103 BCPs. The EO/PO ratio for these BCPs are in the range between 0.15 and 0.4, which is in good agreement with Zhao's [126] findings that at moderate EO/PO ratio between 0.07 and 1.5, the resulted symmetry of the BCP-silica system favors p6mm symmetry. Although EO/PO ratio of L101 is also within this range, an ordered p6mm phase was not observed. It might result from the small EO ratios in the L101 BCP, favors unstable composite with layered structures [159].The diffused Debye rings observed from P105 and F127 guided composite film indicates that disordered structures are formed under the current synthesis condition. NANOCELL simulated lattice parameter 'a'

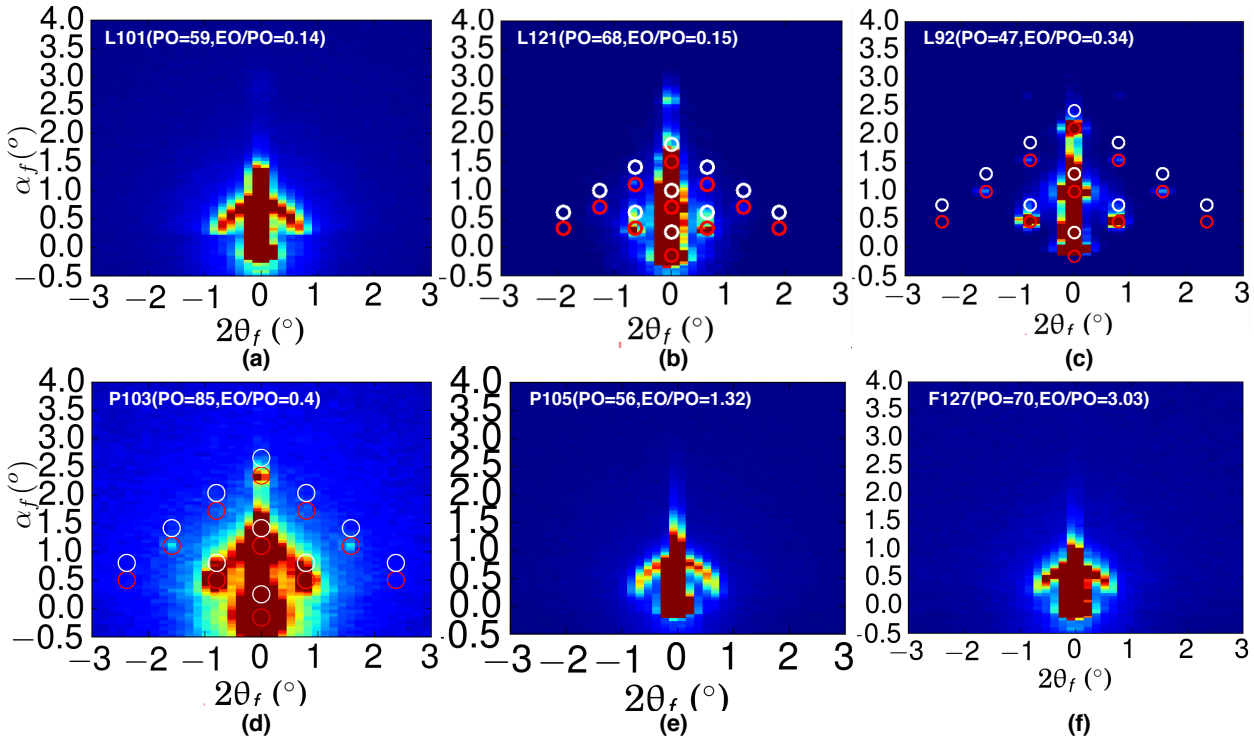

Figure 6.6: GISAXS patterns of the Pluronic BCP-silica composite thin film on glass slide with a and c axis parallel to the substrate surface. The overly is the simulated c2mm structure by NANOCELL.(a) synthesized by triblock copolymer L101 (Sol5) as structure guiding reagent (b) synthesized by L121 (Sol6) as structure guiding reagent with overlay c2mm a=14.0 nm, c=21.7 nm (c) synthesized by L92 (Sol7) as structure guiding reagent with overlay c2mm a=11.5 nm, b=16.0 nm (d) synthesized by P103 (Sol8) as structure guiding reagent with overlay c2mm a=11.2 nm, b=14.2 nm (e) synthesized by P105 (Sol9) and (d) synthesized by F127 (Sol10).

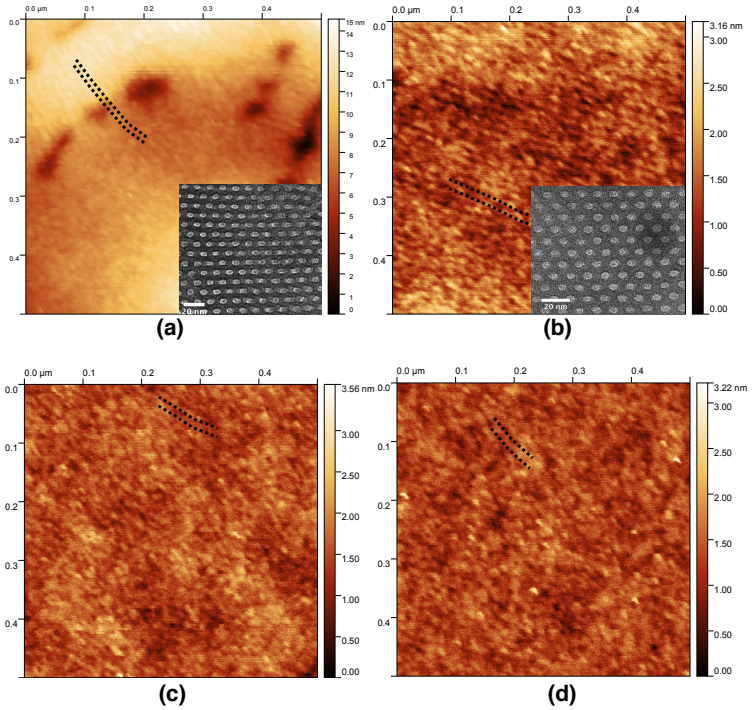

Figure 6.7: AFM plan view of P123-silica thin film swelled by TMB on glass slide (a) (b) (c) (d) are the composite film swelled by 0.5 wt.% TMB/P123 (Sol11), 1 wt.% TMB/P123 (Sol12), 1.5 wt.% TMB/P123 (Sol13) and 2 wt.% TMB/P123 (Sol14). The inset in (a) and (b) is TEM cross sectional view of the composite film (The scale bar is 20 nm). The black dotted line are guide for the eyes.

for L121, L92 and P103 are 14.0 nm, 11.5 nm, and 11.2 nm, respectively. Among them, L121 might guide the single layer morphologies under a larger PAA diameter than P123.

It is well known that the period and the pore size of the cylindrical forming P123-silica bulk composite can be enlarged by adding cosolvent organic molecules, such as 1,3,5-trimethylbenzen (TMB). When the weight ratio of TMB to P123 increase to 2, the lattice parameter a is reported to be 37 nm for the bulk P123-silica composite [126, 160]. TMB is used as the swelling agent for our synthesis of P123-silica thin film by dip coating. Fig. 6.7 shows the AFM plane view of the TMB swelled P123-silica ranging from 0.5 wt.% TMB/P123 to 2 wt.% TMB/P123. The distances between adjacent parallel cylinders from AFM image

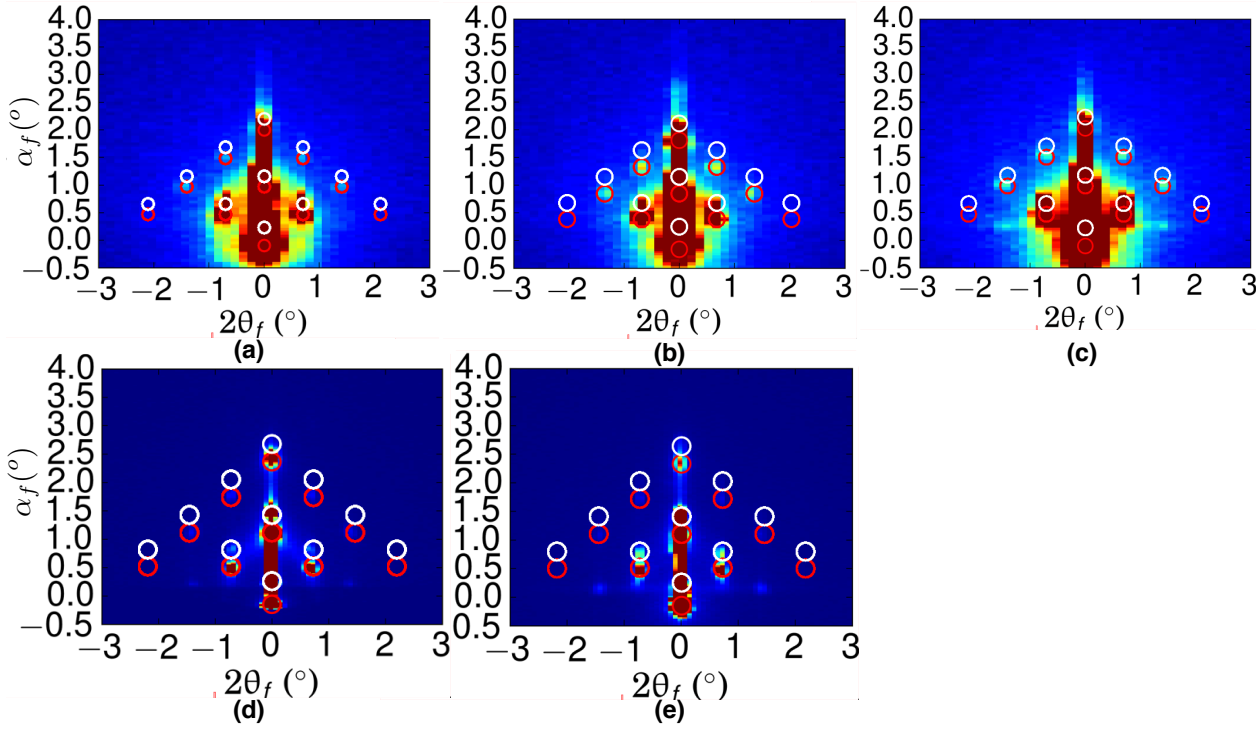

Figure 6.8: GISAXS patterns of the P123-silica composite thin film with TMB as swelling agent on glass slide with a and c axis parallel to the substrate surface at elevated temperature. The overly is the simulated c2mm structure by NANOCELL.(a) as-synthesized composite thin film by Sol1 with overlay c2mm a=12.8 nm, b=17.2 nm (b) as-synthesized composite thin film by adding 0.5 wt.%TMB/P123 (Sol11) with overlay c2mm a=13.1 nm, b=18.2 nm (c) as-synthesized composite thin film by adding 2 wt.%TMB/P123 (Sol14) with overlay c2mm a=12.7nm, b=16.9 nm (d) calcinated composite thin film by Sol1 with overlay c2mm a=12.2 nm, b=14.2 nm (e) calcinated composite thin film by adding 2 wt.%TMB/P123 (Sol14) with overlay c2mm a=12.1nm, b=14.2 nm. This set of samples are prepared at a mixing temperature of 45 °C and aging temperature of 80 °C.

are 11.5 nm, 11.6 nm, 12.7 nm and 12.8 nm for 0.5 wt.% TMB/P123 ,1 wt.% TMB/P123 , 1.5 wt.% TMB/P123 and 2 wt.% TMB/P123 , respectively. The lattice parameter 'a' measured from TEM is slightly larger than the data from AFM. They are 12.23 nm and 12.47 nm for 0.5 wt.% TMB/P123 and 1 wt.% TMB/P123. These data show that the adding cosolvent TMB does not expand the period of the P123-silica thin film prepared by dip-coating as in the bulk case. We conducted the TMB swelling experiments with a higher mixing (45 °C) and aging temperature (80 °C) to ensure the complete cooperation between cosolvent and the amphiphilic P123. The 2D GISAX pattern in Fig. 6.8 (a) (b) and (c) show the as-synthesized P123-silica thin film swelled by 0 wt.% TMB/P123, 0.5 wt.% TMB/P123 and 2 wt.% TMB/P123 respectively. According to the simulated overlay of c2mm symmetry, the 'a' lattice parameters are 12.8 nm, 13.1 nm and 12.7 nm as the weight percentage of TMB increase from 0 to 2 , showing no sign of increasing. And the 'a' lattice parameter of calcinated P123-silica thin film swelled by 2 wt.% TMB/P123 12.1 nm is indistinguishable with the one synthesized without any TMB addition. Compared to the as-synthesized composite thin film, calcination caused the shrink of c2mm lattice unit cell, mainly in the b film thickness direction. In our experiment, the BCP-silica thin film is formed by evaporation induced self-assembly (EISA). Upon the solvent evaporation, the surfactant and silica precursors co-self-assemble into the ordered mesostructure of cylinders after the concentration pass the critical micelle concentration during the dip-coating process. However, the volatile TMB might evaporate off during the dip-coating process and de-swell the P123-silica composite, inhibiting the expansion of the P123-silica period.

Swelling P123-silica composite by non-volatile molecules was conducted. The effect of blending P123 with other Pluronic polymers are shown in Fig. 6.9. The GISAX data show that the highly ordered c2mm symmetry is retained when the added second pluronic polymer weight percentage is less than 0.5 for both L121 and F127. As the amount of L121 increases from 0.1 wt.% L121/P123 to 0.25 wt.% L121/P123, the lattice parameter 'a' increase from 13.5 nm to 15.3 nm. As the L121 amount increase up to 0.5 wt.% L121/P123, the diffused Debye ring shows a disordered structure. By adding F127 to the original Sol precursor, the

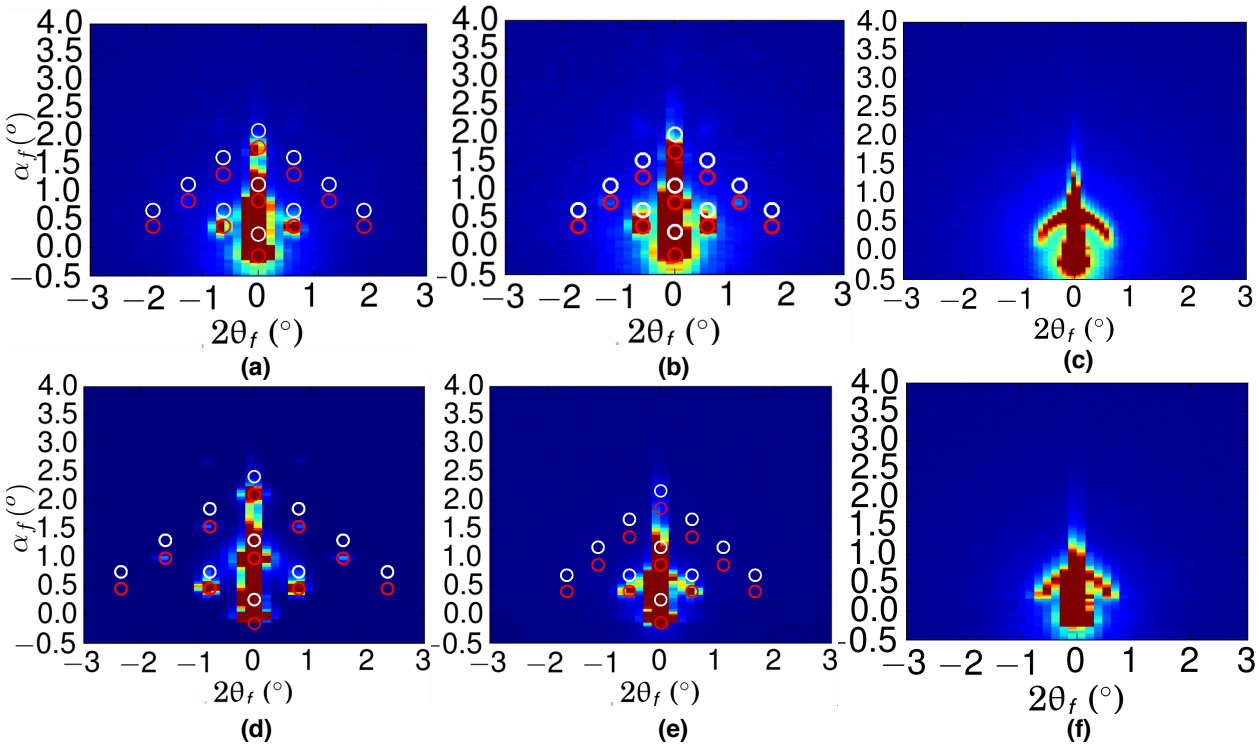

Figure 6.9: GISAXS patterns of the P123-silica composite blended with L121/F127 thin film on glass slide with a and c axis parallel to the substrate surface. The overly is the simulated c2mm structure by NANOCELL.(a) (b) (c) show the as-synthesized composite thin film from 0.1 wt.% L121/P123 (Sol15) with overlay of c2mm (a=13.5 nm, b=17.6 nm), 0.25 wt.% L121/P123 (Sol16) with overlay of c2mm (a=15.3 nm, b=19.3 nm) and 0.5 wt.% L121/P123 (Sol17), respectivley. and (d) (e) (f) show the result of as-synthesized composite thin film from 0.1 wt.% F127/P123 (Sol18) with overlay of c2mm (a=13.9 nm, b=18.8 nm), 0.25 wt.% F127/P123 (Sol19) with overlay of c2mm (a=15.9 nm, b=17.6 nm) and 0.5 wt.% F127/P123 (Sol20), respectivley.

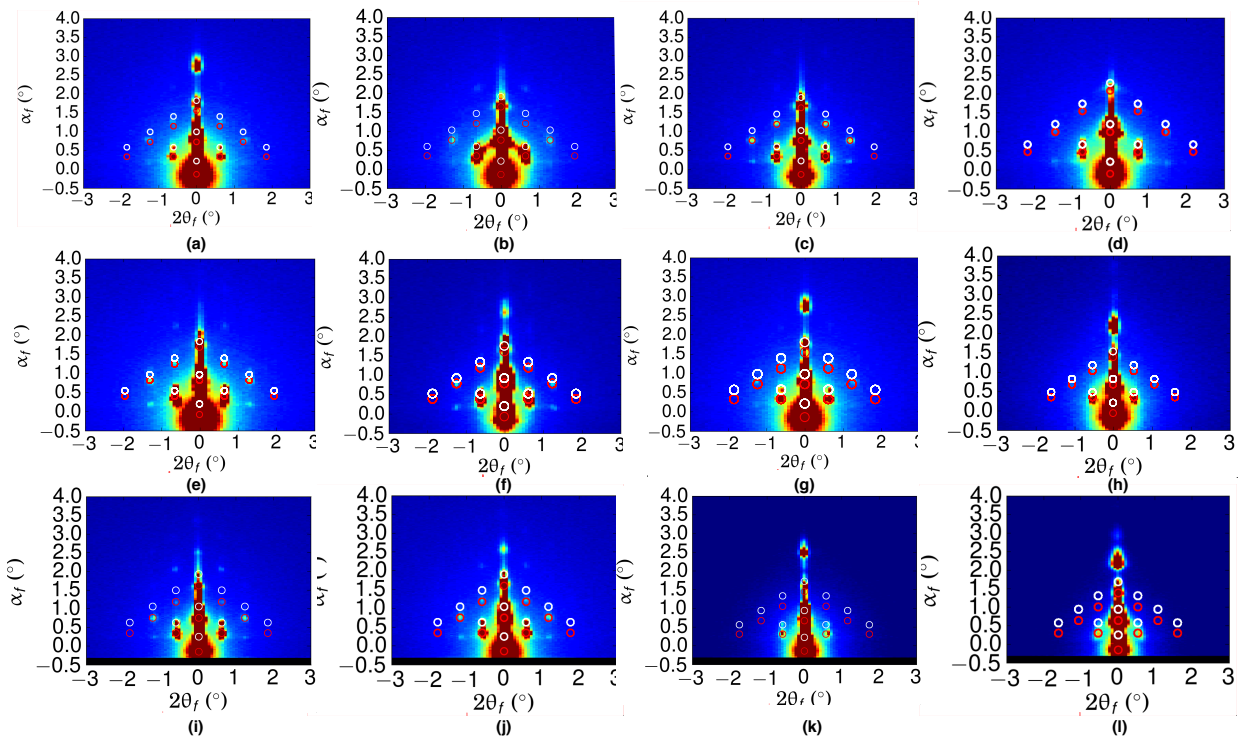

Figure 6.10: GISAXS patterns of the P123-silica composite blended with PPO homopolymer of various molecular weight thin film on glass slide with a and c axis parallel to the substrate surface. The overly is the simulated c2mm structure by NANOCELL. (a) (b) (c) (d) show the as-synthesized composite thin film from sol blended with 0.1 wt.% PPO400/P123 with overlay of c2mm (a=12.9 nm, b=17.1 nm), 0.2 wt.% PPO400/P123 with overlay of c2mm (a=13.6 nm, b=19.9 nm), 0.3 wt.% PPO400/P123 with overlay of c2mm (a=13.8 nm, b=20.3 nm) and 0.5 wt.% PPO400/P123 with overlay of c2mm (a=12.5 nm, b=16.0 nm). (e) (f) (g) (h) show the as-synthesized composite thin film from sol blended with 0.1 wt.% PPO1000/P123 with overlay of c2mm (a=13.8 nm, b=20.5 nm), 0.2 wt.% PPO1000/P123 with overlay of c2mm (a=14.2 nm, b=21.0 nm), 0.3 wt.% PPO1000/P123 with overlay of c2mm (a=14.4 nm, b=21.1nm) and 0.5 wt.% PPO1000/P123 with overlay of c2mm (a=16.5 nm, b=24.5 nm) (i) (j) (k) (l) show the as-synthesized composite thin film from sol blended with 0.1 wt.% PPO3000/P123 with overlay of c2mm (a=14.2 nm, b=20.0 nm), 0.2 wt.% PPO3000/P123 with overlay of c2mm (a=14.8 nm, b=20.1 nm), 0.3 wt.% PPO3000/P123 with overlay of c2mm (a=13.6 nm, b=20.0 nm) and 0.5 wt.% PPO3000/P123 with overlay of c2mm (a=16.3 nm, b=23.0 nm).

lattice parameter 'a' increases from 13.9 nm to 15.9 nm at 0.1 wt.%F127/P123 and 0.25 wt.% F127/P123. It shows that blending Pluronic polymers together can effectively expand the lattice parameter up to 15.9 nm. Fig.6.10 shows the 2D GISAX patterns of P123-silica blended with PPO400, PPO1000 and PPO3000 at various weight fraction of 0.1, 0.2, 0.3 and 0.5 PPO/P123. For P123-silica composite thin film blended with PPO400, the lattice parameter 'a' change from 12.9 nm, 13.6 nm, 13.8 nm to 12.5 nm as the weight fraction of PPO400 increase (Fig. 6.10 (a) to (d)). For PPO1000 case, the lattice parameter 'a' increase from 13.8 nm, 14.2 nm, 14.4 nm to 16.5 nm when the PPO1000 amount increases. And for the PPO3000 case, the lattice parameter change from 14.2 nm, 14.8 nm, 13.6 nm to 16.3 nm. The general trend is that for PPO of the same molecular weight, the resulted mesostructure period increases with increasing PPO amount (except the cases of 0.5 PPO400/P123 and 0.3 PPO1000/P123). And the swelling effect of PPO increase with increasing molecular weight. The lattice parameter 'a' can be expanded to up to 16.5 nm by blending P123 with 0.5 wt. % PPO1000 compared to the original 13.3 nm (Sol1). Further experiments using such mixture of polymers as the structure guiding agent to synthesize *Fe-Pd* single helices with larger diameter is suggested as the future work.

6.3 Conclusion

Fe-Pd nanowires with various morphologies are synthesized by P123-silica co-self-assembly under PAA cylindrical confinement. A self-consistent field theory simulation of AB block copolymer melt under cylindrical confinement is conducted aiding the prediction of mesostructure evolution. Single helices are found to be the result of high degree of confinement and high incommensurate between D and L_0. The *Fe-Pd* single helices with P123 as structure guiding agent are observed at D/L_0= 2.37, 2.74, 3.41, 4.23 and 4.92. And the simulation of the AB block copolymer melt ($f_a = 0.3, \chi N = 20$) shows the single helices at D/L_0 between 1.43 and 1.65. The effect of P123-silica sol precursor solution concentration, poloxamer types, addition of volatile organic molecule TMB and non-volatile L121, F127, PPO400, PPO1000 and PPO3000 on the lattice parameter 'a' of the resulted c2mm BCPs-silica thin

film are studied. The lattice parameter a can be expanded up to 16.5 nm when blending 0.5 PPO1000/P123.

Chapter 7

SUMMARY AND FUTURE WORK

In the presented work, $Fe_{70}Pd_{30}$ nanohelices were synthesized using $PAA-SiO_2$ hybrid template by electrochemical deposition. Spatial- and single helices length-wise chemical composition can be precisely controlled. This method is not material specific, and can be applied to generate all kinds of metals, semiconductors, oxides, and polymers that can be electrodeposited. $Fe_{70}Pd_{30}$ nanorods were synthesized using porous anodic alumina (PAA) template with the same electrodeposition methods.

The as-deposited $Fe_{70}Pd_{30}$ nanowires (both nanorods and nanohelices) exhibit mixed face-centered cubic (fcc) and body-centered cubic (bcc) phases. When annealed above 720 °C in $Ar/5\%H_2$ for over 1 min followed by rapid cooling, single fcc austenite phase is obtained. For $Fe_{70}Pd_{30}$ nanorods (original size is 65 nm in diameter and 1 µm in length) annealed without PAA template, which causes agglomeration with size up to 700 nm, reversible thermal elastic phase transformation was observed by temperature change *in situ* X-ray diffraction (XRD), and the martensite starting temperature is found to be -40 °C. For $Fe_{70}Pd_{30}$ nanorods annealed in PAA template with well-defined shape (65 nm in diameter and 1 µm in length), an austenite peak weakening was observed by XRD at -160 °C, suggesting a martensite starting temperature below -160 °C . For $Fe_{70}Pd_{30}$ nanohelices annealed in $PAA-SiO_2$ hybrid template, martensite transformation was not observed between room temperature and -160 °C. The decrease of martensite phase starting temperature is caused by the decrease of the grain size in nanoscale.

The shape evolution of *Fe-Pd* nanowires synthesized by P123-silica co-self-assembly under cylindrical confinement was investigated by transmission electron microscope (TEM). Single helices are experimentally found at different confining degree of D/L_0= 2.37, 2.74,

3.41, 4.23 and 4.92, where D is the confining pore diameter and L_0 is the equilibrium length of the structure guiding block copolymer in its bulk phase. A simplified asymmetric AB block copolymer (BCP) melt under cylindrical confinement with major block-attracting wall was simulated by self-consistent field theory. For AB block polymer melt with $f_a = 0.3, \chi N = 20$, single helices are formed at D/L_0=1.43, 1.49, 1.52, 1.58 and 1.65. Both the experiment and simulation result show that single helices mainly form at a high degree of confinement condition. Therefore, single helix with larger loop diameter can be produced with BCP with larger equilibrium length. The effect of various methods, including changing Sol precursor solution concentration, changing BCP type, blending with small organic molecules, blending with different BCP and blending with homopolymer, on the equilibrium length of current cylinder forming P123 were investigated. Blending with other poloxamer and homopolymer PPO with P123 are found effective to enlarge L_0.

Future work may consider fabricating $Fe_{70}Pd_{30}$ single helices with larger outer diameter and wire diameter to test the size limitation of shape memory effect. To realize this, one should consider polymerization of BCP with larger molecular weight to be used as the structure guiding polymer in Sol precursor solution. The accuracy of the self-consistent field theory simulation can be improved by modifying the current simple AB BCP melt system to ABA BCP-solvent-inorganic components (standing for the various components in the Sol precursor solution with different affinity to A and B blocks) system.

BIBLIOGRAPHY

[1] Sunyong Hwang, Hyunah Kwon, Sameer Chhajed, Ji Won Byon, Jeong Min Baik, Jiseong Im, Sang Ho Oh, Ho Won Jang, Seok Jin Yoon, Jong Kyu Kim, and Advanced Materials Engineering. "TiO 2 Nanohelix Gas Sensors with Enhanced Performance and Potential Application as a Building Block of Electronic Noses". In: (2012), pp. 1626–1628.

[2] Jae Hwang Lee, Jonathan P. Singer, and Edwin L. Thomas. "Micro-/nanostructured mechanical metamaterials". In: *Advanced Materials* 24.36 (2012), pp. 4782–4810.

[3] Mikhail Lapine, Ilya V. Shadrivov, David A. Powell, and Yuri S. Kivshar. "Magnetoelastic metamaterials". In: *Nature Materials* 11.1 (2012), pp. 30–33.

[4] Robert A. Freitas. "Nanotechnology, nanomedicine and nanosurgery". In: *International Journal of Surgery* 3.4 (2005), pp. 243–246.

[5] Adriano Cavalcanti, Bijan Shirinzadeh, Declan Murphy, and Julian A. Smith. "Nanorobots for laparoscopic cancer surgery". In: *Proceedings - 6th IEEE/ACIS International Conference on Computer and Information Science, ICIS 2007; 1st IEEE/ACIS International Workshop on e-Activity, IWEA 2007* Icis (2007), pp. 738–743.

[6] Adriano Cavalcanti, Bijan Shirinzadeh, Robert A. Freitas, and Tad Hogg. "Nanorobot architecture for medical target identification". In: *Nanotechnology* 19.1 (2008).

[7] Aristides A.G. Requicha. "Nanorobots, NEMS, and nanoassembly". In: *Proceedings of the IEEE* 91.11 (2003), pp. 1922–1933.

[8] K. L. Ekinci. "Electromechanical transducers at the nanoscale: Actuation and sensing of motion in nanoelectromechanical systems (NEMS)". In: *Small* 1.8-9 (2005), pp. 786–797.

[9] Mo Li, H. X. Tang, and M. L. Roukes. "Ultra-sensitive NEMS-based cantilevers for sensing, scanned probe and very high-frequency applications". In: *Nature Nanotechnology* 2.2 (2007), pp. 114–120.

[10] John Rogers, Yonggang Huang, Oliver G. Schmidt, and David H. Gracias. "Origami MEMS and NEMS". In: *MRS Bulletin* 41.02 (2016), pp. 123–129.

[11] Rob Legtenberg and Harrie A.C. Tilmans. "Electrostatically driven vacuum-encapsulated polysilicon resonators Part I. Design and fabrication". In: *Sensors and Actuators: A. Physical* 45.1 (1994), pp. 57–66.

[12] Charles Babbage and Charles Babbage. "Nanodevice motion at microwave frequencies". In: *Nature* 421.January (2003), pp. 496–497.

[13] Amir Rahafrooz and Siavash Pourkamali. "High-frequency thermally actuated electromechanical resonators with piezoresistive readout". In: *IEEE Transactions on Electron Devices* 58.4 (2011), pp. 1205–1214.

[14] S. C. Masmanidis, R. B. Karabalin, I. De Vlaminck, G. Borghs, M. R. Freeman, and M. L. Roukes. "Multifunctional Nanomechanical Systems via Tunably Coupled Piezoelectric Actuation". In: *Science* 317.5839 (2007), pp. 780–783.

[15] María D. Manrique-Juárez, Sylvain Rat, Lionel Salmon, Gábor Molnár, Carlos M. Quintero, Liviu Nicu, Helena J. Shepherd, and Azzedine Bousseksou. "Switchable molecule-based materials for micro- and nanoscale actuating applications: Achievements and prospects". In: *Coordination Chemistry Reviews* 308 (2016), pp. 395–408.

[16] Taishi Wada and Minoru Taya. "Spring-based actuators". In: *Proceedings of SPIE on Smart Structures and Materials 2002* 4699 (2002), pp. 294–302.

[17] J. Cui, T. W. Shield, and R. D. James. "Phase transformation and magnetic anisotropy of an iron-palladium ferromagnetic shape-memory alloy". In: *Acta Materialia* 52.1 (2004), pp. 35–47.

[18] Y. Ma, M. Zink, and S. G. Mayr. "Biocompatibility of single crystalline Fe70Pd30 ferromagnetic shape memory films". In: *Applied Physics Letters* 96.21 (2010), pp. 213703 –213703–3.

[19] Sung Min An, Junghyun Ryu, Maenghyo Cho, and Kyu Jin Cho. "Engineering design framework for a shape memory alloy coil spring actuator using a static two-state model". In: *Smart Materials and Structures* 21.5 (2012).

[20] L. C. Chang and T. A. Read. "Plastic Deformation and Diffusionless Phase Changes in Metals - The Gold-Cadmium Beta-Phase". In: *Transactions of the American Institute of Mining and Metallurgical Engineers* 191.1 (1951), pp. 47–52.

[21] W. J. Buehler, J. V. Gilfrich, and R. C. Wiley. "Effect of Low-Temperature Phase Changes on the Mechanical Properties of Alloys near Composition TiNi". In: *Journal of Applied Physics* 34.5 (1963), pp. 1475–1477.

[22] R. Stalmans, J. Van Humbeeck, and L. Delaey. "The two way memory effect in copper-based shape memory alloys - thermodynamics and mechanisms". In: *Acta Metallurgica Et Materialia* 40.11 (1992), pp. 2921–2931.

[23] J. Melorose, R. Perroy, and S. Careas. "Martensite Ordering and Stabilization in Copper Based Shape Memory Alloys". In: *Mhrials Research Bulletin,* 30.6 (1995), pp. 755–760.

[24] J. A. Shaw and S. Kyriakides. "On the nucleation and propagation of phase transformation fronts in a NiTi alloy". In: *Acta Materialia* 45.2 (1997), pp. 683–700.

[25] Yongqing Fu, Hejun Du, Weimin Huang, Sam Zhang, and Min Hu. "TiNi-based thin films in MEMS applications: A review". In: *Sensors and Actuators, A: Physical* 112.2-3 (2004), pp. 395–408.

[26] R. Kainuma, Y. Imano, W. Ito, Y. Sutou, H. Morito, S. Okamoto, O. Kitakami, K. Oikawa, A. Fujita, T. Kanomata, and K. Ishida. "Magnetic-field-induced shape recovery by reverse phase transformation". In: *Nature* 439.7079 (2006), pp. 957–960.

[27] G. D. Liu, J. L. Chen, Z. H. Liu, X. F. Dai, G. H. Wu, B. Zhang, and X. X. Zhang. "Martensitic transformation and shape memory effect in a ferromagnetic shape memory alloy: Mn2NiGa". In: *Applied Physics Letters* 87.26 (2005), pp. 1–3.

[28] R. C. O'Handley, S. J. Murray, M. Marioni, H. Nembach, and S. M. Allen. "Phenomenology of giant magnetic-field-induced strain in ferromagnetic shape-memory materials (invited)". In: *Journal of Applied Physics* 87.9 (2000), pp. 4712–4717.

[29] Tomoyuki Kakeshita and Kari Ullakko. "G iant Magnetostriction in Ferromagnetic Alloys". In: *Strain* February (2002), pp. 105–109.

[30] T.W. Duerig, K. N. Melton, D. Stockel, and C. M. Wayman. *engineering aspects of shape memory alloys*. Butterworth-Heinemann Ltd, 1990.

[31] N.B Morgan. "Medical shape memory alloy applicationsthe market and its products". In: *Materials Science and Engineering: A* 378.1-2 (2004), pp. 16–23.

[32] C.M. Wayman K.N. Melton in: K. Otsuka. *Shape Memory Materials*. Cambridge University Press, 1998.

[33] Jan Van Humbeeck. "Non-medical applications of shape memory alloys". In: *Materials Science and Engineering: A* 273-275 (1999), pp. 134–148.

[34] Yuanchang Liang, Hiroyuki Kato, and Minoru Taya. "Model calculation of 3D-phase transformation diagram of ferromagnetic shape memory alloys". In: *Mechanics of Materials* 38.5-6 (2006), pp. 564–570.

[35] M. Taya, C. Xu, T. Matsuse, and S. Muraishi. "Molecular dynamics model for nanomotions of FePd nanohelices". In: *Journal of Applied Physics* 121.15 (2017), p. 154302.

[36] Jun Cui and Tom Shield. "Ferromagnetic shape memory effects in an iron palladium alloy". In: *Journal of Mechanics of Materials and Structures* 2.3 (2007), pp. 505–528.

[37] A. Sozinov, A. A. Likhachev, and Kari Ullakko. "Crystal structures and magnetic anisotropy properties of Ni-Mn-Ga martensitic phases with giant magnetic-field-induced strain". In: *IEEE Transactions on Magnetics* 38.5 I (2002), pp. 2814–2816.

[38] M. Wuttig and R. D. James. "Magnetostriction of martensite". In: *Philosophical Magazine A* 77.5 (1998), pp. 1273–1299.

[39] E Denkhaus and K Salnikow. "Nickel essentiality, toxicity, and carcinogenicity". In: *Critical Reviews in Oncology/Hematology* 42.1 (2002), pp. 35–56.

[40] U. Allenstein, Y. Ma, A. Arabi-Hashemi, M. Zink, and S. G. Mayr. "Fe-Pd based ferromagnetic shape memory actuators for medical applications: Biocompatibility, effect of surface roughness and protein coatings". In: *Acta Biomaterialia* 9.3 (2013), pp. 5845–5853.

[41] Kirsten M. Pondman, Nathan D. Bunt, A. Wouter Maijenburg, Richard J A Van Wezel, Uday Kishore, Leon Abelmann, Johan E. Ten Elshof, and Bennie Ten Haken. "Magnetic drug delivery with FePd nanowires". In: *Journal of Magnetism and Magnetic Materials* 380 (2015), pp. 299–306.

[42] Thaddeus B. Massalki. "Binary Alloy Phase Diagrams". In: (1990).

[43] Masaaki Matsui, Hajime Yamada, and Kengo Adachi. *NEW LOW TEMPERATURE PHASE (FCT) OF Fe-Pd INVAR.* 1980.

[44] Eiji Yashima, Katsuhiro Maeda, Hiroki Iida, Yoshio Furusho, and Kanji Nagai. "Helical polymers: synthesis, structures, and functions." In: *Chemical reviews* 109.11 (2009), pp. 6102–211.

[45] Yeo-Wan Chiang, Rong-Ming Ho, Christian Burger, and Hirokazu Hasegawa. "Helical assemblies from chiral block copolymers". In: *Soft Matter* 7.21 (2011), p. 9797.

[46] K. Robbie, M. J. Brett, and A. Lakhtakia. *Chiral sculptured thin films.* 1996.

[47] K. Robbie. "Sculptured thin films and glancing angle deposition: Growth mechanics and applications". In: *Journal of Vacuum Science and Technology A: Vacuum, Surfaces, and Films* 15.3 (1997), p. 1460.

[48] Sunyong Hwang, Hyunah Kwon, Sameer Chhajed, Ji Won Byon, Jeong Min Baik, Jiseong Im, Sang Ho Oh, Ho Won Jang, Seok Jin Yoon, and Jong Kyu Kim. "A near single crystalline TiO ₂ nanohelix array: enhanced gas sensing performance and its application as a monolithically integrated electronic nose". In: *The Analyst* 138.2 (2013), pp. 443–450.

[49] Andrew G Mark, John G Gibbs, Tung-Chun Lee, and Peer Fischer. "Hybrid nanocolloids with programmed three-dimensional shape and material composition." In: *Nature materials* 12.9 (2013), pp. 802–7.

[50] Dominik J Bell, Lixin Dong, Bradley J Nelson, Matthias Golling, Li Zhang, and Detlev Grützmacher. "Fabrication and characterization of three-dimensional InGaAs/GaAs nanosprings." In: *Nano letters* 6.4 (2006), pp. 725–9.

[51] Zheng Ren and Pu-Xian Gao. "A review of helical nanostructures: growth theories, synthesis strategies and properties." In: *Nanoscale* 6.16 (2014), pp. 9366–400.

[52] L Zhang, E Deckhardt, a Weber, C Schönenberger, and D Grützmacher. "Controllable fabrication of SiGe/Si and SiGe/Si/Cr helical nanobelts". In: *Nanotechnology* 16.6 (2005), pp. 655–663.

[53] Li Zhang, Lixin Dong, Dominik J. Bell, Bradley J. Nelson, Christian Schönenberger, and Detlev Grützmacher. "Fabrication and characterization of freestanding Si/Cr micro- and nanospirals". In: *Microelectronic Engineering* 83.4-9 (2006), pp. 1237–1240.

[54] Xiang Yang Kong and Zhong Lin Wang. "Spontaneous Polarization-Induced Nanohelixes, Nanosprings, and Nanorings of Piezoelectric Nanobelts". In: *Nano Letters* 3.12 (2003), pp. 1625–1631.

[55] Rusen Yang, Yong Ding, and Lin Wang Zhong. "Deformation-free single-crystal nanohelixes of polar nanowires". In: *Nano Letters* 4.7 (2004), pp. 1309–1312.

[56] Guoqing Chang, Guoxia Song, Jian Yang, Runsheng Huang, Alina Kozinda, and Jianyi Shen. "Morphology control of nanohelix by electrospinning". In: *Applied Physics Letters* 101.26 (2012), pp. 1–4.

[57] Yiying Wu and Guosheng Chengand Kirill Katsovand Scott W Sidesand Jianfang Wangand Jing Tangand Glenn H Fredricksonand Martin Moskovitsand Galen DStucky. "Composite mesostructures by nano-confinement." In: *Nature materials* 3.11 (2004), pp. 816–22.

[58] Justyna K Gansel, Michael Thiel, Michael S Rill, Manuel Decker, Klaus Bade, Volker Saile, Georg Von Freymann, Stefan Linden, and Martin Wegener. "Gold Helix Photonic Metamaterial as". In: 325.September (2009), pp. 1513–1516.

[59] Lichun Liu, Sang Hoon Yoo, Sang a. Lee, and Sungho Park. "Wet-chemical synthesis of palladium nanosprings". In: *Nano Letters* 11 (2011), pp. 3979–3982.

[60] Chun-long Chen, Peijun Zhang, and Nathaniel L Rosi. "A New Peptide-Based Method for the Design and Synthesis of Nanoparticle Superstructures : Construction of Highly Ordered Gold Nanoparticle Double Helices". In: (2008), pp. 13555–13557.

[61] Cong-Yan Chen, Hong-Xin Li, and Mark E. Davis. "Studies on mesoporous materials". In: *Microporous Materials* 2.1 (1993), pp. 17–26.

[62] D Gangardt. "Letters To Nature". In: *Nature* 429.MAY (2004), pp. 281–285.

[63] Stephen A Bagshaw, Eric Prouzet, Thomas J Pinnavaia, Stephen A Bagshaw, Eric Prouzet, and Thomas J Pinnavaiat. "Templating of Mesoporous Molecular Sieves by Nonionic Polyethylene Oxide Surfactants Published by : American Association for the Advancement of Science Stable URL : http://www.jstor.org/stable/2888004 Templating of Mesoporous Molecular Sieves by Nonionic ". In: 269 (1995), pp. 1242–1244.

[64] Priyanka Dobriyal, Hongqi Xiang, Matsunaga Kazuyuki, Jiun Tai Chen, Hiroshi Jinnai, and Thomas P. Russell. "Cylindrically confined diblock copolymers". In: *Macromolecules* 42.22 (2009), pp. 9082–9088.

[65] Bin Yu, Pingchuan Sun, Tiehong Chen, Qinghua Jin, Datong Ding, Baohui Li, Anchang Shi, and Bin Yu. "Self-assembled morphologies of diblock copolymers confined in nanochannels : Effects of confinement geometry Self-assembled morphologies of diblock copolymers confined in nanochannels : Effects of confinement geometry". In: 204903 (2007).

[66] Peng Chen, Haojun Liang, and An-chang Shi. "Origin of Microstructures from Confined Asymmetric Diblock Copolymers". In: (2007), pp. 7329–7335.

[67] Weihua Li and Robert A. Wickham. "Influence of the surface field on the self-assembly of a diblock copolymer melt confined in a cylindrical nanopore". In: *Macromolecules* 42.19 (2009), pp. 7530–7536.

[68] Su-mi Hur, Carlos J Garc, Edward J Kramer, and Glenn H Fredrickson. "SCFT Simulations of Thin Film Blends of Block Copolymer and Homopolymer Laterally Confined in a Square Well". In: (2009), pp. 5861–5872. DOI: 10.1021/ma900519r.

[69] Bo Lin, Hongdong Zhang, Feng Qiu, and Yuliang Yang. "Self-assembly of ABC star triblock copolymer thin films confined with a preferential surface: A self-consistent mean field theory". In: *Langmuir* 26.24 (2010), pp. 19033–19044.

[70] Yuci Xu, Nan Xie, Weihua Li, Feng Qiu, and An Chang Shi. "Phase behaviors and ordering dynamics of diblock copolymer self-assembly directed by lateral hexagonal confinement". In: *Journal of Chemical Physics* 137.19 (2012).

[71] Meijiao Liu, Weihua Li, Feng Qiu, Meijiao Liu, Weihua Li, and Feng Qiu. "Segmented helical structures formed by ABC star copolymers in nanopores Segmented helical structures formed by ABC star copolymers in nanopores". In: 104904 (2013).

[72] Nabil Laachi, Kris T. Delaney, Bongkeun Kim, Su Mi Hur, Robert Bristol, David Shykind, Corey J. Weinheimer, and Glenn H. Fredrickson. "Self-consistent field theory investigation of directed self-assembly in cylindrical confinement". In: *Journal of Polymer Science, Part B: Polymer Physics* 53.2 (2015), pp. 142–153.

[73] Yixin Liu. "Polyorder [source code]". In: (2014). URL: `https://bitbucket.org/liuyxpp/polyorder`.

[74] W. M. Latimer. "the oxidation states of the elements and their potentials in aqueous solution". In: (1952).

[75] Brenner. A. "Electrodeposition of alloys principles and practice volume I". In: (p.49).

[76] T. C. Franklin. "Some mechanisms of action of additives in electrodeposition processes". In: *Surface and Coatings Technology* 30.4 (1987), pp. 415–428.

[77] P. JUZIKIS, M. U. KITTEL, and C. J. RAUB. "Electrolytic deposition of palladium-iron alloys". In: *Plating and surface finishing* 81.8 (), pp. 59–62.

[78] M.E. Baumgaertner. "The electrodepositon of palladium-iron alloys". In: *dissertaion* (1998).

[79] Sayaka Doi, Feng Wang, Kaori Hosoiri, and Tohru Watanabe. "Preparation and Characterization of Electrodeposited Fe Pd Binary Alloy Film". In: 44.4 (2003), pp. 649–652.

[80] S. C. Hernández, B. Y. Yoo, E. Stefanescu, S. Khizroev, and N. V. Myung. "Electrodeposition of iron-palladium thin films". In: *Electrochimica Acta* 53 (2008), pp. 5621–5627.

[81] X.L. Fei, S.L. Tang, R.L. Wang, H.L. Su, and Y.W. Du. "Fabrication and magnetic properties of FePd nanowire arrays". In: *Solid State Communications* 141.1 (2007), pp. 25–28.

[82] V. Haehnel, S. Fähler, L. Schultz, and H. Schlörb. "Electrodeposition of Fe70Pd30 nanowires from a complexed ammoniumsulfosalicylic electrolyte with high stability". In: *Electrochemistry Communications* 12.8 (2010), pp. 1116–1119.

[83] Byungjun Jeon, Sanghwa Yoon, and Bongyoung Yoo. "Electrochemical synthesis of compositionally modulated FexPd1x nanowires". In: *Electrochimica Acta* 56.1 (2010), pp. 401–405.

[84] Nevin Taaltn, Sadullah Öztürk, Necmettin Klnç, Hayrettin Yüzer, and Zafer Ziya Öztürk. "Fabrication of PdFe nanowires with a high aspect ratio by AAO template-assisted electrodeposition". In: *Journal of Alloys and Compounds* 509.9 (2011), pp. 3894–3898.

[85] Kristina Žužek Rožman, Darja Pečko, Larisa Suhodolčan, Paul J. McGuiness, and Spomenka Kobe. "Electrochemical syntheses of soft and hard magnetic Fe50Pd50-based nanotubes and their magnetic characterization". In: *Journal of Alloys and Compounds* 509.2 (2011), pp. 551–555.

[86] Hengjun Liu, Feng Wang, Yongbin Zhao, Jingjun Liu, Ki Chul Park, and Morinobu Endo. "Synthesis of ironpalladium binary alloy nanotubes by template-assisted electrodeposition from metal-complex solution". In: *Journal of Electroanalytical Chemistry* 633.1 (2009), pp. 15–18.

[87] Veronika Haehnel, Christine Mickel, Sebastian Fa, and Ludwig Schultz. "Structure , Microstructure , and Magnetism of Electrodeposited Fe 70 Pd 30 Nanowires". In: (2010), pp. 19278–19283.

[88] Feng Wang, Sayaka Doi, Kaori Hosoiri, Hirohisa Yoshida, Toshio Kuzushima, Masao Sasadaira, and Torhu Watanabe. "Nanostructured FePd thin films for thermoelastic shape memory alloyselectrochemical preparation and characterization". In: *Electrochimica Acta* 51.20 (2006), pp. 4250–4254.

[89] Kazuya Tsujino and Michio Matsumura. "Helical Nanoholes Bored in Silicon by Wet Chemical Etching Using Platinum Nanoparticles as Catalyst". In: *Electrochemical and Solid-State Letters* 8.12 (2005), p. C193.

[90] X Li and P W Bohn. "Metal-assisted chemical etching in HF/H[sub 2]O[sub 2] produces porous silicon". In: *Applied Physics Letters* 77.16 (2000), p. 2572.

[91] Hideki Masuda and Masahiro Satoh. "Fabrication of gold nanodot array using anodic porous alumina as an evaporation mask". In: *Japanese Journal of Applied Physics, Part 2: Letters* 35.1 B (1996).

[92] H Masuda and K Fukuda. "Ordered metal nanohole arrays made by a two-step replication of honeycomb structures of anodic alumina." In: *Science (New York, N.Y.)* 268.5216 (1995), pp. 1466–8.

[93] Mickael Lillo and Dusan Losic. "Pore opening detection for controlled dissolution of barrier oxide layer and fabrication of nanoporous alumina with through-hole morphology". In: *Journal of Membrane Science* 327.1-2 (2009), pp. 11–17.

[94] Paula V. Jasen, Estela A. Gonzalez, Norberto J. Castellani, and Alfredo Juan. "Theoretical study of hydrogen adsorption on FePd face-centered cubic alloy surfaces". In: *Physical Review B* 71.23 (2005), p. 235422.

[95] T. Klemmer, D. Hoydick, H. Okumura, B. Zhang, and W. A. Soffa. "Magnetic hardening and coercivity mechanisms in L10 ordered FePd ferromagnets". In: *Scripta Metallurgica et Materiala* 33.10-11 (1995), pp. 1793–1805.

[96] Kazuhisa Sato, Bo Bian, and Yoshihiko Hirotsu. "Fabrication of oriented L1 0-FePt and FePd nanoparticles with large coercivity". In: *Journal of Applied Physics* 91.10 I (2002), pp. 8516–8518.

[97] Sven Hamann and Ruhr-universität Bochum. "Development and characterization of Fe 70 Pd 30 ferromagnetic shape memory splats". In: October (2015).

[98] R A Stern, S D Willoughby, J M MacLaren, J Cui, Q Pan, and R D James. "Fe3Pd ferromagnetic shape memory alloys". In: *J. Appl. Physics* 93.10 (2003), pp. 8644–8646.

[99] Hiroyuki Kato, Yuanchang Liang, and Minoru Taya. "Stress-induced FCC/FCT phase transformation in Fe-Pd alloy". In: *Scripta Materialia* 46.6 (2002), pp. 471–475.

[100] Shozo Inoue, Kanryu Inoue, Syuji Fujita, and Keiji Koterazawa. "Fe-Pd Ferromagnetic Shape Memory Alloy Thin Films Made By Dual Source DC Magnetron Sputtering." In: *Materials Transactions* 44.2 (2003), pp. 298–304.

[101] Huiping Xu, Helge Heinrich, and Jörg M K Wiezorek. "Microstructural changes during annealing of FePd-based thin films". In: 11.9 (2003), pp. 963–969.

[102] L. Kühnemund, T. Edler, I. Kock, M. Seibt, and S. G. Mayr. "Epitaxial growth and stress relaxation of vapor-deposited Fe-Pd magnetic shape memory films". In: *New Journal of Physics* 11 (2009).

[103] V.M. Prida, V. Vega, V. Franco, J.L. Sánchez Llamazares, M.J. Pérez, J.D. Santos, Ll. Escoda, J.J. Suñol, and B. Hernando. "FePd melt-spun ribbons and nanowires: Fabrication and magneto-structural properties". In: *Journal of Magnetism and Magnetic Materials* 321.7 (2009), pp. 790–792.

[104] D. Vokoun, C.T. Hu, Y.H. Lo, A. Lančok, and O. Heczko. "Transformation Properties of Fe70-Pd30-XInX Shape Memory Melt-spun Ribbons". In: *Materials Today: Proceedings* 2 (2015), S845–S848.

[105] Jake Steiner, Abdellah Lisfi, Tomoyuki Kakeshita, Takashi Fukuda, and Manfred Wuttig. "Unique magnetostriction of Fe68.8Pd31.2 attributable to twinning". In: *Scientific Reports* 6.1 (2016), p. 34259.

[106] A. Kulovits, W. A. Soffa, W. Püschl, and W. Pfeiler. "Ordering and disordering in L10 FePd alloys as studied by residual resistivity measurement". In: *Intermetallics* 13.5 (2005), pp. 510–514.

[107] Fernanda M. Takata, Gyana Pattanaik, William a. Soffa, Paulo T.a. Sumodjo, and Giovanni Zangari. "Synthesis of L10 FePd films by electrodeposition and thermal annealing". In: *Electrochemistry Communications* 10.4 (2008), pp. 568–571.

[108] Cuicui Qiu, Xiaoqiang Dong, Minghu Huang, Sihui Wang, and Houyi Ma. "Facile fabrication of nanostructured Pd-Fe bimetallic thin films and their electrodechlorination activity". In: *Journal of Molecular Catalysis A: Chemical* 350.1-2 (2011), pp. 56–63.

[109] M. Rezaei, M. Ghorbani, and A. Dolati. "Electrochemical investigation of electrodeposited FePd alloy thin films". In: *Electrochimica Acta* 56.1 (2010), pp. 483–490.

[110] Defu Liang, Jonathan J. Mallett, and Giovanni Zangari. "Underpotential Codeposition of FePt Alloys from an Alkaline Complexing Electrolyte: Electrochemical Studies". In: *Journal of The Electrochemical Society* 158.3 (2011), pp. D149–D157.

[111] L.H. H Mendoza-Huizar, J. Robles, and M. Palomar-Pardavé. "Nucleation and growth of cobalt onto different substrates Part I. Underpotential deposition onto a gold electrode". In: *Journal of Electroanalytical Chemistry* 521 (2002), pp. 95–106.

[112] K. Žužek Rožman, D. Pečko, S. Šturm, U. Maver, P. Nadrah, M. Bele, and S. Kobe. "Electrochemical synthesis and characterization of Fe70Pd30 nanotubes for drug-delivery applications". In: *Materials Chemistry and Physics* 133.1 (2012), pp. 218–224.

[113] Darja Pečko, Kristina Žužek Rožman, Nina Kostevšek, M. Shahid Arshad, Boštjan Markoli, Zoran Samardžija, and Spomenka Kobe. "Electrodeposited hard-magnetic Fe50Pd50 nanowires from an ammonium-citrate-based bath". In: *Journal of Alloys and Compounds* 605 (2014), pp. 71–79.

[114] Tetsuya Akiyama and Hisaaki Fukushima. "Recent Study on the Mechanism of the Electrodeposition lron-group Metal Alloys". In: *ISIJ international* 32.1 992 (1992), pp. 787–798.

[115] Yasushi Endo, Yuji Yamanaka, Yoshio Kawamura, and Masahiko Yamamoto. "Formation of L10-type ordered FePd phase in multilayers composed of Fe and Pd". In: *Japanese Journal of Applied Physics, Part 1: Regular Papers and Short Notes and Review Papers* 44.5 A (2005), pp. 3009–3014.

[116] R Oshima. "Successive martensitic transformations in Fe- Pd alloys". In: *Scripta Metallurgica* 15.i (1981), pp. 829–833.

[117] Shinji Muraishi Cheng Xu Minoru Taya. "Effect of shape and residual stress of Fe-Pd nano-material on martensite phase transformation". In: *to be submetted* ().

[118] Kenta Seki, Hiroaki Kura, Tetsuya Sato, and Tomoyasu Taniyama. "Size dependence of martensite transformation temperature in ferromagnetic shape memory alloy FePd". In: *Journal of Applied Physics* 103.6 (2008).

[119] A. Encinas-Oropesa, M. Demand, L. Piraux, I. Huynen, and U. Ebels. "Dipolar interactions in arrays of nickel nanowires studied by ferromagnetic resonance". In: *Physical Review B - Condensed Matter and Materials Physics* 63.10 (2001), pp. 1044151–1044156.

[120] a. Kumar, S. Fähler, H. Schlörb, K. Leistner, and L. Schultz. "Competition between shape anisotropy and magnetoelastic anisotropy in Ni nanowires electrodeposited within alumina templates". In: *Physical Review B* 73.6 (2006), p. 064421.

[121] Frank S Bates and Glenn H Fredrickson. "Block Copolymers-Designer Soft Materials". In: *Phycisc Today* 2.1999 (1999), p. 32.

[122] Ashish K Khandpurj, Stephan Farster, Frank S Bates, Ian W Hamley, and Anthony J Ryan. "Polyisoprene-Polystyrene Diblock Copolymer Phase Diagram near the Order-Disorder Transition". In: (1995), pp. 8796–8806.

[123] M. W. Matsen and M. Schick. "Stable and unstable phases of a diblock copolymer melt". In: *Physical Review Letters* 72.16 (1994), pp. 2660–2663.

[124] P Mansky, C K Harrison, P M Chaikin, R A Register, N Yao, P Mansky, C K Harrison, and P M Chaikin. "Nanolithographic templates from diblock copolymer thin films Nanolithographic templates from diblock copolymer thin films". In: 2586.1996 (2008).

[125] Christopher M Bates, Michael J Maher, Dustin W Janes, Christopher J Ellison, and C Grant Willson. "Block Copolymer Lithography". In: (2014).

[126] D Zhao, J Feng, Q Huo, N Melosh, Gh Fredrickson, Bf Chmelka, and Gd Stucky. "Triblock copolymer syntheses of mesoporous silica with periodic 50 to 300 angstrom pores". In: *Science (New York, N.Y.)* 279.5350 (1998), pp. 548–52.

[127] Vanessa Z Chan, James Hoffman, Victor Y Lee, Hermis Iatrou, Apostolos Avgeropoulos, Nikos Hadjichristidis, Robert D Miller, and Edwin L Thomas. "Ordered Bicontinuous Nanoporous and Nanorelief Ceramic Films from Self Assembling Polymer Precursors". In: 286.November 1999 (1999), pp. 1716–1720.

[128] Augustine Urbas, Yoel Fink, and Edwin L Thomas. "One-Dimensionally Periodic Dielectric Reflectors from Self-Assembled Block Copolymer - Homopolymer Blends". In: (1999), pp. 4748–4750.

[129] Yoel Fink, Augustine M Urbas, Moungi G Bawendi, John D Joannopoulos, and Edwin L Thomas. "Block Copolymers as Photonic Bandgap Materials". In: 17.11 (1999), pp. 1963–1969.

[130] Yuhua Yin, Pingchuan Sun, Tiehong Chen, Baohui Li, Qinghua Jin, Datong Ding, and An Chang Shi. "Simulated annealing study of diblock copolymer thin films confined between two homogeneous surfaces". In: *ChemPhysChem* 5.4 (2004), pp. 540–548.

[131] Bin Yu, Pingchuan Sun, Tiehong Chen, Qinghua Jin, Datong Ding, and Baohui Li. "Confinement-Induced Novel Morphologies of Block Copolymers". In: 138306.April (2006), pp. 1–4.

[132] Bin Yu, Pingchuan Sun, Tiehong Chen, Qinghua Jin, Datong Ding, Baohui Li, and An Chang Shi. "Self-assembly of diblock copolymers confined in cylindrical nanopores". In: *Journal of Chemical Physics* 127.11 (2007).

[133] Zheng Wang, Baohui Li, Qinghua Jin, Datong Ding, and An Chang Shi. "Simulated annealing study of self-assembly of symmetric ABA triblock copolymers confined in cylindrical nanopores". In: *Macromolecular Theory and Simulations* 17.2-3 (2008), pp. 86–102.

[134] Bin Yu, Qinghua Jin, Datong Ding, Baohui Li, and An Chang Shi. "Confinement-induced morphologies of cylinder-forming asymmetric diblock copolymers". In: *Macromolecules* 41.11 (2008), pp. 4042–4054.

[135] H. P. Huinink, J. C. M. Brokken-Zijp, M. A. van Dijk, and G. J. A. Sevink. "Asymmetric block copolymers confined in a thin film". In: *The Journal of Chemical Physics* 112.5 (2000), pp. 2452–2462.

[136] G. J A Sevink, A. V. Zvelindovsky, J. G E M Fraaije, and H. P. Huinink. "Morphology of symmetric block copolymer in a cylindrical pore". In: *Journal of Chemical Physics* 115.17 (2001), pp. 8226–8230.

[137] A. Knoll, A. Horvat, K. S. Lyakhova, G. Krausch, G. J.A. Sevink, A. V. Zvelindovsky, and R. Magerle. "Phase behavior in thin films of cylinder-forming block copolymers". In: *Physical Review Letters* 89.3 (2002), pp. 355011–355014.

[138] Xuehao He, Mo Song, Haojun Liang, and Caiyuan Pan. "Self-assembly of the symmetric diblock copolymer in a confined state: Monte Carlo simulation". In: *Journal of Chemical Physics* 114.23 (2001), p. 10510.

[139] Jie Feng and Eli Ruckenstein. "Morphologies of AB diblock copolymer melts confined in nanocylindrical tubes". In: *Macromolecules* 39.14 (2006), pp. 4899–4906.

[140] Qiang Wang. "Symmetric diblock copolymers in nanopores: Monte Carlo simulations and strong-stretching theory". In: *Journal of Chemical Physics* 126.2 (2007).

[141] Yuping Sheng, Jian An, and Yutian Zhu. "Self-assembly of ABA triblock copolymers under soft confinement". In: *Chemical Physics* 452 (2015), pp. 46–52.

[142] Gj Kellogg, Dg Walton, Am Mayes, P Lambooy, Tp Russell, Pd Gallagher, and Sk Satija. "Observed surface energy effects in confined diblock copolymers." In: *Physical review letters* 76.14 (1996), pp. 2503–2506.

[143] Yiming Sun, Martin Steinhart, Danilo Zschech, Rameshwar Adhikari, Goerg H. Michler, and Ulrich Gösele. "Diameter-dependence of the morphology of PS-b-PMMA nanorods confined within ordered porous alumina templates". In: *Macromolecular Rapid Communications* 26.5 (2005), pp. 369–375.

[144] Minglin Ma, Kirill Titievsky, Edwin L. Thomas, and Gregory C. Rutledge. "Continuous concentric lamellar block copolymer nanofibers with long range order". In: *Nano Letters* 9.4 (2009), pp. 1678–1683.

[145] Hongqi Xiang, Kyusoon Shin, Taehyung Kim, Sung In Moon, Thomas J Mccarthy, and Thomas P Russell. "Block Copolymers under Cylindrical Confinement Block Copolymers under Cylindrical Confinement". In: *Society* 37.15 (2004), pp. 5660–5664.

[146] K. Shin. "Curving and Frustrating Flatland". In: *Science* 306.5693 (2004), pp. 76–76.

[147] Hongqi Xiang, Kyusoon Shin, Taehyung Kim, Sung In Moon, Thomas J. McCarthy, and Thomas P. Russell. "From cylinders to helices upon confinement". In: *Macromolecules* 38.4 (2005), pp. 1055–1056.

[148] Hongqi Xiang, Kyusoon Shin, Taehyung Kim, Sungin Moon, T J Mccarthy, and T P Russell. "The Influence of Confinement and Curvature on the Morphology of Block Copolymers". In: June (2005), pp. 3377–3383.

[149] Suman K. Jana, Reiichi Nishida, Kazuya Shindo, Tsuyoshi Kugita, and Seitaro Namba. "Pore size control of mesoporous molecular sieves using different organic auxiliary chemicals". In: *Microporous and Mesoporous Materials* 68.1-3 (2004), pp. 133–142.

[150] P. Schmidt-Winkel, W. W. Lukens, P. Yang, D. I. Margolese, J. S. Lettow, J. Y. Ying, and G. D. Stucky. "Microemulsion templating of siliceous mesostructured cellular foams with well-defined ultralarge mesopores". In: *Chemistry of Materials* 12.3 (2000), pp. 686–696.

[151] Abdelhamid Sayari. "Unprecedented expansion of the pore size and volume of periodic mesoporous silica". In: *Angewandte Chemie - International Edition* 39.16 (2000), pp. 2920–2922.

[152] J. L. Blin and Bao Lian Su. "Tailoring pore size of ordered mesoporous silicas using one or two organic auxiliaries as expanders". In: *Langmuir* 18.13 (2002), pp. 5303–5308. ISSN: 07437463.

[153] Darren R. Dunphy, Pratik H. Sheth, Fred L. Garcia, and C. Jeffrey Brinker. "Enlarged pore size in mesoporous silica films templated by pluronic F127: Use of poloxamer mixtures and increased template/SiO2 ratios in materials synthesized by evaporation-induced self-assembly". In: *Chemistry of Materials* 27.1 (2015), pp. 75–84.

[154] Malin H. Sörensen, Robert W. Corkery, Jan Skov Pedersen, Jessica Rosenholm, and Peter C. Alberius. "Expansion of the F127-templated mesostructure in aerosol-generated particles by using polypropylene glycol as a swelling agent". In: *Microporous and Mesoporous Materials* 113.1-3 (2008), pp. 1–13.

[155] Tate Michael P., Urade Vikrant N., Kowalski Jonathon D., Wei Ta Chen, Hamilton Benjamin D., Eggiman Brian W., and Hillhouse Hugh W. "Simulation and interpretation of 2D diffraction patterns from self-assembled nanostructured films at arbitrary angles of incidence: From grazing incidence (above the critical angle) to transmission perpendicular to the substrate". In: *Journal of Physical Chemistry B* 110.20 (2006), pp. 9882–9892.

[156] Michael P. Tate, Vikrant N. Urade, Jonathon D. Kowalski, Ta Chen Wei, Benjamin D. Hamilton, Brian W. Eggiman, and Hugh W. Hillhouse. "Simulation and interpretation of 2D diffraction patterns from self-assembled nanostructured films at arbitrary

angles of incidence: From grazing incidence (above the critical angle) to transmission perpendicular to the substrate". In: *Journal of Physical Chemistry B* 110.20 (2006), pp. 9882–9892. URL: NANOCELL2_0_2, http://faculty.washington.edu/h2/simulation.html.

[157] Weihua Li and Robert A Wickham. "Self-Assembled Morphologies of a Diblock Copolymer Melt Confined in a Cylindrical Nanopore Self-Assembled Morphologies of a Diblock Copolymer Melt Confined in a Cylindrical Nanopore". In: (2006), pp. 8492–8498.

[158] Peter C A Alberius, Karen L Frindell, Ryan C Hayward, Edward J Kramer, Galen D Stucky, and Bradley F Chmelka. "General Predictive Syntheses of Cubic , Hexagonal , and Lamellar Silica and Titania Mesostructured Thin Films §". In: 25 (2002), pp. 3284–3294.

[159] *Ordered Mesoporous Materials*. Wiley-VCH Verlag GmbH Co. KGaA, 2013.

[160] D Zhao, J Feng, Q Huo, N Melosh, Gh Fredrickson, Bf Chmelka, and Gd Stucky. "Triblock copolymer syntheses of mesoporous silica with periodic 50 to 300 angstrom pores". In: *Science (New York, N.Y.)* 279.5350 (1998), pp. 548–52.

[161] Burton B P. "Binary Alloy Phase Diagrams". In: (1990).

[162] Y P Zhao, D X Ye, G C Wang, and T M Lu. "Designing nanostructures by glancing angle deposition". In: *Proceedings of SPIE Vol. 5219 Nanotubes and Nanowires* 5219 (2003), pp. 59–73.

[163] Richard Kovács. "American Association for the Advancement of Science". In: 54.2 (2014), pp. 155–161.

[164] K Shimizu and T Kakeshita. "Effect of magnetic fields on martensitic transformations in ferrous alloys and steels". In: *ISIJ International* 29.2 (1989), pp. 97–166.

[165] *The Equilibrium Theory of Inhomogeneous Polymers*. Clarendon Press, Oxford, 2006.

Appendix A

SELF-CONSISTENT FIELD THEORY EQUATIONS

The self-consistent field theory describes the polymer melt problem by analyzing the conformation of a single random-walk polymer chain in a potential field created by the other chains. For a AB diblock copolymer with N monomers and A volume fraction of f, different types of monomers are labeled by 'A' for A block and 'B' for B block. Specific monomers are labeled by a contour variable s ($0 < s < N$). The statistical mechanics of the polymer chain in an external field $\omega(\mathbf{r})$ can be fully described by the following end-segment distribution functions (A.0.1 and A.0.2) :

$$\frac{\partial q(\mathbf{r},s)}{\partial s} = \left[\nabla^2 - \omega(\mathbf{r},s))\right] q(\mathbf{r},s) \tag{A.0.1}$$

$$-\frac{\partial q^\dagger(\mathbf{r},s)}{\partial s} = \left[\nabla^2 - \omega(\mathbf{r},s))\right] q^\dagger(\mathbf{r},s) \tag{A.0.2}$$

where the initial condition is $q(\mathbf{r},0) = q^\dagger(\mathbf{r},N) = 1$. $q(\mathbf{r},s)$ is the end-segment distribution function for a segment of chain starting from 0 to s constrained at position $\mathbf{r}$. The product of $q(\mathbf{r},0)q^\dagger(\mathbf{r},N)$ is proportional to the probability of a specific monomer s at position $\mathbf{r}$.

The concentrations of monomers of type A and B at position $\mathbf{r}$ are expressed in equation A.0.3, A.0.4:

$$\phi_A(\mathbf{r}) = \frac{1}{Q}\int_0^f ds\, q(\mathbf{r},s)q^\dagger(\mathbf{r},s) \tag{A.0.3}$$

$$\phi_B(\mathbf{r}) = \frac{1}{Q}\int_f^1 ds\, q(\mathbf{r},s)q^\dagger(\mathbf{r},s) \tag{A.0.4}$$

with

$$Q = \frac{1}{V}\int_{|\mathbf{r}|\le R} d\mathbf{r}\, q(\mathbf{r},N) \tag{A.0.5}$$

where V is the unit cell volume, R is the diameter of the geometrical confining cylinder. The constrain of incompressible of AB block copolymer melt is expressed as:

$$\phi_A(\mathbf{r}) + \phi_B(\mathbf{r}) = 1 \tag{A.0.6}$$

The chemical potential field for an incompressible melt is given by:

$$\omega_A(\mathbf{r}) = \chi N \phi_B(\mathbf{r}) + H(\mathbf{r}) + \eta(\mathbf{r}) \tag{A.0.7}$$

$$\omega_B(\mathbf{r}) = \chi N \phi_A(\mathbf{r}) - H(\mathbf{r}) + \eta(\mathbf{r}) \tag{A.0.8}$$

with a surface field [157]

$$\begin{cases} \frac{H(\mathbf{r})}{\chi N} = v_0(e^{(|\mathbf{r}|-R)/\lambda} - e^{-\sigma/\lambda}) & , \quad R-\sigma \leq |\mathbf{r}| \leq R \\ H(\mathbf{r}) = 0 & , \quad |\mathbf{r}| < R-\sigma \end{cases} \tag{A.0.9}$$

where σ is the thickness of surface field interaction, v_0 describes the strength of the polymer-confining wall interaction, λ is the decay length of the surface field.

The free energy per monomer of the resulting polymer structure confined inside a cylindrical pore with the diameter R has the form:

$$\frac{F}{nk_BT} = -lnQ + \frac{1}{V}\int_{|\mathbf{r}|\leq R} d\mathbf{r}\left\{\chi N \phi_A(\mathbf{r})\phi_B(\mathbf{r}) - \omega_A(\mathbf{r})\phi_A(\mathbf{r}) - \omega_B(\mathbf{r})\phi_B(\mathbf{r}) + H(\mathbf{r})\left[\phi_A(\mathbf{r}) - \phi_B(\mathbf{r})\right]\right\} \tag{A.0.10}$$

Detailed explanation of the SCF equations can be found in Fredrickson's book [165]. The above SCF equations are solved by the pseudospectral method with a C++ program PolyorderConf (free for academic use upon request).

Appendix B

PUBLICATION

Taya, M., Xu, C., Matsuse, T., & Muraishi, S. (2017). Molecular dynamics model for nano-motions of FePd nanohelices. Journal of Applied Physics, 121(15), 154302.